PREPARED FOR THE U.S. DEPARTMENT OF ENERGY,
UNDER CONTRACT DE-AC02-76CH03073

PPPL-3892
UC-70

PPPL-3892

Physics of Substorm Growth Phase, Onset, and Dipolarization

by

C.Z. Cheng

October 2003

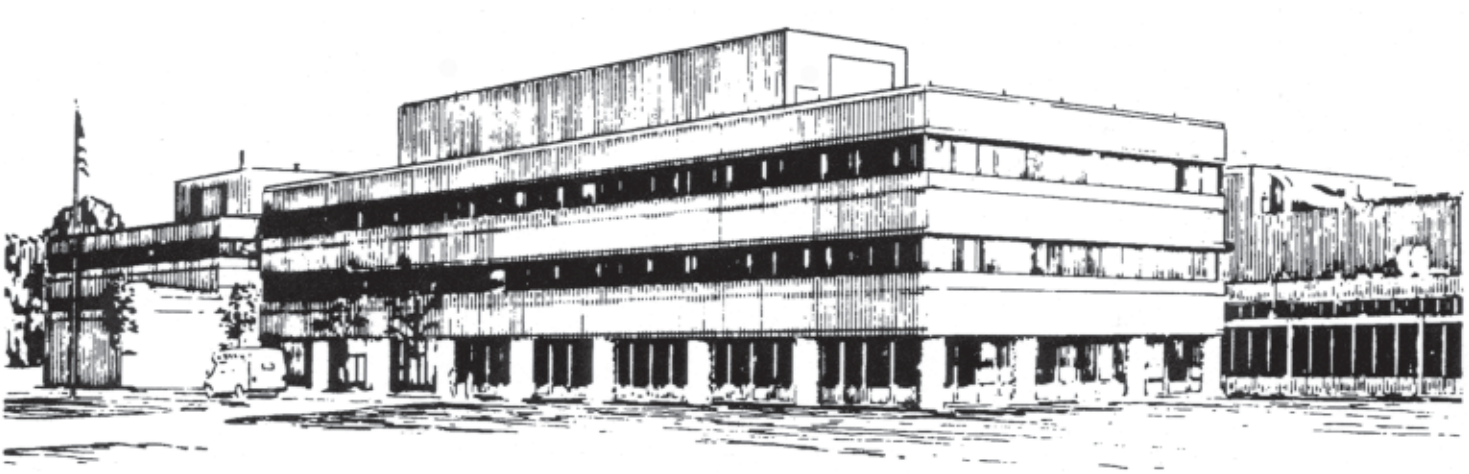

PRINCETON PLASMA PHYSICS LABORATORY
PRINCETON UNIVERSITY, PRINCETON, NEW JERSEY

PPPL Reports Disclaimer

Availability

This report is posted on the U.S. Department of Energy's Princeton Plasma Physics Laboratory Publications and Reports web site in Fiscal Year 2004. The home page for PPPL Reports and Publications is: http://www.pppl.gov/pub_report/

DOE and DOE Contractors can obtain copies of this report from:

U.S. Department of Energy
Office of Scientific and Technical Information
DOE Technical Information Services (DTIS)
P.O. Box 62
Oak Ridge, TN 37831

Telephone: (865) 576-8401

Fax: (865) 576-5728

Email: reports@adonis.osti.gov

This report is available to the general public from:

National Technical Information Service
U.S. Department of Commerce
5285 Port Royal Road
Springfield, VA 22161

Telephone: 1-800-553-6847 or
(703) 605-6000

Fax: (703) 321-8547

Internet: http://www.ntis.gov/ordering.htm

Physics of Substorm Growth Phase, Onset, and Dipolarization

C. Z. Cheng
Princeton Plasma Physics Laboratory, Princeton University, Princeton, NJ 08543

Received _____; accepted _____

Short title: SUBSTORM MECHANISMS

Abstract. A new scenario of substorm growth phase, onset and dipolarization during expansion phase and the corresponding physical processes are presented. During the growth phase, as a result of enhanced plasma convection, the plasma pressure and its gradient are continued to be enhanced over the quiet-time values in the plasma sheet. Toward the late growth phase, a strong cross-tail current sheet is formed in the near-Earth plasma sheet region, where a local magnetic well is formed, the plasma beta can reach a local maximum with value larger than 50 and the cross-tail current density can be enhanced to over 10nA/m^2 as obtained from 3D quasi-static magnetospheric equilibrium solutions for the growth phase. The most unstable kinetic ballooning instabilities (KBI) are expected to be located in the tailward side of the strong cross-tail current sheet region. The field lines in the most unstable KBI region map to the transition region between the region-1 and region-2 currents in the ionosphere, which is consistent with the observed initial brightening location of the breakup arc in the intense proton precipitation region. The KBI explains the AMPTE/CCE observations that a low frequency instability with a wave period of $50 - 75$ seconds is excited about 2-3 minutes prior to substorm onset and grows exponentially to a large amplitude at the onset of current disruption (or current reduction). At the current disruption onset higher frequency instabilities are excited so that the plasma and electromagnetic field fluctuations form a strong turbulent state. Plasma transport takes place due to the strong turbulence to relax the ambient plasma pressure profile so that the plasma pressure and current density are reduced and the ambient magnetic field intensity increases by more than a factor of 2 in the high-β_{eq} region and the field line geometry recovers from tail-like to dipole-like – dipolarization.

1. Introduction

Substorms are considered to be the most important dynamical process in regulating the plasma and magnetic field energy in the magnetosphere (particularly in the plasma sheet) and the ionosphere. The observations of substorm auroral and magnetospheric processes clearly demonstrate that the entire substorm process involves a growth phase, onset and breakup, expansion phase, and recovery phase [e.g., *Akasofu*, 1977]. During the growth phase the polar cap region expands equatorward, the auroral oval shrinks in width, convection enhances, and the magnetospheric magnetic field topology at the night side becomes stretched. Immediately before the breakup, a discrete auroral arc (usually the equatorward-most visible arc) brightens from within a 1° to 2° wide latitude region of the intense proton emission near the poleward edge of the intense proton precipitation [*Samson et al.*, 1992a]. The onset of expansion phase is an extremely fast and apparently local process characterized in the ionosphere by a localized brightening usually located in the pre-midnight sector in the breakup arc and in the magnetosphere by a localized turbulent disturbance in the near-Earth plasma sheet equatorial region. These significant morphological changes occur on a time scale of tens of seconds or even less. The substorm breakup in the expansion phase involves the development of the breakup arc into a vortex structure, a poleward expansion of the vortex within the auroral oval which corresponds to the spread of turbulent disturbance into a wider region in all directions in the equatorial plane, the dipolarization of the magnetic field topology in the inner central plasma sheet (CPS), the energization of CPS particles, and the magnetic signatures of the enhanced ionospheric currents. In the expansion phase, the expanding vortex reaches the poleward boundary of diffuse electron precipitation, which also expands poleward. The expansion phase lasts minutes to tens of minutes, after which the system returns to a less disturbed state during the recovery phase which lasts tens of minutes. It is to be emphasized that the substorm energy release in the auroral electrojet is only a small portion of the total substorm energy release. Most energy is released through changes in ring current, cross-

tail current, plasma sheet plasma and magnetic field, and perhaps plasmoid formation and its tailward motion in the magnetosphere.

Not all substorm dynamical processes lead to a full expansion phase of auroral arc breakup. Weaker substorms form an auroral vortex that does not expand as far poleward as the polar cap boundary, and that is not accompanied by signatures of lobe flux reconnection. However, these substorms begin with the intensification of a discrete auroral arc, and lead to vortex formation. These substorms have been called pseudo-breakups. Pseudo-breakups stall before lobe field lines are involved whereas full breakups are followed by a full expansion phase. In this paper they are considered as weak substorms [see, e.g., *Mishin et al.*, 2000, and references therein].

The entire substorm process can be considered phenomenologically as a dynamical sequence of energy storage and release in the plasma sheet. Because the change of energy in the ionosphere is much smaller than that in the plasma sheet during substorms, the substorm auroral dynamics can be considered as the ionospheric signatures of the plasma sheet dynamics. The growth phase is a period of enhanced energy storage in the plasma sheet which can be considered as a magnetic container to store enhanced plasma particle and energy. The stored plasma energy consists of the plasma pressure and its earthward gradient. The magnetic energy of the plasma sheet also increases during the growth phase due to the equatorward compression and tailward stretching of the magnetic field lines so that a greater amount of plasma free energy can be stored in the magnetic container. The plasmas are supplied by the solar wind through enhanced magnetic merging and reconnection on the dayside. As the plasma free energy in the plasma sheet increases above a critical level, which depends on the capacity of the magnetic container, plasma instabilities are triggered and a plasma turbulence is excited in the plasma sheet at the substorm onset. During the expansion phase, the turbulence spreads in the plasma sheet and redistributes and energizes the plasmas, and some plasmas are eventually transported out of the plasma sheet into ionosphere, inner magnetosphere

and even down the magnetotail tail. The plasma turbulence and transport processes then relax the plasma pressure profile to reduce the free energy that excites the plasma instabilities, cause the cross-tail current density to reduce and the magnetic field to dipolarize in the central plasma sheet, which are related to the auroral breakup and intensification, and enhanced ionospheric currents. After the turbulence level decreases, the plasma sheet and the ionosphere recover to a less disturbed state during the recovery phase. Other phenomenological views of substorms in terms of energy storage and release with different proposals of energy storage and release processes have also been proposed [e.g., *Rostoker et al.*, 1980; *Rostoker*, 1999].

As the substorm research progresses, one needs to understand the underlying physical mechanisms of substorm processes. Thus, a satisfactory substorm model requires detailed theories and calculations to explain the underlying physical processes such as how the magnetospheric configuration and plasma distribution changes during the growth phase, what instability causes the substorm onset and leads to plasma turbulence and auroral breakup, and what causes the magnetic field to dipolarize in the plasma sheet, etc. The models must subject to the observational constraints.

In this paper, we present theoretical models to address some of the key issues of substorm observations: plasma pressure, current and magnetic field distributions in the magnetosphere and corresponding features in the ionosphere during the growth phase, features of substorm onset due to kinetic ballooning instability, and the mechanism of dipolarization in the plasma sheet during the expansion phase. The theoretical models for these processes are inter-related. The theoretical calculations are compared with observations to verify the theoretical models. In the following we first review the relevant observational features of substorms in both the magnetosphere and ionosphere. We then present three-dimensional (3D) solutions of the magnetosphere that satisfy force balance among plasma pressure, current and magnetic field with the effect of plasma flow energy neglected. The ideal MHD and kinetic theories of ballooning instability are

then presented to describe the substorm onset process. Then, a theory of dipolarization in the plasma sheet is presented. A discussion of the role of magnetic reconnection on substorm is also presented. Finally, a summary and discussion is presented.

2. Review of Relevant Observational Features of Substorms

In this Section we review salient observational features of substorm dynamics in both the magnetosphere and the ionosphere. These observations are extremely important in constraining substorm theories and clarifying questions concerning the magnetosphere-ionosphere coupling. However, the difficulties in observing substorm onset related phenomena due to its extremely fast time scale and localized spatial scale are often exacerbated by significantly disturbed background conditions that can obscure the real commencement of auroral breakup and expansion phase activity. *Liou et al.* [1999, 2000] compared different signatures of onset and concluded that the most robust substorm onset timing indicator is the breakup arc brightening that typically overtakes other signatures of the expansion phase commencement. Therefore, to reach a comprehensive understanding of substorm dynamics it requires a comparison of auroral signatures with the plasma sheet dynamics.

2.1. Substorm Growth Phase

The first stage of substorm dynamics is called the growth phase [*McPherron*, 1970] and typically starts after the interplanetary magnetic field (IMF) turns southward. It typically lasts about 0.5-1 hour with a significant amount of energy stored in the plasma sheet. During the growth phase an increased cross-tail electric field enhances the plasma convection toward the earth such that the plasma pressure (and thus its gradient) increases and the cross-tail current intensifies in the near-Earth plasma sheet region. Observations [*Kistler et al.*, 1992] have shown that the pre-onset pressure increases monotonically with decreasing radial distance, reaching 1.5 nPa at $10\,R_E$, 4 nPa at $7\,R_E$,

and 10 nPa at $5\,R_E$. In the meantime the open magnetic flux forms in the lobe region, which expands equatorward with enhanced magnetic field intensity, pushes the plasma sheet magnetic field equatorward, and causes them to stretch tailward leading to the thinning of the plasma sheet and the formation of a "thin" and intensified cross-tail current sheet in the near-Earth plasma sheet region ($\sim 6 - \sim 13\,R_E$) [e.g., *Sergeev et al.*, 1990, 1993b; *Lui*, 1993; *Sanny et al.*, 1994]

Figure 1.

The common ionospheric signatures of the growth phase include that the polar cap region expands equatorward, the aurora emissions of both soft electrons with energy of $\sim$ 100 eV (630 nm red line emissions) and energetic protons (486.1 nm H_β emissions) move equatorward and brighten, and the auroral oval shrinks in width. These features are clearly shown in the ground based optical images between t1 and t2 as well as between t3 and t4 in plates (a) and (c) of Figure 1 [*Voronkov et al.*, 2003]. Usually, several brightening spots are observed during the polar cap expansion. The poleward edge of the auroral oval (or soft electron precipitation) defines the polar cap region, and corresponds to the open-closed field line boundary [*Samson et al.*, 1992b; *Blanchard et al.*, 1997]. Thus, the equatorward expansion of the polar cap corresponds to the equatorward expansion of the lobe region. The equatorward movement and brightening of the electron and proton aurora emissions correspond to the equatorward movement of the field aligned currents and their intensification in the ionosphere. Typically the proton aurora forms a band of $\sim 2^\circ$ latitude and overlaps with the equatorward part of the electron aurora, which has a $\sim 5^\circ$ width in latitude. Prior to substorm onset, the latitudinal extent of the soft electron precipitation region decreases to $\sim 2^\circ$ to 5°, which indicates significant stretching of magnetic field lines in the magnetotail and thinning of the plasma sheet.

Another important ionospheric feature of the substorm growth phase is that prior to substorm onset a discrete arc (usually the most equatorward visible arc) in 557.7 nm green line emissions (produced by hard electrons with energy $\geq$ 1 keV) with a thickness of tens of kilometers brightens up for several minutes from within a 1° to

2° wide latitude region of the intense proton emission located near the equatorward edge of the diffuse electron emissions before it forms a vortex and expands poleward, a process called breakup [*Samson et al.*, 1992a; *Voronkov et al.*, 2003]. This feature is clearly shown in the optical images at t2 and t4 in plate (b) of Figure 1. Also, the "breakup" arc usually lies equatorward of the ionospheric convection reversal in the north-south electric field known as the Harang discontinuity. The "breakup" arc can be as much as $5° - 6°$ equatorward of the polar cap boundary, which suggests that the breakup arc is situated on stretched but dipole-like field lines that cross the equatorial plane close to the Earth, possibly between 6 and 12 R_E.

Although the growth phase features such as the equatorward expansion of the polar cap region, thinning of the plasma sheet, and motion of the inner portion of the cross-tail current toward the Earth are very common features of the substorm growth phase, they are not always observed, in particular for weaker substorms, and thus are probably not the necessary conditions for the triggering of a substorm intensification. However, one of the few predictable features of the substorm growth phase is the formation and brightening of a discrete arc and its breakup within the region of intense proton precipitation, which poses as the most critical test of a successful substorm model.

2.2. Substorm Onset

The substorm onset is an extremely fast and apparently local process characterized both in the magnetosphere and the ionosphere by significantly morphological changes that occur on time scales of tens of seconds [e.g., *Takahashi et al.*, 1987b; *Samson et al.*, 1992a]. Based on coordinated observations of AMPTE/CCE and GOES satellites, the substorm onsets are found to be initiated in a localized equatorial region of about 1 R_E wide in the cross-tail current sheet in the near-Earth plasma sheet between $X \sim -6$ to $-10\,R_E$ around midnight [e.g., *Ohtani et al.*, 1991]. At the onset location the magnetic field is marked by the initiation of large amplitude (as large as the background field)

magnetic field fluctuations with wave periods of $\sim$ 60 seconds (in the Pi 2 frequency range) and shorter (15 seconds and below) [*Takahashi et al.*, 1987a]. A more careful analysis of the magnetic field data based on AMPTE/CCE observations shows that a low frequency instability in the Pi 2 frequency range is excited at the near-Earth plasma sheet onset location at about 2 minutes before substorm onset [*Cheng and Lui*, 1998a, 1998b]. The instability occurs when the plasma pressure becomes isotropic and the equtorial plasma β increases abruptly to ≥ 50 from ~ 20 in about 3 minutes near the end of the growth phase [*Lui et al.*, 1992]. The instability grows exponentially to a large amplitude with $\delta B/B \geq 0.3$ at the substorm onset, has $\gamma/\omega_r \sim 0.2$ and $\omega_r/\omega_{ci} \sim 0.1$, and is explained in terms of a kinetic ballooning instability (KBI) [*Cheng and Lui*, 1998a, 1998b], where γ is the instability growth rate and ω_r is the real frequency. Based on the observation of AMPTE/CCE spacecraft, at the approach of substorm onset, there is an explosive growth phase, which lasts $\sim$ 30 seconds and is characterized by a large upsurge in the duskward ion bulk drift to nearly the ion thermal velocity is found near the local midnight sector [*Ohtani et al.*, 1992]. The interaction of the KBI with ions can cause enhanced duskward drift depending on the wave phase. The half wave period of the instability before the current disruption onset corresponds to the explosive growth phase and explains the brief enhancement of duskward ion drift [*Cheng and Lui*, 1998a, 1998b].

At onset the ionospheric signature shows that the breakup arc (typically the most equatorward visible arc) becomes azimuthally structured and forms vortices which grow with a characteristic time of $\sim$ 1 min. The brightest onset location is embedded in the region of enhanced proton precipitation which maps to the inner edge of the plasma sheet [*Samson et al.*, 1992a; *Voronkov et al.*, 2003]. Polar satellite observations also indicate that auroral oval disturbances which lead to a large scale vortex formation appear at the equatorward edge of the electron precipitation region which maps to an near-Earth equatorial distance in the range of $\sim 6 - 10\,\mathrm{R_E}$ [*Frank et al.*, 1998; *Frank and Sigwarth*, 2000]. Statistically the initial brightening spot is located in a wide region (bounded by

roughly $55^\circ - 75^\circ$ in magnetic latitude and $20:00 - 02:00$ MLT with stronger substorms occurring at lower magnetic latitudes [*Kamide*, 1998]. The onset brightening spot is more probable in the pre-midnight sector. The substorm onset location correlates well with solar wind and is controlled by IMF B_z and its polarization. In general, the onset location is at higher latitude for less southward B_z, and the substorm occurrence probability is 100% for southward B_z with $|B_z| > 5nT$.

Note that Pi 2 pulsations were also detected by the ground magnetometers near the auroral breakup region suggesting that Pi 2 pulsations observed by satellites near the substorm onset location in the near-Earth plasma sheet are the source of these pulsations. Moreover, for weak substorms the substorm current wedge that followed the pseudo-breakup was initially confined within the optical auroral breakup region. This further supports that the origin of auroral breakup is in the near-Earth plasma sheet region. Moreover, to link the ionospheric observations of auroral breakup emissions with the equatorial observations of magnetic field fluctuations in the near-Earth plasma sheet, the electrons must be accelerated by these fluctuations to an energy of greater than 1 keV. Thus, a parallel electric field must accompany these fluctuations as they propagate to the ionosphere. This dictates that these fluctuations are of non-MHD origin, and kinetic physics is essential for understanding these fluctuations.

2.3. Substorm Expansion Phase

AMPTE/CCE observations show that at or immediately after substorm onset, higher frequency (periods of $\sim 3 - 15$ seconds in the Pi 1 frequency range) waves/instabilities are also observed at the onset location in the near-Earth plasma sheet region [*Takahashi et al.*, 1987a; *Lui et al.*, 1992]. The higher frequency waves/instabilities combine with the low frequency fluctuations to form a strong turbulence with large magnetic field fluctuations ($\delta B/B \geq 0.5$) through out the expansion phase. These higher frequency waves/instabilities are thought to be due to the cross-field current instability (CCI)

[*Lui et al.*, 1991; *Lui*, 1996] driven by the large upsurge in the ion bulk drift, which oscillates between the eastward and westward directions during the current disruption phase. During the expansion phase the strong turbulence persists and the turbulent region expands in all directions in the equatorial plane as close as the geosynchronous orbit and as far as the mid-magnetotail region [e.g., *Roux et al.*, 1991; *Erickson et al.*, 2000; *Shiokawa et al.*, 2003]. The turbulence transport causes the plasma pressure profile to relax quickly so that the cross-tail current density is reduced, a process called current disruption, and the ambient magnetic field intensity can recover up to the pre-growth phase level in the near-Earth plasma sheet region including the geosynchronous orbit location and the plasma sheet magnetic field configuration recovers from a tail-like geometry to a more dipole-like geometry. Moreover, the turbulence heats and accelerates the plasma sheet particles as it expands. Other expansion phase signatures include the energetic particle injection into the inner magnetosphere [*Reeves et al.*, 1992; *Zaharia et al.*, 2000] and the propagation of the electromagnetic energy flux toward the ionosphere [*Maynard et al.*, 1996; *Erickson et al.*, 2000]. In the mid-magnetotail region numerous satellite observations mainly from Geotail show strong expansion phase activity at distances of $20 - 30\,\mathrm{R_E}$ such as tailward and earthward bursty bulk flows, plasmoids and dipolarization [e.g., *Angelopoulos et al.*, 1992, 1994; *Nagai et al.*, 1998; *Baumjohann et al.*, 1999; *Miyashita et al.*, 2000; *Ieda et al.*, 2001].

In the ionosphere, the intensification of the "breakup" arc (in 577.7 nm green line emissions) is followed by the arc undulation [*Murphree and Johnson*, 1996] giving the start of a large-scale vortex formation and its poleward expansion from the initial arc position, but also spreading out equatorward as well as azimuthally. The optical breakup occurs almost simultaneously with the explosive onset in tens of seconds of short period but longer lasting pulsations and the beginning of dipolarization in the near-Earth plasma sheet [*Friedrich et al.*, 2001; *Voronkov et al.*, 2003]. The westward traveling electrojet associated with substorm current wedge are enhanced explosively poleward of the initial

breakup region. Eventually the aurora is wrapped up into a cell-like (surge) structure. In the meantime, both the auroral proton and electron precipitation (and auroral emissions) move rapidly poleward on the order of a few minutes. The total auroral electrojet current (I_A) in substorms is correlated with the southward IMF B_z. The auroral electrojet location shifts equatorward as I_A increases; from ($10^5 A$ at 70° to $10^6 A$ at 65°) [e.g., *Kamide*, 1998].

Typically the substorm intensification region expands poleward in a few minutes after the initial breakup to the poleward border of the 630.0 nm (red line) emissions (or electron precipitation) as shown in the optical images between t2 and t3 as well as after t5 in plate (c) of Figure 1. And, only after approximately 1-5 minutes, the poleward border of the red line emissions begins to move poleward, possibly owing to the expanding substorm intensification region. Because the poleward border of the red line emission corresponds to the close-open field line boundary, the poleward movement of the poleward border of the red line emissions is interpreted as the beginning of the lobe flux reconnection. The observations suggest that the expansion phase onset occurs prior to the reconnection of lobe field lines, which is perhaps influenced by the rapid spreading of the current disruption region downtail toward the reconnection site [*Friedrich et al.*, 2001].

3. Magnetospheric Configurations During Substorm Growth Phase

Understanding the plasma pressure, current density and magnetic field structures in the magnetosphere and ionosphere in the growth phase is a critical issue that is essential for a better understanding of the substorm onset mechanism and its subsequent expansion. Of particular importance is to answer the questions of how a thin and intensified cross-tail current current sheet is formed in the near-Earth plasma sheet region

($\sim 7 - \sim 13\,R_E$) [e.g., *Sergeev et al.*, 1990; *Lui*, 1993; *Sanny et al.*, 1994], and how the distribution of region-1 and region-2 ionospheric field-aligned (Birkeland) current changes in relation to the proton and soft electron precipitation and optical emission patterns [e.g., *Samson et al.*, 1992a; *Voronkov et al.*, 1999]. The formation of current sheet in the near-Earth plasma sheet region is closely related to the excitation mechanism of the kinetic ballooning instability that initiates the substorm onset [e.g., *Cheng and Lui*, 1998a, 1998b].

The study of the growth phase magnetospheric structure with a current sheet in the near-Earth plasma sheet region requires knowledge of 3D solutions. In particular, we need to understand the structure of the current sheet in terms of location, thickness in the north-south direction, magnetic local time and radial extents, peak cross-tail current intensity, magnetic field intensity and curvature, plasma beta, etc. Moreover, it is also important to know where the thin current sheet region maps to the ionosphere, its location with respect to the Birkeland current distribution, and how it is related to the onset location of the auroral substorm.

The large scale structure of the magnetosphere during the substorm growth phase can be well approximated by quasi-static equilibrium solutions with the plasma pressure gradient in force balance with the Lorentz force due to the cross product of the current density and the magnetic field. During the substorm growth phase the large scale plasma flow is quite steady and its flow energy is usually much smaller than the magnetic energy and the plasma thermal energy. Therefore, during the substorm growth phase the magnetosphere can be considered as a series of snap shots of quasi-static equilibria that vary due to evolving plasma pressure profile and external solar wind and IMFs.

Recently, we have improved our 3D magnetospheric equilibrium modeling code, MAG-3D [*Cheng*, 1995], for computing the magnetic field, currents, and plasma distribution of quasi-static magnetospheric equilibrium states under different solar wind conditions [*Zaharia and Cheng*, 2003; *Zaharia et al.*, 2003]. In particular, we have

investigated the 3D growth phase magnetospheric structure with a thin and intensified cross-tail current sheet in the near-Earth plasma sheet region and the corresponding Birkeland current distribution in the ionosphere [*Zaharia and Cheng*, 2003]. The obtained configuration for the substorm growth phase case shows a thin current sheet with a westward current density $\sim 10\,\mathrm{nA/m^2}$ and plasma beta above 50 in the near-Earth plasma sheet region with a radial extent between $X = -7\,R_E$ and $X = -9\,R_E$, an azimuthal extent between $Y = -5\,R_E$ and $Y = 5\,R_E$, and a half-thickness $\sim 1\,R_E$, in the Z (north-south) direction measured at the peak current density location of $X = -8\,R_E$ (from here on X, Y and Z are the usual GSM coordinates), consistent with observations [e.g., *Sergeev et al.*, 1990; *Lui*, 1993; *Sanny et al.*, 1994]. The magnetic field also forms a local magnetic well in the current sheet region. The near-Earth cross-tail current sheet thickness is in good agreement with observations [*Sanny et al.*, 1994] showing the current sheet being wider than $1\,R_E$ throughout the growth phase.

In comparison with the quiet time magnetosphere, the growth phase configuration is also characterized by the region-1 and region-2 Birkeland currents moving equatorward (60° – 65°) with narrower latitude width, and being more intense (region-1 $J_{\parallel 1\,\max} \sim 3\,\mu\mathrm{A/m^2}$). If we interpret that the upward field-aligned current region corresponds to the soft electron precipitation region, the equatorward movement and intensification of the Birkeland currents with narrower latitude width is consistent with the auroral observations of the equatorward movement, brightening and narrowing of the electron and proton emissions.

Our results also show that the cross-tail current sheet region maps into the ionosphere in the transition area between the region-1 and region-2 currents. As observed by satellites substorms are initiated in the near-Earth plasma sheet region by a low frequency instability, which was identified as kinetic ballooning instabilities [*Cheng and Lui*, 1998a, 1998b]. Our stability theory and calculations show that the kinetic ballooning instability is expected to be unstable for field lines in the current sheet at the end of the growth

phase, consistent with observations. Thus, the ionospheric region where the field lines in the cross-tail current sheet are mapped to should be the auroral substorm onset location. This is consistent with auroral substorm observations that the auroral breakup is initiated within a 1° to 2° wide latitude region of the intense proton emission near the equatorward edge of the intense soft electron precipitation region [*Samson et al.*, 1992a]. Thus, the study of the 3D growth phase magnetospheric structure with a thin current sheet in the near-Earth plasma sheet region is critical in understanding the excitation mechanism of kinetic ballooning instabilities that initiate the substorm onset [e.g., *Cheng and Lui*, 1998a, 1998b; *Chen et al.*, 2003]. Although there have been several efforts to study these questions, the answers have not been achieved until recently [*Cheng and Zaharia*, 2003b].

3.1. Previous Efforts in Modeling the Near-Earth Plasma Sheet Region with Current Sheet

Previous studies of current sheet structure in the near-Earth plasma sheet region were mostly performed by employing local measurements of magnetic field and plasma from a single satellite orbiting in the vicinity of the equatorial plane [*Sergeev et al.*, 1990; *Lui et al.*, 1992; *Sergeev et al.*, 1993a; *Lui*, 1993; *Pulkkinen et al.*, 1994; *Sanny et al.*, 1994; *Sergeev et al.*, 1998; *Pulkkinen et al.*, 1999; *Kaufman et al.*, 2001, 2002; *Kubyshkina et al.*, 2002]. The observed magnetic fields were fitted with the 2D modified Harris current sheet model or empirical 3D field models to estimate the current sheet structure information such as the north-south thickness of the current sheet, the magnetic field curvature at the center of the current sheet, and the current density distribution of the current sheet. Unfortunately, the 2D modified Harris current sheet model or empirical 3D field models might be unrealistic in modeling the magnetic field structure in the near-Earth plasma sheet region during the substorm growth phase. This has been demonstrated by our modeling results of 3D magnetospheric configuration during the growth phase which show that the 3D current sheet structure in the near-Earth plasma sheet region

is substantially different from the Tsyganenko T-96 model [*Tsyganenko and Stern*, 1996] under disturbed time conditions (see the discussion in Subsection 3.2 and the panels (b) and (c) in Fig. 5) or the 2D modified Harris current sheet model.

With the assumption that the flow energy is much smaller than the magnetic field energy or the plasma thermal energy, there have been several theoretical efforts trying to explain the formation and structure of the thin current sheet. Most studies of the thin current sheet [e.g., *Hau*, 1991; *Wiegelmann and Schindler*, 1995; *Becker et al.*, 2001; *Birn and Schindler*, 2002] investigated the currents in the tail region beyond $20\,R_E$, and only a few modeling studies [e.g., *Erickson*, 1992; *Lee et al.*, 1995] have looked at the current sheets closer to Earth at $X \simeq -10\,R_E$. However, these studies assumed either 2-D axisymmetry or symmetry in the Y-direction, missing the formation of the field-aligned currents (an intrinsic 3-D effect, as explained by *Cheng* [1995]). Most studies consider the magnetospheric evolution during the growth phase to be dictated by "adiabatic convection" [e.g., *Wolf*, 1983] whereby the entropy, related to the quantity $S = PV^{\gamma}$, is conserved (P is the pressure, V the magnetic flux tube volume per unit flux, $V = \int ds/B$, with the integral performed along a magnetic field line; $\gamma = 5/3$). With entropy conservation constraints a very thin current sheet in the far tail can form for example due to deformations of the magnetopause boundary [*Birn and Schindler*, 2002]. During the substorm growth phase there are observational indications in the inner tail ($X > -15\,R_E$) [e.g., *Borovsky et al.*, 1998] that the entropy conservation is violated. Without entropy conservation, a process called entropy anti-diffusion has been proposed [*Lee et al.*, 1998] to explain thin current sheet formation in 2D with symmetry in the Y-direction. The magnetospheric evolution in the model of *Lee et al.* [1998] is however characterized by significant flows, a result not supported by observations during the growth phase. It should be noted that these modeling efforts were performed in 2D geometries.

3.2. Modeling of 3D Magnetosphere with Current Sheet in the Near-Earth Plasma Sheet Region

Recently, we have modeled quasi-static equilibrium magnetospheric states during the substorm growth phase by employing MAG-3D, a 3D quasi-static magnetospheric equilibrium code, which solves the 3D force-balance equation $\mathbf{J} \times \mathbf{B} = \boldsymbol{\nabla} P_\perp + \boldsymbol{\nabla} \cdot [(P_\perp - P_\parallel)\hat{\mathbf{b}}\hat{\mathbf{b}}]$, where $P_\perp$ is the perpendicular plasma pressure, $P_\parallel$ is the parallel plasma pressure and $\hat{\mathbf{b}}$ is the unit vector along a magnetic field line, in a domain inside the boundaries of magnetic flux surfaces [*Cheng*, 1995; *Zaharia et al.*, 2003]. Instead of employing the entropy evolution concept, the plasma pressure distributions in the equatorial plane such as those based on observations are specified as an input to the MAG-3D code. We have performed MAG-3D calculations with anisotropic pressure distributions. Recently, by assuming an isotropic pressure with $P = P_\perp = P_\parallel$, we have investigated the formation of thin current sheet in the near-Earth plasma sheet region during the substorm growth phase and obtained 3D equilibria with a thin current sheet located at around $X = -8R_E$ [*Zaharia and Cheng*, 2003]. For comparison purpose we present below the 3D magnetospheric structures for both the quiet time state (an example is shown in Figs. 3 and 4) and the state during the growth phase (an example is shown in Figs. 5 and 6).

An intrinsic feature of the three-dimensional magnetospheric structure is the existence of Birkeland currents, which are field-aligned currents linking the Earth's polar ionosphere with more distant magnetospheric plasma. Observations [*Iijima and Potemra*, 1976a, 1976b] indicate that near Earth they flow in broad sheets, roughly aligned with the aurora oval. Those sheets form two large current systems: region 1 entering on the morning side of the polar cap and flowing out on the afternoon side and region 2 further equatorward but with opposite polarities. At noon and midnight the current systems overlap in complicated ways, and during substorms region 1 on the nightside is reinforced by a "substorm wedge," which covers a limited sector in longitude. It is

now generally believed that the region 2 currents originate from the closed field line region where the plasma convective flow is slow in comparison with the thermal speeds. The sources of the region 1 currents are still being debated. In our 3D study we found that the sources of the region 1 currents also originate from the closed field line regions in the plasma sheet. The distribution of Birkeland currents depends critically on the equatorial pressure distribution and our results are consistent with direct observations of the Birkeland current distribution for the quiet times and particle precipitation pattern during the substorm growth phase. **Figure 2.**

3.2.1. 3D Magnetospheric Equilibrium Equations and Current System

If the plasma convection is small, the quasi-static magnetospheric equilibrium with isotropic pressure is described in the rationalized EMU unit by the system of equations: $\mathbf{J} \times \mathbf{B} = \boldsymbol{\nabla} P$, $\boldsymbol{\nabla} \times \mathbf{B} = \mathbf{J}$, and $\boldsymbol{\nabla} \cdot \mathbf{B} = 0$, where P is the plasma pressure and $\hat{\mathbf{b}}$ is the unit vector along a magnetic field line [*Cheng*, 1995; *Zaharia et al.*, 2003]. Assuming that the three-dimensional magnetospheric equilibrium has nested magnetic surfaces and has no toroidal flux, the magnetic field can be expressed in a straight field line (ψ, α, χ) flux coordinate (shown in Figure 2) as $\mathbf{B} = \boldsymbol{\nabla}\psi \times \boldsymbol{\nabla}\alpha$, where the Euler potential ψ is the magnetic flux function, the Euler potential $\alpha = \phi - \delta(\psi, \alpha, \chi)$ is an angle-like function, χ is a generalized poloidal angle, ϕ is the toroidal angle in the cylindrical (R, ϕ, Z) coordinate, and $\delta(\psi, \alpha, \chi)$ is periodic in both ϕ and χ. Note that near the Earth's surface, a constant ψ surface corresponds to an L-shell of the dipole field, and α corresponds to the longitudinal angle. The intersection of constant ψ and α surfaces defines the magnetic field line. The Jacobian is given by $\mathcal{J} = (\boldsymbol{\nabla}\psi \times \boldsymbol{\nabla}\alpha \cdot \boldsymbol{\nabla}\chi)^{-1}$. The flux coordinate system is in general not orthogonal, and $\boldsymbol{\nabla}\psi \cdot \boldsymbol{\nabla}\chi \neq 0$, $\boldsymbol{\nabla}\psi \cdot \boldsymbol{\nabla}\alpha \neq 0$, and $\boldsymbol{\nabla}\alpha \cdot \boldsymbol{\nabla}\chi \neq 0$. Within a magnetic surface the poloidal flux is $\int d^3x \mathbf{B} \cdot \boldsymbol{\nabla}\chi / 2\pi = 2\pi\psi$. Note that α is a cyclic function with a period of 2π for all constant ψ surfaces. This property allows the general three-dimensional equilibrium equations to be reduced to

quasi two-dimensional equations in the flux coordinate system, thus greatly simplifying the computational complexity.

Because $\mathbf{B}\cdot\boldsymbol{\nabla}P=0$, the pressure is constant along the field line and $P=P(\psi,\alpha)$. The $\mathbf{B}\times\boldsymbol{\nabla}\psi$ component of the force balance equation gives the current density in the $\boldsymbol{\nabla}\psi$ direction,

$$\mathbf{J}\cdot\boldsymbol{\nabla}\psi=\boldsymbol{\nabla}\cdot[(\nabla\psi)^2\boldsymbol{\nabla}\alpha-(\boldsymbol{\nabla}\alpha\cdot\boldsymbol{\nabla}\psi)\boldsymbol{\nabla}\psi]=-\frac{\partial P}{\partial\alpha}, \tag{1}$$

which is a two-dimensional elliptic equation on each constant ψ surface. In the two-dimensional axisymmetric limit, (1) is trivially satisfied by $\alpha=\phi$. The $\boldsymbol{\nabla}\psi$ component of the force balance equation gives the ring current and the generalized Grad-Shafranov equation,

$$\mathbf{J}\cdot\boldsymbol{\nabla}\alpha=\boldsymbol{\nabla}\cdot[(\boldsymbol{\nabla}\alpha\cdot\boldsymbol{\nabla}\psi)\boldsymbol{\nabla}\alpha-(\nabla\alpha)^2\boldsymbol{\nabla}\psi]=\frac{\partial P}{\partial\psi}, \tag{2}$$

which is a two-dimensional elliptic equation on each constant α surface. Note that in general (1) and (2) are three-dimensional equations. However, by choosing the (ψ,α,χ) coordinate system we have reduced the dimensionality of (1) and (2) to two dimensions. Equations (1) and (2) form a coupled set of equations that determine α and ψ, and can be solved by specifying α and ψ on the computational boundary and $P(\psi,\alpha)$ or its equatorial distribution.

From the charge neutrality condition, $\boldsymbol{\nabla}\cdot\mathbf{J}=0$, the field-aligned current density equation can be computed from

$$\mathbf{B}\cdot\boldsymbol{\nabla}\left(\frac{J_\parallel}{B}\right)=\frac{2\boldsymbol{\kappa}\times\mathbf{B}\cdot\boldsymbol{\nabla}P}{B^2}=\frac{\boldsymbol{\nabla}B^2\times\mathbf{B}\cdot\boldsymbol{\nabla}P}{B^4}, \tag{3}$$

where $J_\parallel\equiv\mathbf{J}\cdot\hat{\mathbf{b}}$ is the field-aligned current density, $\boldsymbol{\kappa}=\hat{\mathbf{b}}\cdot\boldsymbol{\nabla}\hat{\mathbf{b}}$ is the magnetic field curvature, and $\hat{\mathbf{b}}$ is a unit vector along a magnetic field line. $J_\parallel$ can be obtained by integrating (3) along the field line. The right hand sides of (3) represent the source of the field-aligned current density which originates from the component of the particle guiding-center $\boldsymbol{\nabla}B$ and curvature drifts perpendicular to the pressure gradient direction. In the axisymmetric limit, $\boldsymbol{\kappa}\times\mathbf{B}$ is in the $\boldsymbol{\nabla}\phi$ direction, the right hand side of (3) is

zero, and hence $J_\parallel = 0$ everywhere.

Assuming that there is a north-south symmetry, the current density can be expressed in the differential form [*Grad*, 1964; *Heinemann and Pontius, Jr.*, 1990]

$$\mathbf{J} = \boldsymbol{\nabla} V \times \boldsymbol{\nabla} P, \tag{4}$$

where V is periodic in α and satisfies the magnetic differential equation, $\mathbf{B} \cdot \boldsymbol{\nabla} V = 1$. In the (ψ, α, χ) flux coordinate system $dV = ds/B = \mathcal{J} d\chi = d^3x/(d\psi d\alpha)$, where ds is the element of arc length along the magnetic field line. Thus, integrating along the field line V has the physical meaning of the magnetic flux tube volume per unit flux area $(d\psi d\alpha)$. With north-south symmetry, $J_\parallel = \mathbf{B} \cdot \boldsymbol{\nabla} \chi = 0$ at the equator, and the field-aligned current density at the ionosphere can be expressed in terms of the equatorial quantities as [*Vasyliunas*, 1970; *Birmingham*, 1992]

$$\begin{aligned} J_{\parallel i}/B_i &= \mathbf{B}_e \cdot \boldsymbol{\nabla}_e V(\psi, \alpha, e, i) \times \boldsymbol{\nabla}_e P/B_e^2 + \\ &\quad (\mathcal{J}\mathbf{B} \cdot \boldsymbol{\nabla}\chi \times \boldsymbol{\nabla} P)_i/B_i^2, \end{aligned} \tag{5}$$

where $V(\psi, \alpha, e, i) = \int_{\chi_e}^{\chi_i} \mathcal{J} d\chi$, the subscripts e and i denote that the quantities are evaluated at the equator and the ionosphere, respectively. Note that with east-west symmetry, $J_\parallel$ is zero in the noon-midnight meridian plane. As pointed out by *Birmingham* [1992] the second term is missing in the expression given by *Vasyliunas* [1970], and it is much smaller than the first term by a factor of L^{-6}, where L is the equatorial distance of the field line.

From (4) we have $\mathcal{J}\mathbf{J} \cdot \boldsymbol{\nabla}\chi = (\partial V/\partial\psi)(\partial P/\partial\alpha) - (\partial P/\partial\psi)(\partial V/\partial\alpha)$. Because P and V are periodic in α, $\int_0^{2\pi} d\alpha \mathcal{J}\mathbf{J} \cdot \boldsymbol{\nabla}\chi = 0$. Therefore, $I_p = (1/2\pi) \int d^3x \mathbf{J} \cdot \boldsymbol{\nabla}\chi = 0$, and there is no net poloidal current across a constant χ surface such as the planetary ionosphere.

3.2.2. Numerical Method foe Solving 3D Magnetospheric Equilibrium Equations

Equations (1) and (2) can be cast into inverse equilibrium equations in terms of a (ψ, α, χ) flux coordinate system [*Cheng*, 1992]. A three-dimensional magnetospheric equilibrium code, the *MAG-3D* code, has been developed to solve the coupled nonlinear inverse equilibrium equations [*Cheng*, 1995; *Zaharia et al.*, 2003]. The choice of $ds/d\chi = \mathcal{J}B = F(\psi, \alpha)$ gives an equal arc length coordinate system. The numerical grid is tied to the equilibrium solution in such a way that grid points automatically accumulate in regions of steep gradients, thus yielding accurate solutions of high-β_{eq} magnetospheric equilibria. An iterative metric method is used to solve for the discrete rectangular coordinate $[x(\psi, \alpha, \chi), y(\psi, \alpha, \chi), z(\psi, \alpha, \chi)]$ of constant ψ and α surfaces such that the finite-differenced inverse equilibrium equations based on these points are satisfied to a small tolerance.

We consider a fixed boundary problem with the computational domain bounded by: (a) an outer $\psi = \psi_{\text{out}}$ flux boundary with its shape specified to take into account the effects of the solar wind and the interplanetary magnetic field; (b) an inner $\psi = \psi_{\text{in}}$ boundary determined by the dipole magnetic field; and (c) the Earth's surfaces between ψ_{in} and ψ_{out} surfaces. The boundary condition on the Earth's surface is $\alpha = \phi$. In the computational domain, a (ρ, ζ, χ) flux coordinate is chosen with $0 \leq \chi \leq \pi$, $0 \leq \zeta \leq 2\pi$, and $0 \leq \rho \leq 1$, where $\psi = \psi(\rho)$ and $\alpha = \alpha(\zeta)$ are chosen such that uniform ρ and *zeta* grids give optimal equatorial radial and azimuthah grids for the computational purpose. The magnetic field is normalized by the equatorial dipole magnetic field intensity B_D at $R = R_o$. The magnetic flux is chosen to be $\psi_{\text{out}} \equiv -B_D R_o^3 / R_{\max}$ at the outer magnetic surface and $\psi_{\text{in}} \equiv -B_D R_o^3 / R_{\min}$ at the inner magnetic surface. The boundary ψ surfaces, $\psi = \psi_{\text{out}}$ and $\psi = \psi_{\text{in}}$, delimiting the computational domain have specified shapes, usually obtained from empirical models such as T96 [*Tsyganenko and Stern*, 1996] for various solar wind and IMF conditions. The equatorial plasma pressure distribution will

be specified by using the empirical observations for the quiet time case [*Lui and Hamilton*, 1992; *Spence and Kivelson*, 1993; *Lui et al.*, 1994] with modifications including azimuthal variation. For the growth phase case, due to very limited observations, the equatorial plasma pressure distribution will be modeled by adding pressure over the quiet time distribution to simulate the observed pressure enhancement in the plasma sheet [*Lui et al.*, 1987; *Kistler et al.*, 1992].

Figure 3.

3.2.3. Modeling Results of the Quiet Time Magnetosphere

For the quiet-time case we use the inner and outer boundary shapes for ψ obtained by field-line tracing using the T96 model, with parameters $Dst = -5\,\mathrm{nT}$, $P_{\mathrm{SW}} = 2.1\,\mathrm{nPa}$, $B_{\mathrm{yIMF}} = 0$ and $B_{\mathrm{zIMF}} = 1\,\mathrm{nT}$, representing average quiet-time parameters as obtained from the OMNI solar wind database. For the equatorial pressure P distribution we choose the following form in the equatorial plane:

$$P(R,\phi,Z=0) = 89e^{-0.59R}\left[A + Be^{-\left(\frac{\phi-\pi}{\Delta\phi}\right)^2}\right] + 8.9R^{-1.53}\left[C + De^{-\left(\frac{\phi-\pi}{\Delta\phi}\right)^2}\right], \qquad (6)$$

where R, ϕ, Z define the usual cylindrical coordinate system with Earth as the origin and $\phi = \pi$ at midnight, while A, B, C, D and $\Delta\phi$ are constants. We choose $A = B = 0.5$, $C = 2$, $D = -1$ and $\Delta\phi = 0.5\pi$, such that for $\phi = \pi$ Eq. (6) recovers the Spence-Kivelson empirical formula [*Spence and Kivelson*, 1993], which is based on observations at midnight as shown in the top panel of Fig. 3(a). At the same time, since the first term on the right hand side of Eq. (6) dominates close to Earth ($R < 10\,R_E$), while the second term farther in the tail, Eq. (6) also simulates for a given R an azimuthal maximum in P at midnight close to Earth, and an azimuthal minimum farther in the tail. This qualitative local-time dependence, seen in the equatorial P contours in Fig. 4(b), is justified by observations showing a maximum in P at midnight close to Earth [*De Michelis et al.*, 1999, e.g.,], but a slight minimum at midnight for $R > 10\,R_E$ (see Fig. 11 of [*Tsyganenko and Mukai*, 2003]).

We will only briefly summarize the physical parameters of the computed quiet-time state. The cross-tail current ($J_\phi = \mathbf{J} \cdot \boldsymbol{\nabla}\phi/|\boldsymbol{\nabla}\phi|$) has a maximum $J_\phi \approx 2.4\,\mathrm{nA/m^2}$. Fig. 3 shows (a) the profiles of P, B and plasma β along the Sun-Earth axis; (b) the magnetic field lines in the noon-midnight meridian plane; (c) noon-midnight meridian plane contours of J_ϕ in $\mathrm{nA/m^2}$; and (d) plasma β contours in the noon-midnight meridian. **Figure 4.**

The Birkeland currents in the northern ionosphere are shown in Fig. 4(a) with $J_\parallel > 0$ indicating the current is flowing into the ionosphere. The region-2 currents span a broad area, but are very weak ($J_{\parallel 2\mathrm{max}} = 0.07\,\mu\mathrm{A/m^2}$) — consistent with observations [*Iijima and Potemra*, 1976a] showing their virtual disappearance during quiet times. On the other hand, a narrower region-1 current pattern exists at higher latitudes ($\sim 68°$), with maximum densities ($\approx 0.5\,\mu\mathrm{A/m^2}$) at 23:00 and 02:00 magnetic local time (MLT), again agreeing very well with quiet-time observations [*Iijima and Potemra*, 1976a]. The region-1 and region-2 current formation mechanism is easily understood from the Vasyliunas relation [*Vasyliunas*, 1970], Eq. (5) by neglecting the small second term on the right hand side. The quantity $(\mathbf{B} \cdot \boldsymbol{\nabla} V \times \boldsymbol{\nabla} P)_{eq}$ has opposite signs for region-1 versus region-2 current formation, as seen in Fig. 4(b), which shows the contours of constant P and V over a color plot of J_ϕ in the equatorial plane and the orientation of the vectors $\boldsymbol{\nabla} P$ and $\boldsymbol{\nabla} V$ at two locations that map into the ionosphere in regions of opposite $\mathbf{J}_\parallel$. **Figure 5.**

3.2.4. Modeling Results of the Growth Phase Magnetosphere

For modeling a substorm growth phase configuration, the ψ boundary shapes are obtained again from T96 with $P_{SW} = 5\,\mathrm{nPa}$, $B_{\mathrm{ZIMF}} = -5\,\mathrm{nT}$, $B_{\mathrm{YIMF}} = 0.5\,\mathrm{nT}$ and $Dst = -50\,\mathrm{nT}$, typical for disturbed times. There are only scarce plasma pressure observations during the growth phase. While P generally increases with activity throughout the plasma sheet [e.g., *Tsyganenko and Mukai*, 2003], observations [e.g. *Spence et al.*, 1989; *Kistler et al.*, 1992] as well as convection simulations [*Wang et al.*, 2003] show that the pressure enhancement is larger at smaller radial distances. Another

property, both observed [*Wing and Newell*, 1998; *Tsyganenko and Mukai*, 2003] and apparent in simulations [*Wang et al.*, 2003, e.g.,], is the earthward expansion of regions with azimuthal minimum P at midnight (for fixed equatorial distance R). We thus choose the P distribution in the equatorial plane as

$$P(R,\phi,Z=0) = 12.5e^{-0.25R}\cdot\left[A + B\tanh\left(\frac{x_1 - R}{\Delta R}\right)e^{-\left(\frac{\phi-\pi}{\Delta\phi}\right)^2}\right] + 8.9R^{-1.53}\left[C + De^{-\left(\frac{\phi-\pi}{\Delta\phi}\right)^2}\right] \tag{7}$$

We choose $A = 1.25$, $B = 0.75$, $C = 3$, $D = -2$, $\Delta\phi = 0.3\pi$, $x_1 = 10$ and $\Delta R = 1.25$ in Eq. (7) to model the equatorial pressure distribution in the late growth phase. The resulting P profile along the Sun-Earth axis, shown by solid lines in Fig. 5(a), is about twice the quiet-time value tailward of $10\,R_E$, and even more enhanced at the inner edge of the plasma sheet. Note that the dashed lines in Fig. 5(a) are the quiet time values presented in Fig. 3(a) and are presented for comparison purpose. The equatorial P contours, shown in Fig. 6(b), show the earthward expansion of regions with P minimum (for a given R) at midnight, and at the same time the more pronounced azimuthal minima in P as compared to the quiet-time case.

Figure 5 shows several quantities in the obtained force-balanced state. The solid lines in Fig. 5(a) show profiles of P, B and β along the Sun-Earth axis. The quiet time profiles (dashed lines) are also shown for comparison. We notice the appearance of a local magnetic well, with $B_{\min} \approx 15\,\mathrm{nT}$, between $X = -7\,R_E$ and $X = -9\,R_E$. In the magnetic well, plasma β peaks at $\beta \approx 45$ near $X = -8\,R_E$. The magnetic field is extremely tail-like in the near-Earth plasma sheet, as seen in Fig. 5(b). For comparison purpose the magnetic field lines of the T-96 model field are shown in Fig. 5(c), which are substantially different from the equilibrium tail-like field lines in the near-Earth region between $X = -6\,R_E$ and $X = -10\,R_E$. The tail-like field in the near-Earth region suggests a thin current sheet, which can indeed be seen in Fig. 5(d), which shows noon-midnight meridian plane contours of J_ϕ. The maximum current density is $J_{\phi_{\max}} \approx 11\,\mathrm{nA/m^2}$, and the sheet has a north-south half-width of $1\,R_E$ at $X = -8\,R_E$. Finally, from Fig. 5 (e) one notices that

the plasma β is very large in the vicinity of the equatorial plane. **Figure 6.**

The Birkeland currents in this state are shown in Fig. 6(a). Both the region-1 and region-2 currents have moved to lower latitudes compared to the quiet-time case shown in Fig. 4(a), and are much more intense (with the intense $J_{\parallel}$ regions quite peaked in latitudinal extent). The region-2 current has a maximum density of $1.2\,\mu\mathrm{A/m^2}$ at 22:00 and 02:00 MLT, and stretches between 60° and 62° in latitude. The region-1 current is found between 62° and 65° and has a maximum of $3.5\,\mu\mathrm{A/m^2}$ closer to midnight (22:30 and 01:30 MLT). Again, the different signs of $(\mathbf{B}\cdot\boldsymbol{\nabla}V\times\boldsymbol{\nabla}P)_{eq}$ in the region-2 and region-1 current regions, respectively, are readily seen in Fig. 6(b), which shows the contours of constant P and V over a color plot of J_ϕ in the equatorial plane and the orientation of the vectors $\boldsymbol{\nabla}P$ and $\boldsymbol{\nabla}V$ at three locations. One also observes that the strong cross-tail current sheet region (with $J_\phi \geq 0.5J_{\phi max}$) surrounded by a closed curve in the equatorial plane as shown in Fig. 6(b) maps into the northern ionosphere into the transition area (inside a closed curve) between region-1 and region-2 current regions as shown in Fig. 6(a).

3.2.5. Summary and Discussion of the Growth Phase Magnetosphere Modeling Results

The magnetospheric configuration for the substorm growth phase case is substantially different from the quiet time case as a result of the plasma pressure enhancement in the plasma sheet. In particular, a thin current sheet with $J_\phi \sim 10\,\mathrm{nA/m^2}$ is formed in the near-Earth plasma sheet with an radial extent between $X = -6\,R_E$ and $X = -10\,R_E$, and the azimuthal extent between $Y = -5\,R_E$ and $Y = 5\,R_E$, and a half-thickness $\sim 1\,R_E$, in the north-south direction. Associated with the current sheet region is the formation of a local magnetic well and a local enhancement of β_{eq} (≥ 50) due to high plasma pressure. The spatial distribution and location of the current sheet change with different pressure distributions. In general, we expect the center of the near-Earth

current sheet to be located radially somewhere between $X = -6\,R_E$ and $X = -12\,R_E$. The substorm growth phase configuration is also characterized by the region-1 and region-2 Birkeland currents moving toward lower latitudes (60° – 65°), and being more intense (region-1 $J_{\parallel 1\,\max} \sim 3\,\mu\mathrm{A/m}^2$) compared to quiet times.

To compare the modeling results of the 3D growth phase magnetosphere, we recognize that the soft electron precipitation roughly tracks with the upward Birkeland current in the ionosphere. Thus, the equatorward movement and intensification of the Birkeland current obtained in the modeled growth phase magnetospheric configuration agrees with the observed equatorward movement and intensification of the auroral electron and proton emissions. Moreover, the 3D calculation shows that the cross-tail current sheet region maps into the ionosphere in the transition area between the region-1 and region-2 currents. As will be shown in the next Section that the kinetic ballooning instability is expected to be unstable for field lines in the current sheet region as observed by satellites in the near-Earth plasma sheet region. Thus, we expect the transition area between the region-1 and region-2 currents mapped from the current sheet region to be the onset location of auroral breakup in the ionosphere. This is consistent with the auroral onset observations that the auroral breakup location and the arc are within the region of intense proton precipitation near the equatorward edge of the electron emissions.

The total magnetic energy in the plasma sheet can be considered as a measure of the capacity of the plasma sheet magnetic field (container) to contain plasma thermal energy. It is thus important to discuss the change of magnetic and plasma thermal energy in the plasma sheet from the quiet time configuration to the growth phase configuration. Based on our equilibrium solutions, we calculated the total magnetic field energy and plasma thermal energy within spatial domains bounded by two specified flux surfaces which correspond to two fixed magnetic latitudes (or L-shells) in the ionosphere. The chosen flux surfaces correspond to the inner and outer flux surfaces of the computational boundary of the growth phase case with the ionospheric latitude angles with $\theta_{in} = 57.7°$

(dipole $L = 3.5$) and $\theta_{out} = 64.5°$ (dipole $L = 5.4$). The field lines in the outer flux surface stretch out to $X = -18.5\,\mathrm{R_E}$ at the midnight. Note that for the quiet time case, the midnight field line of the $L = 5.42$ flux surface extends only to $X = -10.5\,\mathrm{R_E}$. Thus, because of the further stretching of field lines during the growth phase, the volume bounded by these two specified flux surfaces increases about 7 times from $70.8\,\mathrm{R_E}^3$ for the quiet time case to $490\,\mathrm{R_E}^3$ for the growth phase. We note that, for the quiet time case the midnight field line, that extends to the same equatorial distance of $X = -18.5\,\mathrm{R_E}$ for the growth phase case, resides in a flux surface with $\theta = 68.6°$ (dipole $L = 7.3$). The volume bounded by the surfaces of the $L = 3.5$ and $L = 7.3$ fluxes for the quiet time case is larger ($\approx 695\,\mathrm{R_E}^3$). For the quiet time configuration the total magnetic energy within the surfaces of the $L = 3.5$ and $L = 5.4$ fluxes is $W_B = 5.6 \times 10^{20}$ erg, and the total plasma thermal energy is $W_P = 2.7 \times 10^{20}$ erg. However, for the growth phase configuration $W_B = 1.9 \times 10^{21}$ erg and $W_P = 2.7 \times 10^{21}$ erg. Thus, the magnetic container (bounded by these two magnetic fluxes) stores ten times more plasma thermal energy with an increase of 3.3 times in the magnetic energy mainly due to the increase in volume. However, the average magnetic energy density decreases in the growth phase from the quiet time case, but the average plasma thermal energy density increases.

Also, we can estimate the total energy dissipated in the ionosphere during the substorm expansion, which is given by $\mathcal{E}_i = \int dt d^3x \mathbf{J}_{jet} \cdot \mathbf{E}_{jet}$, where $\mathbf{J}_{jet}$ and $\mathbf{E}_{jet}$ are the westward electrojet current density and electric field in the substorm current wedge, respectively, the time integration is over the expansion phase. The upper bound of $\mathcal{E}_i$ can be estimated to be $I_{jet} V_{jet} \Delta t$, where I_{jet} is the total auroral electrojet current, V_{jet} is the potential drop over the current wedge region, and Δt is the time span of the expansion phase. From observations the maximum I_{jet} ranges from 0.08 to 1 MA for many substorms surveyed [*Kamide*, 1998]. If we consider $I_{jet} = 1\,\mathrm{MA}$, $\Delta t = 10$ minutes and assume $V_{jet} = 5\,\mathrm{kV}$, then $\mathcal{E}_i \leq 1.8 \times 10^{20}$ erg, which is much smaller than the energy change in the plasma sheet during the expansion phase, which is estimated to be the

difference in the plasma sheet energy between the growth phase case and the quiet time case because the plasma sheet recovers to the pre-growth phase condition. In the next section we will show that the growth phase configuration is expected to be unstable to the kinetic ballooning instability in the cross-tail current sheet region.

The near-Earth cross-tail current sheet thickness is in good agreement with satellite observations [*Sanny et al.*, 1994] showing the current sheet being wider than $1\,R_E$ throughout the growth phase. This result differs from the popular belief that the sheet thickness is on the order of an ion gyro-radius ($\rho_i \leq 1000\,\mathrm{km}$). It is unlikely that such currents can be found in a force-balanced configuration in the transition region between the dipole-like and tail-like magnetic field. Among the reasons for this, we note that direct evidence of extremely thin current sheets is scarce — most observations measure the **B**-field and try to fit it with an unrealistic very thin Harris current sheet, without discussing whether a thicker sheet might suffice. Secondly, observations in the near-Earth plasma sheet at $X \approx -8\,R_E$ by AMPTE/CCE [*Lui et al.*, 1992] show that the angle between the B_z and B_x components of **B** is never less than 40° during the substorm growth phase (except during the "explosive growth phase" of roughly 30 sec period just before the substorm onset [*Ohtani et al.*, 1992]). In the "explosive growth phase" the perturbed magnetic field associated with the kinetic ballooning instability (KBI) has already reached a large amplitude and the estimate of current sheet thickness based on the observed magnetic field in the "explosive growth phase" is distorted by the KBI signal and thus such an estimate does not represent the true current sheet thickness [*Cheng and Lui*, 1998a, 1998b]. Moreover, we note that the current sheet does not need to become thinner than $\sim 0.5\,R_E$ in order to lead to substorm onset by the KBI [*Cheng and Lui*, 1998a, 1998b]; indeed, in our current sheet region plasma β_{eq} (~ 50) is already sufficiently large for a kinetic ballooning instability to be excited and lead to onset.

Based on our study, the scenario for current sheet formation in the near-Earth plasma sheet region is the following: during the growth phase, the larger solar wind

P_{SW} and increased flux merging at the magnetopause leads to enhanced tail stretching. At the same time, plasma pressure in the near-Earth plasma sheet greatly increases due to enhanced convection, leading to larger pressure gradients. Due to the strong stretching of the tail flux tubes, the difference $\Delta\psi$ between $\psi_{\rm out}$ (the flux on the outer boundary at $R \approx 18.5\,R_E$) and $\psi_{\rm in}$ (on the inner boundary at $R \approx 3.5\,R_E$) becomes smaller compared to quiet times. The increase in $|\partial P/\partial R|$ coupled with the decrease in $\partial\psi/\partial R$ leads to very large $|\partial P/\partial\psi|$ and thus current densities (at midnight $\alpha = \phi$ and $J_\phi = \mathbf{J}\cdot\boldsymbol{\nabla}\phi/|\boldsymbol{\nabla}\phi| = R\partial P/\partial\psi$) localized in the near-Earth plasma sheet. In our study a large gradient in the flux volume $V = \int ds/B$ is not needed in order to have large $|\partial P/\partial\psi|$, unlike in adiabatic formalisms of current sheet formation such as the "gradient of flux volume mechanism" (GFVM) [*Wiegelmann and Schindler*, 1995].

Finally, we point out that the formation of breakup discrete arc in the strong proton precipitation region in the late growth phase is not discussed in this paper. In our opinion, the formation of breakup discrete arc in the strong proton precipitation region is related to the structure of cross-tail current sheet in the near-Earth plasma sheet region. It is possible that the kinetic ballooning instability that is excited in the cross-tail current sheet can be directly related to the arc, which sometimes occurs just a few minutes prior to its breakup [*Lyons et al.*, 2002]. Another idea for the arc formation is based on the field line resonance as proposed by many authors [e.g., *Samson et al.*, 1992b; *Lui and Cheng*, 2001]. As the field line resonance is excited by compressional Alfvén waves that propagate to the resonant field lines, the wave energy is accumulated at these field lines, which form a resonant surface. Shear Alfvén waves propagate mainly along these resonant field lines and accelerate electrons to over 1 keV energy which produces a discrete arc. However, due to the observed very low resonant frequency (1.3 mHz) of these magnetic field oscillations associated with the arc, no satisfactory theory has been developed to provide a correct frequency calculation. However, we believe the resolution of this problem is within reach because we have developed a new theory of field line

resonance that takes into account the effects of coupling between slow mode and shear Alfvén wave due to plasma pressure and its gradient and the magnetic field curvature in high β_{eq} plasmas [*Cheng*, 2003; *Cheng and Zaharia*, 2003a]. This subject should be addressed in future studies.

4. Substorm Onset

In this section we will first describe observations by AMPTE/CCE satellite which clearly demonstrate that toward the end of late growth phase (approximately 3 minutes before the substorm onset of plasma turbulence and current disruption) the plasma pressure becomes isotropic and β_{eq} increases to ≥ 50 and a low frequency instability with a wave period of $\sim 50 - 75$ seconds (in the Pi 2 frequency range) is excited and grows exponentially to a large amplitude with $\delta B/B \geq 0.3$ at the onset of current disruption. The half wave period of the instability just before the current disruption onset corresponds to the explosive growth phase [*Ohtani et al.*, 1992]. At the current disruption onset higher frequency instabilities (with wave periods 15 sec, 10, sec, 5 sec, etc.) are also excited and they are identified as the cross-field current instability (CCI) [*Lui*, 1996] driven unstable by the velocity space free energy associated the enhanced ion drift which oscillates between westward and eastward directions during the current disruption phase. The low frequency instability combines with the higher frequency instabilities to form a strong turbulent state and the turbulence expands in all directions (but more in the tailward direction) in the equatorial plane through out the expansion phase. The strong turbulence causes anomalously fast plasma transport and heating and modifies the mean plasma pressure profile so that the ambient magnetic field recovers from a tail-like geometry to a dipole-like geometry. Associated with the dipolarization, an enhanced duskward electric field is produced, which causes dispersionless energetic particle injections observed by geosynchronous satellites.

It is emphasized that the initial excitation of the low frequency instability and the

subsequent generation of the secondary higher frequency instabilities occur in a localized equatorial area of less than 1 R_E in width in the near-Earth plasma sheet region [*Ohtani et al.*, 1991]. Because of such a localized onset region, satellites not located at the initiation region will not observe the exponential increase of the low frequency instability amplitude. Instead, they observe an abrupt increase of large amplitude fluctuations that result from the spatial expansion of the turbulence region [e.g., *Roux et al.*, 1991; *Erickson et al.*, 2000; *Shiokawa et al.*, 2003]. As we have proposed that the localized initiation region corresponds to the strong cross-tail current sheet region, where the kinetic ballooning instability is excited to cause the low frequency wave in the Pi 2 frequency range, which accelerate electrons to the ionosphere by its parallel electric field to cause the initial brightening in the discrete arc.

Two key issues need to be resolved in order to understand the physical processes of the substorm onset of the current disruption and subsequent magnetic field dipolarization: (1) the excitation mechanism and the high β_{eq} threshold ($\geq$ 50) of the observed low frequency instability that underlines the explosive growth phase prior to substorm onset; (2) the physical mechanism of the enhanced ion drift in the explosive growth phase that leads to excitation of higher frequency instabilities. To understand these two key issues, we will adopt the theory of kinetic ballooning instability (KBI), which results from the release of configuration space free energy of nonuniform pressure with gradient in the same direction as the magnetic field curvature in the cross-tail current sheet region of the near-Earth plasma sheet.

To explain the observed low frequency instability, theoretical investigations of the ballooning instability based on the ideal MHD model have been made previously [e.g., *Lee and Wolf*, 1992; *Ohtani and Tamao*, 1993; *Hurricane*, 1997; *Liu*, 1997; *Lee*, 1998; *Bhattacharjee et al.*, 1998; *Horton et al.*, 1999; *Lee*, 1999a]. All these ideal calculations employed simplified equilibria in 2D magnetospheric geometries and made simplified assumptions on the plasma compressibility to reduce the eigenmode equations from a

fourth order differential equation to a second order integro-differential equation. The stability of ballooning modes depends crucially on the equilibrium field structure and the assumption made on the plasma compressibility. Numerical calculations to examine the compressibility effect with different simplifying assumptions of the plasma compressibility [*Lee*, 1999a] have been performed for a 2D equilibrium model by *Voigt* [1986]. By assuming the parallel plasma displacement to be a finite constant along the field line [*Lee and Wolf*, 1992], the stability calculations predicted a low β_{eq} (≤ 1) threshold for instability. *Horton et al.* [1999] considered a different approximation for the plasma compressibility with the fast-MHD model which assumes that the wave propagates very fast along the ambient magnetic field such that there is not sufficient time for parallel plasma motion and the plasma displacement along **B** vanishes, and they concluded that the ballooning instability occurs for $\beta < 1$. However, the numerical stability calculations of the fast-MHD model performed by *Lee* [1999a] show that the ballooning mode is stable in the Voigt's equilibrium, which is in contradiction to the analytical conclusion of *Horton et al.* [1999]. Calculations with these simplifying compressibility model, but with a more stretched 2D equilibrium field model by *Kan* [1973] gave totally different results from the Voigt's equilibrium. These results clearly illustrate that to obtain the correct stability result even within the ideal MHD model it is essential to model the plasma compressibility correctly as well as the equilibrium field realistically.

Efforts to broaden the physics of plasma compressibility and the Hall effect in the Ohm's law have also been pursued [e.g., *Hurricane et al.*, 1994, 1995; *Horton et al.*, 1999; *Lee*, 1999a, 1999b]. For example, *Hurricane et al.* [1994, 1995] developed a kinetic formulation by considering that the particle orbits are stochastic and thus the particle magnetic moments are not conserved in the plasma sheet. They also assumed that the frequency of the ballooning mode is much smaller than both the electron and ion bounce frequencies, the particle gyroradii are much smaller than the mode perpendicular wavelength, and the parallel electric field vanishes. The stochastic particle orbit effect

shows up in the bounce-orbit average of the magnetic drift frequency by replacing it with its bounce and pitch-angle average. By further assuming that the wave frequency is smaller than the bounce and pitch-angle average of the magnetic drift frequency, a second-order integro-differential eigenmode equation was obtained with a simplified plasma compressibility term that takes into account the stochastic particle orbit effect. Numerical solutions of the eigenmode equation with model 2D equilibria show that the ballooning mode will be unstable for $\beta \geq O(1)$, which is not much different from those based the ideal MHD model with simplified assumptions on the plasma compressibility [*Lee*, 1999a]. Including the Hall effect in the Ohm's law only slightly increased the ballooning instability β_{eq} threshold by a few tens of percents [*Lee*, 1999b]. Thus, these previous MHD ballooning mode stability calculations could not explain the high β_{eq} value (≥ 50) [*Lui et al.*, 1995] when the low frequency instability was observed by AMPTE/CCE [*Cheng and Lui*, 1998a]. Moreover, the low β_{eq} threshold predicted by these previous ballooning mode stability calculations are in contradictory to the observed high β_{eq} values ($50 > \beta > 10$) observed throughout the late growth phase when no noticeable magnetic fluctuations were observed by AMPTE/CCE [*Takahashi et al.*, 1987b] in the enhanced cross-tail current sheet region.

There are additional drawbacks of these previous MHD ballooning stability calculations. For example, because of the use of 2D equilibria, there is no information on where in the equatorial plane the ideal ballooning instability would be initiated. The MHD ballooning mode theory would predict purely growing instabilities, and do not explain the observed frequency of the instability. Another fundamental drawback is that there is no parallel electric field, and thus the unstable MHD ballooning mode does not accelerate particles to produce the substorm onset auroral brightening as observed in the ionosphere. However, even with the above mentioned deficiencies, the ideal MHD model provides the valuable information of where in the plasma sheet the free energy and the most unstable ballooning instability are located when realistic 3D magnetospheric

equilibria are available. Thus, we will present calculations based on realistic 3D growth phase magnetospheric equilibria and the full MHD model without making assumptions on plasma compressibility. The calculations will demonstrate that the ballooning instability is most unstable in the strong cross-tail current sheet region in the near-Earth plasma sheet, which maps to the initial brightening location of the breakup arc in the ionosphere.

The full assessment of the stability of the ballooning mode in the magnetosphere requires the consideration of kinetic effects such as trapped particle dynamics, finite ion Larmor radii (FLR), parallel electric fields, wave-particle resonances, as well as correct ordering between the wave frequency with respect to the bounce frequencies of electrons and protons. We have developed a kinetic theory of ballooning mode by including these kinetic effects and considering the correct frequency ordering that the wave phase velocity along the ambient field line is smaller than the typical electron velocity, but larger than the typical ion thermal velocity [*Cheng and Lui*, 1998a, 1998b] as dictated by the observations from the particle and wave measurements of AMPTE/CCE. The kinetic ballooning instability theory properly explains the wave frequency, growth rate and high β_{eq} threshold ($\geq$ 50) of the low frequency instability observed by the AMPTE/CCE. Because the wave phase velocity along the field line is smaller than the electron thermal velocity, the trapped electron effect coupled with ion Larmor radius effects causes a large parallel electric field and thus a much enhanced parallel current which greatly enhances the stabilizing field line tension over the value expected from the MHD theory. As a result, a much higher β threshold than that based on the ideal MHD model is obtained with $\beta_c \geq O(10^2)\beta_c^{MHD}$, where β_c^{MHD} is the critical β_{eq} predicted by the MHD theory.

The effect of the wave-ion magnetic drift resonance with $\omega - \omega_{di} = 0$, where ω_{di} is the ion magnetic drift frequency, provides an additional channel to release the free energy and typically reduces β_c by up to 20%. Another consequence of the wave-particle resonance is to produce a perturbed ion distribution in the velocity space centered around $v_y = V_{di}$, where v_y is the particle velocity in the dusk direction and V_{di} is the average ion magnetic

(∇B and curvature) drift velocity. As KBI grows to a large amplitude, the perturbed ion velocity distribution increases so that $\partial f_i/\partial v_y > 0$ for $v_y \leq v_{di}$, which provides an additional free energy source for higher frequency instabilities such as cross-field current instability (CCI) [*Lui*, 1996]. As the higher frequency instabilities quickly grow to large amplitudes, they combine with KBIs to form a strong plasma turbulence, which leads to anomalously large plasma transport and heating in the current disruption phase. In a few minutes the pressure profile relaxes to a more quiet time-like profile, the magnetic field recovers to a more dipole-like geometry, and β_{eq} decreases. Thus, the new substorm scenario emphasizes a low-frequency mode (KBI) which can naturally account for the explosive growth phase and the initiation of subsequent current disruption through a combination of KBI and CCI.

Figure 7.

Figure 8.

4.1. Low Frequency Instability Observed by AMPTE/CCE

Evidence for the low-frequency perturbations occurring prior to current disruption onset can be found in the detailed examination of magnetic field during current disruption events. Figure 7 shows the components of the magnetic fluctuations in the cylindrical (V, D, H) coordinate from the magnetometers on board the AMPTE/CCE satellite for the June 1, 1985 substorm event [*Lui et al.*, 1992]. The satellite was in the midnight local time sector, MLT = 23.5, at a radial distance of approximately 8.8 R_E. It is obvious that the magnetic field is in a strong turbulence state with $\delta B/B \sim O(1)$ during the current disruption phase. Figure 8 shows the power spectrogram of the V component magnetic field by using the wavelet analysis and it clearly shows that a low frequency instability with frequency of about 20 mHz is excited at about 1.5 minutes before the onset of current disruption at 23:14:20 UT. To extract the low frequency components of the fluctuations, we employed successive smoothing of the original signals with normalized binomial coefficients as previously used in *Lui and Najmi* [1997], and the resultant low frequency magnetic fluctuations are shown in Figure 9. The low frequency magnetic

field perturbations in the cylindrical (V, D, H) components were then converted into components in the unperturbed magnetic field coordinate system to give δB_L, δB_ϕ, and $\delta B_\parallel$, where positive δB_ϕ is pointing eastward, positive $\delta B_\parallel$ is along the mean magnetic field direction and positive δB_L is in the third right-handed orthogonal direction. From Figure 9, one can deduce that the real frequency of the low-frequency perturbation is ~ 0.1 Hz (compared with proton cyclotron frequency of about 1 Hz) and the growth rate is about 0.2 of the real frequency. Note that the exponentially growing low-frequency perturbation begins quite early at $\sim$ 23:13:00 UT, about 1.5 minutes before the onset of current disruption. It is interesting to note that there is almost no magnetic field fluctuation before the low frequency instability was observed. The general characteristics of the low frequency perturbation given here have been found in several other current disruption events. Another substorm event was observed by AMPTE/CCE on August 30, 1986 [*Takahashi et al.*, 1987a; *Lui et al.*, 1992; *Ohtani et al.*, 1995] and the three components of the magnetic field are shown in Figure 10 and the corresponding low frequency magnetic field perturbations are shown in Figure 11. The AMPTE/CCE was in the midnight local time sector, MLT = 23.5, at a radial distance of approximately $8\,\mathrm{R_E}$. The current disruption onset occurs at 11:52:40 UT [*Takahashi et al.*, 1987a; *Lui et al.*, 1992; *Ohtani et al.*, 1995] and it is clear that the low frequency was excited about 1.5 minutes before the onset of current disruption.

Figure 9.

Figure 10.

Figure 11.

The exponential growth phase period of about $30sec$ of the low frequency instability (with amplitude reaching $\delta B/B \geq 0.3$) just before the current disruption onset was previously called "explosive growth phase" [*Ohtani et al.*, 1992] which is accompanied by a large duskward shift of the ion velocity distribution function and hence a significantly enhanced cross-tail current density [*Lui*, 1996]. One possibility of the enhanced duskward ion flux is due to the low frequency instability as proposed in Section 4.4.2 from the resonance between the ion magnetic drift and the low frequency instability. This enhanced cross-tail ion drift population is responsible for exciting higher frequency

instabilities such as CCI which together with the low frequency instability last through out the current disruption phase and form a strong magnetic field turbulence. It is interesting to note that from Plate 1 of *Lui et al.* [1992] the enhanced ion flux in the 30 keV energy bin oscillates between the dawnward and duskward during the current disruption phase.

Figure 12.

During the late growth phase of substorms the equatorial plasma pressure in the midnight sector of the near-Earth plasma sheet observed by the AMPTE/CCE (located at $X \simeq -(8-9)\,\mathrm{R_E}$) [*Lui et al.*, 1992] usually increases $\sim 50\%$ from about 10 minutes prior to the current disruption onset to the time the low frequency instability is excited. Figure 12 shows the three-minute averages of the perpendicular and parallel components of the electron and proton and total plasma pressures, and $\beta = (P_\perp + P_\parallel)/B^2$ for the June 1, 1985 substorm event. The corresponding plasma β increases from ~ 20 at about 10 minutes prior to the current disruption onset to ≥ 60 at 3 minutes prior to the current disruption onset, at which time a low frequency instability was excited. At onset the plasma β drops to about 40 and then drops to ≤ 6 during the current disruption phase. The β decrease during the current disruption phase is mainly due to the increase in the magnetic field intensity as a result of dipolarization with the plasma pressure decreased by about 10%. It is to be noted that the pressure enhancement during the growth phase leads to the enhancement of the cross-tail current density and thinning of the plasma sheet. Although there is no observational determination on the pressure profile during the late growth phase, it is reasonable to expect that the plasma pressure decreases monotonically with increasing radial distance. The energy associated with the current enhancement can be viewed as being stored in the large-scale magnetic field on the nightside during the growth phase. The energy reduction associated with the current disruption and magnetic field dipolarization can be viewed as the energy release during the expansion phase through pressure reduction and pressure profile relaxation as a result of the plasma transport due to the strong turbulence.

4.2. Ideal MHD Theory of Ballooning Instability

To study the instability mechanism for understanding the low frequency modes responsible for substorm onset [*Cheng and Lui*, 1998a], we first study the ballooning instability based on the ideal MHD model. In particular, we perform numerical studies of the ballooning instability for the growth phase magnetospheric equilibrium presented in Section 3.

4.2.1. 3D MHD Eigenmode Equations

We first derive the ideal MHD eigenmode equations without making assumption on the plasma compressibility. We consider quasi-static equilibria with the equilibrium relations $\mathbf{J} \times \mathbf{B} = \boldsymbol{\nabla} P$ and $\boldsymbol{\nabla}(P + B^2/2) = \boldsymbol{\kappa} B^2$, where $\boldsymbol{\kappa} = (\mathbf{B}/B) \cdot \boldsymbol{\nabla}(\mathbf{B}/B)$ is the magnetic field curvature vector. With the time dependence of perturbed quantities as $e^{-i\omega t}$, the linearized ideal MHD equations governing the asymptotic behaviors of the perturbed quantities are the momentum equation

$$\rho\omega^2 \boldsymbol{\xi} = \boldsymbol{\nabla}\delta P + \delta\mathbf{B} \times \mathbf{J} + \mathbf{B} \times \delta\mathbf{J}, \tag{8}$$

the equation of state is chosen as the adiabatic pressure law

$$\delta P + \boldsymbol{\xi} \cdot \boldsymbol{\nabla} P + \Gamma_s P \boldsymbol{\nabla} \cdot \boldsymbol{\xi} = 0, \tag{9}$$

the Ampere's law

$$\boldsymbol{\nabla} \times \delta\mathbf{B} = \delta\mathbf{J}, \tag{10}$$

the Faraday's law

$$-i\omega\delta\mathbf{B} = \boldsymbol{\nabla} \times \delta\mathbf{E}, \tag{11}$$

and the Ohm's law

$$\delta\mathbf{E} = i\omega\boldsymbol{\xi} \times \mathbf{B}, \tag{12}$$

where $\boldsymbol{\xi}$ is the usual fluid displacement vector, $\delta\mathbf{B}$ is the perturbed magnetic field, δP is the perturbed plasma pressure, ρ is the total plasma mass density, $\delta\mathbf{E}$ is the perturbed electric field, and $\Gamma_s = 5/3$ is the ratio of specific heats. We introduce the electrostatic potential ϕ and the vector potential $\mathbf{A}$ such that the perturbed electric field is expressed as $\delta\mathbf{E} = -\boldsymbol{\nabla}\phi + i\omega\mathbf{A}$, and the perturbed magnetic field as $\delta\mathbf{B} = \boldsymbol{\nabla}\times\mathbf{A}$. Because the perturbed parallel electric field vanishes in the ideal MHD model, we have $A_\parallel = \mathbf{A}\cdot\mathbf{B}/B = -\mathbf{B}\cdot\boldsymbol{\nabla}\Phi/B$, where $\Phi = i\phi/\omega$. We also assume that $A_\parallel$ and $\mathbf{A}_\perp$ are of the same order, but $|\boldsymbol{\nabla}_\perp\phi| \gg |\boldsymbol{\nabla}_\parallel\phi|$. Then, $\delta\mathbf{E}_\perp \simeq -\boldsymbol{\nabla}_\perp\phi$ and $\boldsymbol{\xi}\times\mathbf{B} \simeq \boldsymbol{\nabla}_\perp\Phi$.

Operating Eq. (8) with $\mathbf{B}\times$, the perturbed current density perpendicular to $\mathbf{B}$ is given by

$$\delta\mathbf{J}_\perp \simeq \frac{\rho\omega^2}{B^2}\boldsymbol{\nabla}_\perp\Phi + \frac{\mathbf{B}\times\boldsymbol{\nabla}\delta P}{B^2} - \frac{\delta\mathbf{B}\cdot\mathbf{B}}{B^2}\mathbf{J} + \frac{\mathbf{J}\cdot\mathbf{B}}{B^2}\delta\mathbf{B}, \tag{13}$$

Operating Eq. (13) with $\boldsymbol{\nabla}\cdot$ and making use of the equilibrium relations, we have

$$\boldsymbol{\nabla}\cdot\delta\mathbf{J}_\perp \simeq \frac{\rho\omega^2}{B^2}\nabla_\perp^2\Phi - \frac{2\boldsymbol{\kappa}\times\mathbf{B}\cdot\boldsymbol{\nabla}\delta P}{B^2} - \frac{\mathbf{B}\times\boldsymbol{\nabla}P}{B^4}\cdot\boldsymbol{\nabla}(\delta P + \delta\mathbf{B}\cdot\mathbf{B}), \tag{14}$$

where we have neglected the term $\delta\mathbf{B}\cdot\boldsymbol{\nabla}(\mathbf{J}\cdot\mathbf{B}/B^2)$, which is much smaller than the gradient on the perturbed quantities and can be ignored. Next, we choose the Coulomb gauge $\boldsymbol{\nabla}\cdot\mathbf{A} = 0$ and the Ampere's law becomes $\nabla^2\mathbf{A} = -\delta\mathbf{J}$. Again, by ignoring the small gradient on the equilibrium quantities we have $\delta\mathbf{J}\cdot\mathbf{B} \simeq -\nabla^2(\mathbf{A}\cdot\mathbf{B}) = \nabla^2(\mathbf{B}\cdot\boldsymbol{\nabla}\Phi)$. Moreover, we consider the wave frequency to be much smaller than the compressional wave frequency ($\sim k_\perp V_A$, where $V_A = B/\rho^{1/2}$ is the Alfvén speed), so that to the lowest order in $(\omega/k_\perp V_A)$, $\boldsymbol{\nabla}_\perp(\delta P + \delta\mathbf{B}\cdot\mathbf{B}) \simeq 0$ [*Cheng and Johnson*, 1999]. Then, from Eq. (14) and $\boldsymbol{\nabla}\cdot\delta\mathbf{J} = \mathbf{B}\cdot\boldsymbol{\nabla}(\delta\mathbf{J}\cdot\mathbf{B}/B^2) + \boldsymbol{\nabla}\cdot\delta\mathbf{J}_\perp = 0$, we obtain the MHD vorticity equation

$$\mathbf{B}\cdot\boldsymbol{\nabla}\left(\frac{\nabla_\perp^2(\mathbf{B}\cdot\boldsymbol{\nabla}\Phi)}{B^2}\right) + \frac{\rho\omega^2}{B^2}\nabla_\perp^2\Phi - \frac{2\boldsymbol{\kappa}\times\mathbf{B}\cdot\boldsymbol{\nabla}\delta P}{B^2} \simeq 0. \tag{15}$$

From the adiabatic pressure law, Eq. (9), we obtain

$$\delta P - \frac{\mathbf{B}\times\boldsymbol{\nabla}P\cdot\boldsymbol{\nabla}\Phi}{B^2} + \Gamma_s P\boldsymbol{\nabla}\cdot\boldsymbol{\xi} \simeq 0, \tag{16}$$

where we have made use of $\boldsymbol{\xi}\cdot\boldsymbol{\nabla}P = (i\delta\mathbf{E}\times\mathbf{B}/\omega B^2)\cdot\boldsymbol{\nabla}P \simeq -\mathbf{B}\times\boldsymbol{\nabla}P\cdot\boldsymbol{\nabla}\Phi/B^2$. Next, we evaluate

$$\boldsymbol{\nabla}\cdot\boldsymbol{\xi} = \mathbf{B}\cdot\left(\frac{\boldsymbol{\xi}\cdot\mathbf{B}}{B^2}\right) + \boldsymbol{\nabla}\cdot\boldsymbol{\xi}_\perp. \tag{17}$$

By operating the momentum equation, Eq. (8), with $\mathbf{B}\cdot$ we obtain an expression for the parallel displacement

$$\rho\omega^2\boldsymbol{\xi}\cdot\mathbf{B} \simeq \mathbf{B}\cdot\boldsymbol{\nabla}\delta P - \frac{\mathbf{B}\times\boldsymbol{\nabla}P}{B^2}\cdot\boldsymbol{\nabla}\left(\mathbf{B}\cdot\boldsymbol{\nabla}\Phi\right), \tag{18}$$

where we evaluate $\delta\mathbf{B}\cdot\boldsymbol{\nabla}P = \boldsymbol{\nabla}\cdot(\mathbf{A}\times\boldsymbol{\nabla}P) \simeq \boldsymbol{\nabla}\cdot[(\mathbf{A}\cdot\mathbf{B}/B^2)\mathbf{B}\times\boldsymbol{\nabla}P] \simeq -(\mathbf{B}\times\boldsymbol{\nabla}P/B^2)\cdot\boldsymbol{\nabla}(\mathbf{B}\cdot\boldsymbol{\nabla}\Phi)$ with the help of $\mathbf{A}\cdot\mathbf{B} = -\mathbf{B}\cdot\boldsymbol{\nabla}\Phi$ due to the vanishing parallel electric field. Making use of the Ohm's law, we calculate $\boldsymbol{\nabla}\cdot\boldsymbol{\xi}_\perp$ and obtain

$$\boldsymbol{\nabla}\cdot\boldsymbol{\xi}_\perp = -\left(\frac{2\boldsymbol{\kappa}\times\mathbf{B}}{B^2} + \frac{\mathbf{B}\times\boldsymbol{\nabla}P}{B^4}\right)\cdot\boldsymbol{\nabla}_\perp\Phi - \frac{\delta\mathbf{B}\cdot\mathbf{B}}{B^2}. \tag{19}$$

Finally from Eqs. (15)-(19) and $\delta P + \delta\mathbf{B}\cdot\mathbf{B} = 0$, and eliminating δP, we obtain two eigenmode equations for Φ and $\boldsymbol{\nabla}\cdot\boldsymbol{\xi}$ for describing low frequency modes with perpendicular wavelength much shorter than the parallel wavelength:

$$\mathbf{B}\cdot\boldsymbol{\nabla}\left(\frac{\nabla_\perp^2(\mathbf{B}\cdot\boldsymbol{\nabla}\Phi)}{B^2}\right) + \frac{\rho\omega^2}{B^2}\nabla_\perp^2\Phi - \frac{2\boldsymbol{\kappa}\times\mathbf{B}}{B^2}\cdot\boldsymbol{\nabla}\left(\frac{\mathbf{B}\times\boldsymbol{\nabla}P\cdot\boldsymbol{\nabla}\Phi}{B^2}\right) = \frac{2\boldsymbol{\kappa}\times\mathbf{B}\cdot\boldsymbol{\nabla}(\Gamma_s P\boldsymbol{\nabla}\cdot\boldsymbol{\xi})}{B^2}, \tag{20}$$

and

$$\mathbf{B}\cdot\boldsymbol{\nabla}\left[\frac{\Gamma_s P}{\rho\omega^2 B^2}\mathbf{B}\cdot\boldsymbol{\nabla}(\boldsymbol{\nabla}\cdot\boldsymbol{\xi})\right] + \frac{\Gamma_s P + B^2}{B^2}\boldsymbol{\nabla}\cdot\boldsymbol{\xi} - \frac{2\boldsymbol{\kappa}\times\mathbf{B}\cdot\boldsymbol{\nabla}\Phi}{B^2} = 0. \tag{21}$$

It is clear that these two equations describe the coupling between the shear Alfvén type modes, which are mainly determined by Eq. (20), and the slow magnetosonic type modes, which are mainly determined by Eq. (21). The coupling is mainly via the magnetic field curvature and the plasma pressure.

4.2.2. MHD Ballooning Mode Equations

Equations (20) and (21) describe low frequency modes in the three-dimensional space and are usually difficult to solve if not impossible. Thus, further approximations

must be made to simplify these two equations. Fortunately a so-called WKB-ballooning formalism has been developed to simplify these equations by taking advantage of the nature of solutions that the perpendicular wavelength is much shorter than the parallel wavelength [*Dewar and Glasser*, 1983; *Nevins and Pearlstein*, 1988; *Dewar et al.*, 2001]. Adopting the WKB-ballooning formalism, we consider the eikonal representation of the perturbed quantities, $\Phi = ie^{iS}\hat{\Phi}$, where $S \gg 1$ is the WKB eikonal and $\mathbf{B}\cdot\boldsymbol{\nabla}S = 0$. Note that $\boldsymbol{\nabla}S$ is essentially the wave vector perpendicular to $\mathbf{B}$. Thus, the fast variation of Φ in the direction perpendicular to $\mathbf{B}$ is contained in e^{iS} and $\hat{\Phi}$ describes the slow variation along as well as perpendicular to $\mathbf{B}$. Then, to the lowest order in $1/S \ll 1$, the MHD vorticity equation, Eq. (20), reduces to

$$\mathbf{B}\cdot\boldsymbol{\nabla}\left(\frac{|\boldsymbol{\nabla}S|^2\mathbf{B}\cdot\boldsymbol{\nabla}\hat{\Phi}}{B^2}\right) + \frac{\rho\omega^2}{B^2}\nabla_\perp^2\hat{\Phi} + \kappa_c P_s\hat{\Phi} + \kappa_c(\Gamma_s P\Delta) = 0, \tag{22}$$

where $\kappa_c = 2\boldsymbol{\kappa}\times\mathbf{B}\cdot\boldsymbol{\nabla}S/B^2$, $P_s = \boldsymbol{\nabla}P\times\mathbf{B}\cdot\boldsymbol{\nabla}S/B^2$, and $\boldsymbol{\nabla}\cdot\boldsymbol{\xi} = e^{iS}\Delta$. Similarly, Eq. (21) reduces to

$$\mathbf{B}\cdot\boldsymbol{\nabla}\left[\frac{\Gamma_s P}{\rho\omega^2 B^2}\mathbf{B}\cdot\boldsymbol{\nabla}\Delta\right] + \frac{\Gamma_s P + B^2}{B^2}\Delta + \kappa_c\hat{\Phi} = 0. \tag{23}$$

From the ballooning mode equations, Eqs. (22) and (23), we see that the eigenvalues depend on the angle between $\boldsymbol{\nabla}S$ and $\boldsymbol{\nabla}P$. With the Euler potential representation of the ambient magnetic field $\mathbf{B} = \boldsymbol{\nabla}\psi\times\boldsymbol{\nabla}\alpha$, $\boldsymbol{\nabla}S$ can be expressed as $\boldsymbol{\nabla}S = S_\psi\boldsymbol{\nabla}\psi + S_\alpha\boldsymbol{\nabla}\alpha$, where $S_\psi = \partial S/\partial\psi$, and $S_\alpha = \partial S/\partial\alpha$. Then, $\kappa_c = 2S_\alpha[\kappa_s(\boldsymbol{\nabla}\psi\cdot\boldsymbol{\nabla}\alpha/|\boldsymbol{\nabla}\psi|^2 + \Upsilon/\psi) - \kappa_\psi]$, and $P_s = S_\alpha[(\Upsilon/\psi)\partial P/\partial\alpha - \partial P/\partial\psi]$, where $\kappa_\psi = \boldsymbol{\kappa}\cdot\boldsymbol{\nabla}\psi/|\boldsymbol{\nabla}\psi|^2$, $\kappa_s = \boldsymbol{\kappa}\cdot\mathbf{B}\times\boldsymbol{\nabla}\psi/B^2$, and $\Upsilon = \psi S_\psi/S_\alpha$ is a dimensionless free parameter. We see that S_α can be combined with $\hat{\Phi}$, and the eigenmode equations, Eqs. (22) and (23) depend on Υ. Thus, the lowest order eigenvalue, ω^2, is a function of Υ and field lines labeled by ψ and α, with a corresponding wave structure along the field line. Υ has two physical meanings; first, it can be considered as the ratio between the radial wave vector and the azimuthal wave vector, and second, it represents the central location of the mode structure along the field

line. Thus, by scanning the dependence of ω^2 on Υ we determine the radial wave vector and its localization location along the field line for the most unstable mode. The global solutions are then obtained by solving the ballooning ray equations in the next order in $1/S$, which involve the quantization procedure of the rapid wave phase integral

$$I_k = \oint d\mathbf{q} \cdot \boldsymbol{\nabla} S = (2k+1)\pi, \tag{24}$$

where $k = 0, 1, 2, ..$, and $\mathbf{q}$ is the coordinate vector in the (ψ, α) space [*Dewar and Glasser*, 1983; *Nevins and Pearlstein*, 1988; *Dewar et al.*, 2001]. For our purpose, we will address the lowest order ballooning mode equations and find out the lowest order eigenvalue for each field line. From numerical solutions for magnetospheric equilibria with a north-south symmetry, the most unstable solution is obtained with $\Upsilon = 0$ for each field line.

4.2.3. Lagrangian Formulation

To solve the lowest order ballooning mode equations, Eqs. (22) and (23), we construct a variational principle. Multiplying Eq. (22) by $\hat{\Phi}^*$ (the complex conjugate of $\hat{\Phi}$) and integrating along the field line with respect to ds/B, we obtain

$$\int_{s_1}^{s_2} \frac{ds}{B} \left\{ \left(\rho\omega^2 \frac{|\boldsymbol{\nabla} S|^2}{B^2} + \kappa_c P_s \right) |\hat{\Phi}|^2 - \frac{|\boldsymbol{\nabla} S|^2}{B^2} |\mathbf{B} \cdot \boldsymbol{\nabla} \hat{\Phi}|^2 + \Gamma_s P \kappa_c \hat{\Phi}^* \Delta \right\} = 0 \tag{25}$$

where s denotes the distance along the field line so that $\mathbf{B} \cdot \boldsymbol{\nabla} = B(d/ds)$, s_1 and s_2 are the two end points of the field line anchored in the ionosphere, and the boundary condition at the field line end points is assumed to be $\hat{\Phi}^* \mathbf{B} \cdot \boldsymbol{\nabla} \hat{\Phi} = 0$. Multiplying the complex conjugate of Eq. (23) by $\Gamma_s P \Delta$ and integrating along the field line with respect to ds/B, we obtain

$$\int_{s_1}^{s_2} \frac{ds}{B} \left\{ \frac{\Gamma_s P \left(\Gamma_s P + B^2 \right)}{B^2} |\Delta|^2 - \rho\omega^2 B^2 |Z|^2 + \Gamma_s P \kappa_c \hat{\Phi}^* \Delta \right\} = 0 \tag{26}$$

where $Z = \Gamma_s P (\mathbf{B} \cdot \boldsymbol{\nabla} \Delta) / \rho\omega^2 B^2$, and the boundary condition $\Delta Z^* = 0$ at the field line end points is assumed. Subtracting Eq. (26) from Eq. (25) we obtain a Lagrangian

functional δL given by

$$\delta L = \int_{s_1}^{s_2} \frac{ds}{B} \left\{ \rho\omega^2 \left(\frac{|\boldsymbol{\nabla} S|^2}{B^2} |\hat{\Phi}|^2 + B^2 |Z|^2 \right) - \left[\frac{|\boldsymbol{\nabla}\psi|^2}{B^2} |\mathbf{B}\cdot\boldsymbol{\nabla}\hat{\Phi}|^2 - \kappa_c P_s |\hat{\Phi}|^2 + \frac{\Gamma_s P B^2}{\Gamma_s P + B^2} |\kappa_c \hat{\Phi} + \mathbf{B}\cdot\boldsymbol{\nabla} Z|^2 \right] \right\} = 0 \qquad (27)$$

where we have also made use of Eq. (23) to substitute Δ in terms of $\hat{\Phi}$ and $\mathbf{B}\cdot\boldsymbol{\nabla} Z$. It is straightforward to verify that Eqs. (22) and (23) are a consequence of the requirement that the functional δL is stationary. Since $\delta L = 0$, it is clear that the eigenvalues ω^2 and the corresponding eigenfunctions $\hat{\Phi}$ and Δ must be real. The determination of the stability of ballooning modes reduces to that of finding the eigenvalues ω^2 and eigenfunctions so that the Lagrangian functional δL is stationary with respect to variations of $\hat{\Phi}$ and Δ. The admissible variational functions must be square-integrable and satisfy the boundary conditions at the field line end points. It should be noted from Eq. (27) that there is a possibility of $\omega^2 < 0$ if $\kappa_c P_s > 0$, and if $\omega^2 < 0$ the plasma is unstable at these field lines. From the definition of κ_c and P_s (given after Eq. (22)) we see that if the pressure gradient is in the same direction as the magnetic field curvature, then $\kappa_c P_s > 0$ and the ballooning mode is possible to be unstable.

Figure 13.

Figure 14.

4.3. Numerical Solutions of MHD Ballooning Mode Equations

Once a 3D quasi-static magnetospheric equilibrium is known we can compute the ballooning mode solutions for each field line. However, to obtain the mode frequency or growth rate in physical unit we need to specify the mass density along field lines. We assume for simplicity the plasma density to be constant along the field line and choose it to be a function of radius in the equatorial plane: $\rho(R) = 10\,(R_{geos}/R)^3 m_p/cm^3$, where $R_{geos} = 6.6\,R_E$ is the geosynchronous orbit distance and m_p is the proton mass. When the actual mass density distribution is known, the frequency or growth rate can be recalculated easily with the actual density from the results given in this paper.

Employing the growth phase magnetospheric equilibrium published previously

[*Zaharia and Cheng*, 2003] and choosing $(S_\psi/S_\alpha) = 0$, the numerical solutions of the eigenvalues ω^2 and the eigenfunctions for the Lagrangian equation, Eq. (27) for each field line have been obtained by employing a finite element method with the boundary conditions that both $\hat{\Phi}$ and Δ vanish at the end points of the field line in the ionosphere. For the full ideal MHD model, Figures 13 and 14 show the color plot in the equatorial plane and the contours in the northern polar ionosphere of the eigenvalue f^2 (in $(mHz)^2$) of the fundamental harmonic ballooning modes, respectively [*Cheng and Zaharia*, 2003b]. Also shown in Fig. 13 is the contours of the azimuthal current density (in $\mathrm{nA/m^2}$) and in Fig. 14 is the color plot of the field-aligned current density. Note that all field lines beyond $x \simeq -6\,\mathrm{R_E}$ down the tail in the night side are unstable. The region of the most unstable modes tracks well with the strong cross-tail current sheet region, consistent with the expectation from substorm onset observations. The peak growth rate region is located in the strong cross-tail current region (at about $X \simeq -9\,\mathrm{R_E}$), which is at the tailward side of the peak cross-tail current density location at $X \simeq -8\,\mathrm{R_E}$. In the polar ionosphere the field lines in the peak ballooning instability growth rate region map to the transition region between the region-1 and region-2 currents. The results clearly indicate that, although the ideal MHD model over estimates the instability growth rate due to the lack of particle kinetic effects, it shows the field lines where the ballooning free energy is largest and the most unstable ballooning mode is located. Moreover, we expect that the global structure of the MHD ballooning instability is localized around the maximum growth rate location in the equatorial plane with an half-width extending to the location with growth rate equal to about one half of the maximum growth rate.

Figure 15.

Next, we compute the stability of the ballooning modes for the same growth phase magnetospheric equilibrium with the Lee-Wolf model [*Lee and Wolf*, 1992] and the fast-MHD model [*Horton et al.*, 1999], which made approximations on the plasma compressibility, and compare these solutions with the solution of the full MHD model shown in Figs. 13 and 14. This will resolve the controversy arising from these

approximations [*Lee*, 1999a]. In the Lee-Wolf model, the plasma compressibility is assumed to be a non-vanishing constant along the field line. With $\mathbf{B}\cdot\boldsymbol{\nabla}\Delta = 0$, Δ can be obtained from Eq. (23) and is given by $\langle(\Gamma_s P + B^2)/B^2\rangle\Delta + \langle\kappa_c\hat{\Phi}\rangle = 0$, where $\langle X\rangle = \int_{s_1}^{s_2} dsX/B$. Then, Eq. (22) reduces to

$$\mathbf{B}\cdot\boldsymbol{\nabla}\left(\frac{|\boldsymbol{\nabla}S|^2\mathbf{B}\cdot\boldsymbol{\nabla}\hat{\Phi}}{B^2}\right) + \frac{\rho\omega^2}{B^2}\nabla_\perp^2\hat{\Phi} + \kappa_c P_s\hat{\Phi} - \frac{\kappa_c\Gamma_s P\langle\kappa_c\hat{\Phi}\rangle}{\langle\frac{\Gamma_s P+B^2}{B^2}\rangle} = 0, \tag{28}$$

and a Lagrangian functional δL can be constructed and is given by

$$\delta L = \int_{s_1}^{s_2}\frac{ds}{B}\left\{\rho\omega^2\left(\frac{|\boldsymbol{\nabla}S|^2}{B^2}|\hat{\Phi}|^2\right) + \kappa_c P_s|\hat{\Phi}|^2 - \left[\frac{|\boldsymbol{\nabla}S|^2}{B^2}|\mathbf{B}\cdot\boldsymbol{\nabla}\hat{\Phi}|^2 + \frac{\Gamma_s P\kappa_c\hat{\Phi}\langle\kappa_c\hat{\Phi}\rangle}{\langle\frac{\Gamma_s P+B^2}{B^2}\rangle}\right]\right\} = 0 \tag{29}$$

The solution of Eq. (29) is shown in Fig. 15, which shows that ballooning modes are unstable near the current sheet region between $X = -8$ and $-10\,\mathrm{R_E}$ and weakly unstable farthest near the tail boundary, but are stable in other region. This result is different from the full MHD solution shown in Figure 13. Thus, the Lee-Wolf model produce too much stabilization due to the approximation of constant plasma compressibility. **Figure 16.**

In the fast-MHD model [*Horton et al.*, 1999], the parallel displacement is assumed to vanish, $\boldsymbol{\xi}\cdot\mathbf{B} = 0$. From the adiabatic pressure law and the parallel component of the momentum equation, we obtain $\Delta + [\kappa_c B^2/(\Gamma_s P + B^2)]\hat{\Phi} = 0$. Then, Eq. (22) reduces to

$$\mathbf{B}\cdot\boldsymbol{\nabla}\left(\frac{|\boldsymbol{\nabla}S|^2\mathbf{B}\cdot\boldsymbol{\nabla}\hat{\Phi}}{B^2}\right) + \frac{\rho\omega^2}{B^2}\nabla_\perp^2\hat{\Phi} + \kappa_c P_s\hat{\Phi} - \frac{\Gamma_s P\kappa_c^2 B^2}{\Gamma_s P + B^2}\hat{\Phi} = 0, \tag{30}$$

and a Lagrangian functional δL can be constructed and is given by

$$\delta L = \int_{s_1}^{s_2}\frac{ds}{B}\left\{\rho\omega^2\left(\frac{|\boldsymbol{\nabla}S|^2}{B^2}|\hat{\Phi}|^2\right) + \kappa_c P_s|\hat{\Phi}|^2 - \left[\frac{|\boldsymbol{\nabla}S|^2}{B^2}|\mathbf{B}\cdot\boldsymbol{\nabla}\hat{\Phi}|^2 + \frac{\Gamma_s P\kappa_c^2 B^2}{\Gamma_s P + B^2}|\hat{\Phi}|^2\right]\right\} = 0 \tag{31}$$

The solution of Eq. (31) is shown in Fig. 16. which clearly shows that for most of the field lines (except near the far tail boundary of the equilibrium) the ballooning modes are stable. This result is completely different from the results of full MHD model shown in Figures 13 and those of the Lee-Wolf model shown in Fig. 15. Thus, the fast-MHD model gives a much worse approximation of the plasma compressibility than the Lee-Wolf model.

In summary, based on the ideal MHD model the ballooning modes are expected to be unstable for the growth phase magnetospheric equilibrium in a large region of the plasma sheet where $\beta_{eq} \geq 1$. The numerical results clearly illustrate that to obtain the correct stability result even within the ideal MHD model it is essential to model the plasma compressibility correctly as well as the equilibrium fields realistically. Moreover, even for quiet time equilibria [*Zaharia et al.*, 2003], the full MHD calculations (not shown in the paper) indicate that the ballooning modes are unstable for the entire plasma sheet region when $\beta_{eq} \geq 1$. Thus, the results of the ballooning mode stability calculations based on the ideal MHD model are not consistent with the AMPTE/CCE observations that during most of the growth phase $\beta_{eq} < 50$ and the magnetic fields are quiet without noticeable fluctuations [*Lui et al.*, 1992], and the low frequency instability was observed in the enhanced cross-tail current sheet region only toward the end of the growth phase when $\beta_{eq} > 50$ [*Cheng and Lui*, 1998a]. However, even with the inconsistency with observations, the ideal MHD model provides the valuable information that the most unstable ballooning instability and the maximum free energy associated with the product of the plasma pressure gradient and magnetic field curvature are located in the strong cross-tail current sheet region when realistic 3D magnetospheric equilibria are considered.

4.4. Kinetic Theory of Ballooning Instability

To mitigate the difficulty arising from the ideal MHD model, we need to consider the particle kinetic effects. We shall derive the kinetic eigenmode equations for the ballooning

modes by employing the gyrokinetic equations, which are most suitable for studying low frequency waves and instabilities with $\omega < \omega_{ci}$. We will show that the kinetic effects of ion gyroradii and trapped electron dynamics can greatly increase the stabilizing effects of field line tension and thus enhance the critical β_{eq} to excite the ballooning instability [*Cheng and Lui*, 1998a]. The consequence is to reduce the equatorial region of the unstable ballooning modes to the strong cross-tail current sheet region where the free energy associated with the plasma pressure gradient and magnetic field curvature is maximum.

In a 3D magnetospheric equilibrium with the magnetic field expressed as $\mathbf{B} = \boldsymbol{\nabla}\psi \times \boldsymbol{\nabla}\alpha$, we consider plasmas with an isotropic pressure and the particle guiding center distribution is $F = F(\mathcal{E}, \psi, \alpha)$ so that the equilibrium pressure is a function of ψ and α and is constant along $\mathbf{B}$. We consider perturbations with $k_\perp > k_\parallel$, $k_\perp L_\perp > 1$, and $k_\parallel L_\parallel > 1$, where $k_\parallel$ and $k_\perp$ are the wave number parallel and perpendicular to the ambient magnetic field $\mathbf{B}$, and $L_\parallel$ and $L_\perp$ are the background equilibrium scale length parallel and perpendicular to the ambient magnetic field $\mathbf{B}$, respectively. We adopt the WKB-Ballooning representation (presented in Section 4.2.2) of the perturbed quantities which are proportional to $e^{i(S-\omega t)}$, where $\mathbf{B} \cdot \boldsymbol{\nabla} S = 0$. Note that $\boldsymbol{\nabla} S$ is essentially the wave vector perpendicular to $\mathbf{B}$, $\mathbf{k}_\perp$. We shall employ the linearized gyrokinetic equations which describe the dynamics of low frequency instabilities with frequencies much smaller than the particle cyclotron frequency [*Antonsen, Jr. and Lane*, 1980; *Catto et al.*, 1981]. The gyrokinetic equations properly include kinetic effects such as full particle Larmor radii, wave-particle resonances, particle drifts motions, etc. In terms of the rationalized MKS unit, the perturbed particle distribution function can be expressed as

$$\delta f = \frac{q}{M}\frac{\partial F}{\partial \mathcal{E}}\left[1 - \left(1 - \frac{\omega_\star^T}{\omega}\right) J_0 e^{iL}\right]\Phi + g e^{iL}, \tag{32}$$

where F is the particle equilibrium distribution function, q is the particle charge, M is the particle mass, $\mathcal{E} = v^2/2$ the particle energy per unit mass, the subscripts $\parallel$ and $\perp$ represent parallel and perpendicular components to the equilibrium magnetic field, $\omega_\star^T =$

$\mathbf{B}\times\boldsymbol{\nabla}S\cdot\boldsymbol{\nabla}F/(B\omega_c\partial F/\partial\mathcal{E})$, $\omega_c = qB/M$ is the cyclotron frequency, J_l is the l-th order Bessel function of the argument $|\boldsymbol{\nabla}S|v_\perp/\omega_c$, $L = \mathbf{B}\times\boldsymbol{\nabla}S\cdot\mathbf{v}_\perp/\omega_c = (|\boldsymbol{\nabla}S|v_\perp/\omega_c)\sin\varphi$, φ is the particle gyro-phase angle between $\boldsymbol{\nabla}S$ and the particle perpendicular velocity $\mathbf{v}_\perp$, Φ is the electrostatic potential, and g is the nonadiabatic part of the perturbed particle distribution function. Next, we define the parallel electric field potential with $\delta\mathbf{E}_\parallel = -\boldsymbol{\nabla}_\parallel\Psi$, then the vector potential, defined by $\mathbf{A} = \mathbf{A}_\parallel + \mathbf{A}_\perp = \mathbf{A}_\parallel - i\tilde{A}_\perp\mathbf{B}\times\boldsymbol{\nabla}S/(B|\boldsymbol{\nabla}S|)$, is related to Ψ, the electrostatic potential Φ, and the parallel perturbed magnetic field $\delta B_\parallel$ by $i\omega\mathbf{A}_\parallel = \boldsymbol{\nabla}_\parallel(\Phi-\Psi)$ and $\delta B_\parallel = |\boldsymbol{\nabla}S|\tilde{A}_\perp$. Based on the WKB-ballooning formalism the lowest order (in $1/S \ll 1$) gyrokinetic equation for g in the low frequency ($\omega \ll \omega_c$) limit is given by

$$(\omega - \omega_d + i\mathbf{v}_\parallel\cdot\boldsymbol{\nabla}_\parallel + i\nu)g = -\frac{q}{M}\frac{\partial F}{\partial\mathcal{E}}\left(1-\frac{\omega_\star^T}{\omega}\right)\left[J_0\left(\omega_d\Phi - i\mathbf{v}_\parallel\cdot\boldsymbol{\nabla}_\parallel\Psi\right) + \frac{\omega v_\perp}{|\boldsymbol{\nabla}S|}J_1\delta B_\parallel\right], \tag{33}$$

where $\omega_d = -(\mathbf{B}\times\boldsymbol{\nabla}S/B\omega_c)\cdot(v_\parallel^2\boldsymbol{\kappa} + \mu\boldsymbol{\nabla}B)$ is the magnetic drift frequency, $\boldsymbol{\kappa}$ is the magnetic field curvature, $\mu = v_\perp^2/2B$ is the particle magnetic moment, and ν is the particle collision frequency operator. Note that the dissipative effects such as wave-particle resonance and particle collision are included in g. Also, the gyrokinetic formulation is still valid for the case that the particle gyroradius is on the same order as the background magnetic field scale length if the magnetic drift frequency is replaced with the pitch angle average value to account for the non-conservation of the magnetic moment [*Hurricane et al.*, 1994].

4.4.1. Kinetic Eigenmode Equations

To derive the kinetic eigenmode equations we follow the procedure described in *Cheng* [1982a]; *Cheng et al.* [1995]. To determine the parallel electric field we use the quasineutrality condition, $\sum_j q_j\delta n_j = \sum_j\int d^3v q_j\delta f_j = 0$, where the summation over j is

over all particle species. Using Eq. (32) we have

$$\delta n_j = \frac{\mathbf{B}\times\boldsymbol{\nabla}S\cdot\boldsymbol{\nabla}N_j}{\omega B^2}\Phi + \int d^3v \left[\frac{q_j}{M_j}\frac{\partial F_j}{\partial \mathcal{E}}\left(1-\frac{\omega_{\star j}^T}{\omega}\right)(1-J_0^2)\Phi + g_j J_0\right], \tag{34}$$

where N is the background particle density. Then, the charge quasi-neutrality condition becomes

$$\sum_j \int d^3v \frac{q_j^2}{M_j}\frac{\partial F_j}{\partial \mathcal{E}}\left(1-\frac{\omega_{\star j}^T}{\omega}\right)(1-J_0^2)\Phi + \sum_j \int d^3v q_j g_j J_0 = 0, \tag{35}$$

where $\sum_j q_j N_j = 0$ due to charge neutrality.

In the WKB-ballooning formalism the Ampère's law can be written as $\delta\mathbf{J}_\perp = -\boldsymbol{\nabla}^2\mathbf{A}_\perp \simeq |\boldsymbol{\nabla}S|^2\mathbf{A}_\perp = -i\delta B_\parallel \mathbf{B}\times\boldsymbol{\nabla}S/B$. Thus, using Eq. (32) we have

$$\begin{aligned}\mathbf{B}\cdot\delta\mathbf{B} &= i\sum_j \int d^3v q_j \frac{\mathbf{B}\times\boldsymbol{\nabla}S\cdot\mathbf{v}_\perp}{|\boldsymbol{\nabla}S|^2}\delta f_j \\ &= \sum_j \int d^3v M_j v_\perp^2 \frac{\omega_{cj}J_1}{|\boldsymbol{\nabla}S|v_\perp}\left[\frac{q_j}{M_j}\frac{\partial F_j}{\partial\mathcal{E}}\left(1-\frac{\omega_{\star j}^T}{\omega}\right)J_0\Phi - g_j\right],\end{aligned} \tag{36}$$

where we have made use of the gyro-phase average quantity $(i/2\pi)\int d\varphi \sin\varphi e^{iL} = J_1(|\boldsymbol{\nabla}S|v_\perp/\omega_c)$. Eq. (37) can be rewritten in a MHD-like form as

$$\mathbf{B}\cdot\delta\mathbf{B} = \frac{\mathbf{B}\times\boldsymbol{\nabla}P\cdot\boldsymbol{\nabla}S}{\omega B^2}\Phi - \sum_j \delta\hat{P}_{\perp j}, \tag{37}$$

where $P = \sum_j P_j$ is the total plasma pressure, and

$$\delta\hat{P}_{\perp j} = \int d^3v \frac{M_j v_\perp^2}{2}\left[\frac{q_j}{M_j}\frac{\partial F_j}{\partial\mathcal{E}}\left(1-\frac{\omega_{\star j}^T}{\omega}\right)\left(1-\frac{2\omega_{cj}J_1J_0}{|\boldsymbol{\nabla}S|v_\perp}\right)\Phi + \frac{2\omega_{cj}J_1}{|\boldsymbol{\nabla}S|v_\perp}g_j\right] \tag{38}$$

contains the plasma compressibility and all the non-MHD effects such as finite ion gyroradii and wave-particle resonances, and non-adiabatic particle response.

To derive the kinetic vorticity equation that governs the electrostatic potential, we multiply Eq. (33) with $\omega q_j J_0$, integrate it over the velocity space, sum it over all particle species, and make use of the equality

$$\int dv^3 J_0 \mathbf{v}_\parallel\cdot\boldsymbol{\nabla}g = \mathbf{B}\cdot\boldsymbol{\nabla}\left(\int dv^3 \frac{v_\parallel g J_0}{B}\right), \tag{39}$$

where $\int dv^3 = \sum_\sigma 2\pi B \int_0^\infty d\mathcal{E} \int_0^{\mathcal{E}/B} d\mu/|v_\parallel|$, $\sigma = \pm 1$ indicates the direction of the particle parallel velocity, and use has been made of the fact that $\mathcal{E}$ and μ are constant along the unperturbed particle guiding center orbit. Then, the kinetic vorticity equation becomes

$$\sum_j \int d^3v \omega \left(\omega - \omega_{dj} + i\nu_j\right) q_j J_0 g_j + i\mathbf{B}\cdot\boldsymbol{\nabla}\left(\frac{\omega\delta J_\parallel}{B}\right)$$
$$+\omega \sum_j \int d^3v \frac{q_j^2}{M_j}\frac{\partial F_j}{\partial \mathcal{E}}\left(1 - \frac{\omega_{\star j}^T}{\omega}\right)\left(\omega_{dj} J_0^2 \Phi + \frac{\omega v_\perp}{|\boldsymbol{\nabla} S|} J_0 J_1 \delta B_\parallel\right) = 0. \quad (40)$$

Making use of Eq. (35) and the parallel component of the Ampere's law, $\delta J_\parallel = -\boldsymbol{\nabla}^2 A_\parallel \simeq |\boldsymbol{\nabla} S|^2 A_\parallel = -i(|\boldsymbol{\nabla} S|^2/B\omega)\mathbf{B}\cdot\boldsymbol{\nabla}(\Phi - \Psi)$, Eq. (40) becomes

$$\mathbf{B}\cdot\boldsymbol{\nabla}\left[\frac{|\boldsymbol{\nabla} S|^2}{B^2}\mathbf{B}\cdot\boldsymbol{\nabla}\left(\Phi - \Psi\right)\right] - \omega^2 \sum_j \int d^3v \frac{q_j^2}{M_j}\frac{\partial F_j}{\partial \mathcal{E}}\left(1 - \frac{\omega_{\star j}^T}{\omega}\right)\left(1 - J_0^2\right)\Phi$$
$$-\omega \sum_j \int d^3v q_j(\omega_{dj} - i\nu_j) J_0 g_j + \omega \sum_j \int d^3v \frac{q_j^2}{M_j}\frac{\partial F_j}{\partial \mathcal{E}}\left(1 - \frac{\omega_{\star j}^T}{\omega}\right)\left(\frac{\omega v_\perp^2}{2\omega_{cj}}\delta B_\parallel + \omega_{dj}\Phi\right)$$
$$-\omega \sum_j \int d^3v \frac{q_j^2}{M_j}\frac{\partial F_j}{\partial \mathcal{E}}\left(1 - \frac{\omega_{\star j}^T}{\omega}\right)\left[\frac{\omega v_\perp^2}{2\omega_{cj}}\left(1 - \frac{2\omega_{cj}}{|\boldsymbol{\nabla} S| v_\perp} J_0 J_1\right)\delta B_\parallel + \omega_{dj}\left(1 - J_0^2\right)\Phi\right]$$
$$= 0, \quad (41)$$

Note that, if $k_\perp \rho_i < 1$, the fifth term is smaller than the fourth term by $k_\perp^2 \rho_i^2$ in the above equation. The velocity space integration can be carried out for the fourth term and with the help of Eq. (37) and the equilibrium relation, $\boldsymbol{\nabla}_\perp(P_\perp + B^2/2) = B^2\boldsymbol{\kappa}$, we have

$$\sum_j \int d^3v \frac{q_j^2}{M_j}\frac{\partial F_j}{\partial \mathcal{E}}\left(1 - \frac{\omega_{\star j}^T}{\omega}\right)\left(\frac{\omega v_\perp^2}{2\omega_{cj}}\delta B_\parallel + \omega_{dj}\Phi\right)$$
$$= \frac{\mathbf{B}\times\boldsymbol{\nabla} S\cdot\boldsymbol{\nabla} P}{B^4}\left[-\mathbf{B}\cdot\delta\mathbf{B} + \frac{\mathbf{B}\times\boldsymbol{\nabla} S}{\omega}\cdot\left(\boldsymbol{\kappa} + \frac{\boldsymbol{\nabla} B}{B}\right)\Phi\right]$$
$$= \frac{\mathbf{B}\times\boldsymbol{\nabla} S\cdot\boldsymbol{\nabla} P}{B^4}\left[2\frac{\mathbf{B}\times\boldsymbol{\nabla} S\cdot\boldsymbol{\kappa}}{\omega}\Phi + \sum_j \delta\hat{P}_{\perp j}\right] \quad (42)$$

Then, the kinetic vorticity equation has the following MHD-like form

$$\mathbf{B}\cdot\boldsymbol{\nabla}\left[\frac{|\boldsymbol{\nabla} S|^2}{B^2}\mathbf{B}\cdot\boldsymbol{\nabla}\left(\Phi - \Psi\right)\right] - \omega^2 \sum_j \int d^3v \frac{q_j^2}{M_j}\frac{\partial F_j}{\partial \mathcal{E}}\left(1 - \frac{\omega_{\star j}^T}{\omega}\right)\left(1 - J_0^2\right)\Phi$$

$$+2\left(\frac{\mathbf{B}\times\boldsymbol{\nabla}S\cdot\boldsymbol{\kappa}}{B^2}\right)\left(\frac{\mathbf{B}\times\boldsymbol{\nabla}S\cdot\boldsymbol{\nabla}P}{B^2}\right)\Phi$$

$$+\omega\left(\frac{\mathbf{B}\times\boldsymbol{\nabla}S\cdot\boldsymbol{\nabla}P}{B^4}\right)\sum_j\delta\hat{P}_{\perp j}-\omega\sum_j\int d^3v q_j(\omega_{dj}-i\nu_j)J_0 g_j$$

$$-\omega\sum_j\int d^3v\frac{q_j^2}{M_j}\frac{\partial F_j}{\partial\mathcal{E}}\left(1-\frac{\omega_{\star j}^T}{\omega}\right)\left[\frac{\omega v_\perp^2}{2\omega_{cj}}\left(1-\frac{2\omega_{cj}}{|\boldsymbol{\nabla}S|v_\perp}J_0J_1\right)\delta B_\parallel+\omega_{dj}\left(1-J_0^2\right)\Phi\right]=0, \quad (43)$$

If we take the small ion gyroradius limit and neglect the parallel electric field, the first three terms of Eq. (43) are equivalent to the first three terms in the MHD vorticity equation given by Eq. (eq:PhiB). The last three terms of Eq. (43) contain the plasma compressibility and all the non-MHD effects such as finite ion gyroradii and wave-particle resonances, and non-adiabatic particle response. Equations (35), (37), and (43) constitute the basic kinetic eigenmode equations for studying kinetic ballooning instability. To complete the formulation of the eigenmode equations one needs to determine the nonadiabatic perturbed particle distribution by solving Eq. (33), which was derived previously in *Cheng and Qian* [1994]. In general, exact solutions of Eq. (33) can not be obtained analytically, but can be expressed as an infinite series. Each term in the series must be computed numerically for each magnetic field geometry. However, to achieve analytical understanding of the kinetic effects on the stability of ballooning modes, we need to consider simplified solutions of the gyrokinetic equation and making simplifying assumptions.

4.4.2. Kinetic Ballooning Instability

Based on the AMPTE/CCE observation of particle data [*Lui et al.*, 1992; *Lui*, 1996], toward the end of the growth phase when a low frequency instability was observed, we found that the average electron energy is about 5 keV and the average ion energy is about 10 keV. The particle velocity distribution function does not have appreciable bulk drift and the plasma pressure becomes isotropic in the late growth phase in a few minutes before the onset. The average ion magnetic drift velocity evaluated at

the average ion energy is about the same as the ion thermal velocity if the $\boldsymbol{\nabla} B$ scale length is on the order of average ion Larmor radius. With these information we proceed to obtain an analytical understanding of the kinetic ballooning instability (KBI) with the orderings: $k_\perp \rho_i \sim O(1)$, $k_\parallel \ll k_\perp$ and $v_e > (\omega/k_\parallel) > v_i$ [*Cheng*, 1982b, 1982a], where $k_\perp = |\boldsymbol{\nabla} S|$ is the perpendicular wave number, ρ_i is the ion gyroradius, $k_\parallel$ is the parallel wave number, and v_e and v_i are the electron and ion thermal speed, respectively. With these orderings the following kinetic effects must be considered: trapped electron dynamics, ion Larmor radius effect and wave-particle resonance with $\omega - \omega_{di} = 0$. We shall consider collisionless plasmas ($\nu_{e,i} = 0$) and obtain approximate solutions of the perturbed particle distributions based on the gyrokinetic formulation by assuming that both electrons and ions have local Maxwellian equilibrium distribution functions [*Cheng et al.*, 1995]. For ions we consider only the contribution from protons.

For electrons we shall neglect Larmor radius effects and consider $|v_\parallel \nabla_\parallel| \gg \omega, \omega_{de}$. Clearly, trapped and un-trapped electrons have very different parallel dynamics. The un-trapped electron dynamics along $\mathbf{B}$ is mainly determined by its fast parallel transit motion, and its motion perpendicular to the field line is mainly determined by the $\mathbf{E} \times \mathbf{B}$ drift motion. Thus, to the lowest order in $(\omega/|v_\parallel \nabla_\parallel|)$ the non-adiabatic electron distribution can solved from Eq. (33) [*Cheng*, 1982a] and is given by

$$g_{eu} \simeq -\frac{e}{M_e} \frac{\partial F_e}{\partial \mathcal{E}} \left(1 - \frac{\omega_{\star e}^T}{\omega}\right) \Psi, \tag{44}$$

where $q_e = -e$, e is the absolute value of the electron charge, and F_e is the electron Maxwellian distribution. Then, the perturbed un-trapped electron density and is given by

$$\delta n_{eu} \simeq \frac{e N_{eu}}{T_e} \left[\frac{\omega_{*e}}{\omega} \Phi + \left(1 - \frac{\omega_{*e}}{\omega}\right) \Psi\right], \tag{45}$$

where N_{eu} is the untrapped electron density, $\omega_{*e} = \mathbf{B} \times \boldsymbol{\nabla} N_e \cdot \mathbf{k}_\perp T_e/(B m_e \omega_{ce} N_e)$ is the electron diamagnetic drift frequency, N_e and T_e are the electron density and temperature,

respectively. Note that $N_{eu}/N_e = 1 - [1 - B(s)/B_i]^{1/2}$ is the fraction of un-trapped electron at the field line location s, B_i is the magnetic field at the ionosphere. Near the equator $N_{eu}/N_e \simeq B(s)/2B_i \ll 1$.

The trapped electron dynamics along the field line is mainly determined by its fast parallel bounce motion, and its motion perpendicular to the field line is mainly determined by the $\mathbf{E}\times\mathbf{B}$ and magnetic drift motions. To the lowest order in (ω/ω_{be}), where ω_{be} is the electron bounce frequency, the nonadiabatic trapped electron distribution function is given by

$$g_{et} \simeq -\frac{e}{M_e}\frac{\partial F_e}{\partial \mathcal{E}}\left(1-\frac{\omega^T_{\star e}}{\omega}\right)\left[\Psi - \frac{\langle(\omega-\omega_{de})\Psi + \omega_{de}\Phi + \omega v_\perp^2 \delta B_\parallel/2\omega_{ce}\rangle}{\langle\omega-\omega_{de}\rangle}\right] \tag{46}$$

Thus, the perturbed trapped electron density is given by

$$\delta n_{et} \simeq \frac{eN_{et}}{T_e}\left[\frac{\omega_{*e}}{\omega}\Phi + \left(1-\frac{\omega_{*e}}{\omega}\right)\Delta\Psi\right] + \delta\hat{n}_{et}, \tag{47}$$

where $N_{et}/N_e = [1 - B(s)/B_i]^{1/2}$ is the fraction of trapped electron,

$$\Delta = \int_{tr} d^3v (F_e/N_{et})\left[1 - \frac{\langle(\omega-\omega_{de})\Psi\rangle}{\langle\omega-\omega_{de}\rangle\Psi}\right], \tag{48}$$

$$\delta\hat{n}_{et} = -\int_{tr} d^3v \frac{eF_e}{T_e}\frac{(\omega-\omega^T_{\star e})}{(\omega-\langle\omega_{de}\rangle)}\left\langle\frac{\omega_{de}}{\omega}\Phi + \frac{v_\perp^2}{2\omega_{ce}}\delta B_\parallel\right\rangle, \tag{49}$$

and $\langle\omega_{de}\rangle$ is the trapped particle orbit average of ω_{de}. Note that $\Delta \ll 1$ near the equator.

To obtain the perturbed non-adiabatic ion distribution function we assume that $\omega, \omega_{di} \gg |v_\parallel \nabla_\parallel|$, and obtain

$$g_i \simeq \frac{eF_i}{T_i}\frac{\omega-\omega^T_{\star i}}{\omega-\omega_{di}}\left(\frac{\omega_{di}J_0\Phi}{\omega} + \frac{v_\perp J_1 \delta B_\parallel}{k_\perp}\right). \tag{50}$$

Note that the ion dynamics is mainly determined by its perpendicular motion, which is due to $\mathbf{E}\times\mathbf{B}$, polarization and magnetic drift motions and is substantially different from the electron perpendicular motion if $k_\perp\rho_i \sim 1$. The perturbed ion density is given by

$$\delta n_i \simeq -\frac{eN_i}{T_i}\left[\frac{\omega_{*i}}{\omega}\Phi + \left(1-\frac{\omega_{*pi}}{\omega}\right)(1-\Gamma_0)\,\Phi\right] + \delta\hat{n}_i, \tag{51}$$

where N_i is the ion density, T_i is the ion temperature, $\omega_{*i} = \mathbf{B} \times \boldsymbol{\nabla} N_i \cdot \mathbf{k}_\perp T_i/(B m_i \omega_{ci} N_i)$, $\omega_{*pi} = \mathbf{B} \times \boldsymbol{\nabla} P_i \cdot \mathbf{k}_\perp T_i/(B m_i \omega_{ci} P_i)$, $\Gamma_0(b_i) = I_0(b_i)\exp(-b_i)$, $b_i = k_\perp^2 T_i/M_i\omega_{ci}^2 = k_\perp^2 \rho_i^2/2$, I_0 is the modified Bessel function of the zeroth order, and $\delta\hat{n}_i = \int d^3v g_i J_0$.

From the charge quasi-neutrality condition we obtain the parallel electric field potential

$$\left(\frac{N_{eu} + N_{et}\Delta}{N_e}\right)\Psi = -\frac{T_e}{T_i}\frac{\omega - \omega_{*pi}}{\omega - \omega_{*e}}\left(1 - \Gamma_0\right)\Phi + \frac{T_e}{eN_e}\left(\delta\hat{n}_i - \delta\hat{n}_e\right) \tag{52}$$

If we ignore the second term on the right hand side of the above equation, the physical origin of the parallel electric field is clearly due to the difference between the ion and electron gyroradii given in the first term on the right hand side of the equation, which is large if $b_i \sim O(1)$. If $N_{et}\Delta \ll N_{eu}$, the term on the left hand side of the equation represent the ratio between the untrapped electron density to the total electron density. In comparison with the limit without trapped electrons, the parallel electric field is enhanced by $N_e/(N_{eu} + N_{et}\Delta)$ which is much larger than unity near the equator.

The physical picture of the enhanced perturbed parallel electric field ($\delta E_\parallel = -\boldsymbol{\nabla}_\parallel \Psi$) can be understood by considering the particle dynamics. Upon a three-dimensional perturbation the electrons and ions move differently in the direction perpendicular to the ambient magnetic field and a charge separation is established. In order to maintain charge quasi-neutrality, particles need to move along the ambient magnetic field to smear out the charge separation. However, ions move much slower than the wave parallel phase velocity and can be considered stationary with respect to the wave parallel motion. Electrons move along the ambient magnetic field much faster than the wave parallel phase velocity and can move to smear out the charge separation. But, the trapped electrons execute bounce motion and are not effective to smear out the charge separation. Thus, the untrapped electrons will need to smear out the charge separation. However, the untrapped electron fraction is small in the plasma sheet and hence an enhanced parallel electric field is created to accelerate the untrapped electrons along the field line to smear

out the charge separation. From the parallel Ampere's law, $\delta J_\parallel \simeq i\nabla_\perp^2 \boldsymbol{\nabla}_\parallel (\Phi - \Psi)/\omega$, the enhanced perturbed parallel electric field produces an enhanced perturbed parallel current, which represents an enhancement of the field line tension that is to stabilize the ballooning modes.

To obtain a simplified eigenmode equation for analytical understanding of the kinetic ballooning instability due to the kinetic effects of finite ion gyroradii and trapped electron dynamics, we need to make further simplification. If we consider the orderings $\omega \gg \omega_{de}, \omega_{di}$ and $k_\perp \rho_i < 1$ and ignore the effects of $\delta B_\parallel$ and the nonadiabatic density and pressure responses, then the fourth, fifth and sixth terms in Eq. (43) can be ignored [*Cheng*, 1991; *Cheng and Qian*, 1994; *Cheng et al.*, 1995]. The kinetic vorticity equation, Eq. (43), then reduces to

$$\mathbf{B}\cdot\boldsymbol{\nabla}\left[\frac{k_\perp^2}{B^2}\mathbf{B}\cdot\boldsymbol{\nabla}(\Phi-\Psi)\right] + \frac{\omega(\omega-\omega_{*pi})}{V_A^2}\frac{1-\Gamma_0(b_i)}{\rho_i^2/2}\Phi + 2\frac{\mathbf{B}\times\boldsymbol{\kappa}\cdot\mathbf{k}_\perp}{B^2}\frac{\mathbf{B}\times\boldsymbol{\nabla}P\cdot\mathbf{k}_\perp}{B^2}\Phi = 0, \quad (53)$$

where $V_A = B/(n_i M_i)^{1/2}$ is the Alfvén speed. Similarly, we also ignore the perturbed nonadiabatic density responses in Eq. (52), then Eqs. (52) and (53) form a coupled set of kinetic ballooning eigenmode equations for Φ and Ψ along the field lines and the eigenvalue ω. Equations (52) and (53) can be combined to form a simplified kinetic ballooning mode equation

$$\mathbf{B}\cdot\boldsymbol{\nabla}\left[\frac{k_\perp^2}{B^2}\mathbf{B}\cdot\boldsymbol{\nabla}(S\Phi)\right] + \frac{\omega(\omega-\omega_{*pi})}{V_A^2}\frac{1-\Gamma_0(b_i)}{\rho_i^2/2}\Phi + 2\frac{\mathbf{B}\times\boldsymbol{\kappa}\cdot\mathbf{k}_\perp}{B^2}\frac{\mathbf{B}\times\boldsymbol{\nabla}P\cdot\mathbf{k}_\perp}{B^2}\Phi = 0, \quad (54)$$

where

$$S = 1 + \frac{N_e T_e}{(N_{eu}+N_{et}\Delta)T_i}\frac{\omega-\omega_{*pi}}{\omega-\omega_{*e}}(1-\Gamma_0). \quad (55)$$

The simplified kinetic ballooning mode equation retains the kinetic effects of trapped electron dynamics and finite ion gyroradii, and a local dispersion relation for KBI is approximately given by

$$\frac{\omega(\omega-\omega_{*pi})}{(1+b_i)V_A^2} \simeq Sk_\parallel^2 - \frac{2(\mathbf{B}\times\boldsymbol{\kappa}\cdot\mathbf{k}_\perp)(\mathbf{B}\times\boldsymbol{\nabla}P\cdot\mathbf{k}_\perp)}{B^4}. \quad (56)$$

where S is approximated by

$$S = 1 + \frac{b_i}{(1+b_i)} \frac{N_e T_e}{(N_{eu} + N_{et}\Delta) T_i} \gg 1 \tag{57}$$

by neglecting ω_{*e} and ω_{*pi}, and adopting the Padé approximation $1 - \Gamma_0 \simeq b_i/(1+b_i)$. At marginal stability, the real frequency of KBI is $\omega_r = \omega_{*pi}/2$, thus the KBI propagates in the ion diamagnetic drift direction, which is westward for ion pressure gradient pointing earthward, consistent with observations [*Chen et al.*, 2003]. The critical β is given by

$$\beta_c \simeq S\beta_c^{MHD} + \frac{\omega_{*pi}^2 R_c L_p}{4(1+b_i)V_A^2}, \tag{58}$$

where R_c is the radius of the magnetic field curvature and L_p is the pressure gradient scale length, and $\beta_c^{MHD} = k_\parallel^2 R_c L_p$ is the ballooning instability threshold based on the MHD theory. Note that based on the magnetic field and plasma parameters observed by AMPTE/CCE at $X = -8.8\,\mathrm{R_E}$ near midnight equator: $B = 10nT, T_e/T_i = 0.5, b_i = 0.5$, we estimate that $S \simeq 10^2 - 10^3$ and $\beta_c^{MHD} \sim 0.1$ at equator [*Cheng and Qian*, 1994; *Lee*, 1999a], then $\beta_c \simeq S\beta_c^{MHD} \sim 10 - 10^2$, which is consistent with the AMPTE/CCE observation of $\beta_{eq} > 50$ when the low frequency was excited [*Lui et al.*, 1992; *Lui*, 1996]. However, based on the full ideal MHD model the numerical ballooning stability calculations for the growth phase equilibrium (presented in Section 4.3) show that the MHD ballooning modes are unstable ($\omega^2 < 0$) for field lines crossing the equator in the tail region with about $X < -6\,\mathrm{R_E}$ as shown in Fig. 13. Taking into account of the kinetic effects of finite ion gyroradii and trapped electron dynamics, weaker MHD ballooning instabilities in the tail region for $X < -10\,\mathrm{R_E}$ will probably be stabilized. Therefore, we expect that the kinetic ballooning mode will be unstable for the growth phase equilibrium and its amplitude will be localized in the strong cross-tail current sheet region.

Because the ion magnetic drift is in the same direction as the ion diamagnetic pressure gradient drift, it is possible that the wave-ion magnetic drift resonance with

$\omega \sim \omega_{di}$ can occur and modify the growth rate and critical β. To fully evaluate the effect of wave-ion magnetic drift resonance, we need to retain ion nonadiabatic responses in the perturbed density and pressures in the eigenmode equations. Numerical studies of KBI have been performed for tokamaks previously [*Cheng*, 1982b, 1982a] and the results indicated that the effect of the wave-ion magnetic drift resonance is to reduce β_c by at most 20% and the real frequency of KBI will increase to ω_{*pi} at critical β. We expect the results for the magnetosphere will be qualitatively similar to the tokamak case and the detailed numerical solutions will need to be carried out in the future.

Another consequence of the wave-ion magnetic drift resonance is that as the KBI grows to a large amplitude with $\delta B/B \geq 0.3$, ions resonating with the KBI can be accelerated or decelerated depending on the wave phase. As a result the resonant particle flux will increase or decrease near the duskward resonant ion magnetic drift velocity. This can be clearly seen from the $(\omega - \omega_{di})$ resonance denominator in the perturbed nonadiabatic ion distribution given in Eq. (50). Because $\omega_r \simeq \omega_{*pi}$ near marginal stability, the wave-ion magnetic drift resonance will occur at the ion magnetic drift velocity $V_{di} = T_i/(eBL_{pi})$, where T_i is the ion temperature, L_{pi} is the ion pressure gradient scale length. Because $|V_{di}| \simeq \mathcal{E}/(eBL_B)$, where $\mathcal{E}$ is the ion energy and L_B is the magnetic gradient scale length, thus, ions with energy $\mathcal{E} \sim T_i(L_B/L_{pi})$ will resonate with the wave. Typically, $L_B/L_{pi} > 1$ and we expect the ions with energy a few times of its temperature will be in resonance with the KBI, consistent with the AMPTE/CCE observations [*Lui et al.*, 1992; *Lui*, 1996].

4.5. Summary of Substorm Onset mechanism

In this Section we have shown that based on the AMPTE/CCE observations a low frequency instability is excited prior to substorm onset when β_{eq} increases over 50 in the near-Earth plasma sheet region at $X \simeq -(8-9)\,\mathrm{R_E}$. The low frequency instability grows exponentially and lead to substorm onset when its amplitude reaches $\delta B/B > 0.3$.

The low frequency instability is interpreted as a ballooning instability. Based on the ideal MHD model and realistic 3D magnetospheric equilibria for the substorm growth phase, our numerical solutions show that the MHD ballooning modes are unstable for the entire plasma sheet where $\beta_{eq} \geq 1$, but with the most unstable modes located in the strong cross-tail current sheet region in the near-Earth plasma sheet, which maps to the initial brightening location of the breakup arc in the ionosphere. However, the MHD β_{eq} threshold is too low in comparison with observations by AMPTE/CCE at $X \simeq -(8-9)\,\mathrm{R_E}$. The difficulty is mitigated by considering the kinetic effects of finite ion gyroradii and trapped electron dynamics, which can greatly increase the stabilizing effects of field line tension and thus enhance the β_{eq} threshold [*Cheng and Lui*, 1998a]. The consequence is to reduce the equatorial region of the unstable ballooning modes to the strong cross-tail current sheet region where the free energy associated with the plasma pressure gradient and magnetic field curvature is maximum. Moreover, the kinetic theory of ballooning modes predicts the correct mode frequency and provides a generation mechanism for the parallel electric field, which is required to accelerate particles to produce the substorm onset auroral brightening as observed in the ionosphere.

5. Dipolarization

In high β_{eq} region, an efficient mechanism to cause magnetic field dipolarization is via the reduction in plasma pressure. We will show that as a result of plasma transport due to plasma turbulence, a small reduction of plasma pressure in the plasma sheet can cause significant increase in the magnetic field intensity and thus dipolarize the magnetic field.

From the AMPTE/CCE observations, we find that as the KBI grows to a large amplitude with $\delta B/B \geq 0.3$, the substorm is initiated in a localized region. At the current disruption onset higher frequency instabilities (with wave periods 15 sec, 10, sec, 5 sec, etc.) are also excited and they are identified as the cross-field current instability (CCI)

[*Lui*, 1996] driven unstable by the velocity space free energy associated the enhanced duskward ion drift fluxes during the current disruption phase. The KBI combines with the higher frequency instabilities to form a strong turbulent state [*Takahashi et al.*, 1987a; *Roux et al.*, 1991; *Lui et al.*, 1992; *Ohtani et al.*, 1995; *Lui*, 1996; *Cheng and Lui*, 1998a; *Erickson et al.*, 2000]. The turbulence expands in all directions (but more in the tailward direction) perhaps due to the nonlinear growth of the KBI through out the expansion phase.

During the expansion phase the current disruption and magnetic field dipolarization occur in the plasma sheet. There are different ideas how the magnetic field dipolarization occurs, such as the magnetic flux transport from the far tail by fast plasma earthward flow [*Angelopoulos et al.*, 1992, 1994; *Nagai et al.*, 1998; *Baumjohann et al.*, 1999; *Miyashita et al.*, 2000; *Ieda et al.*, 2001]. Here, we present a mechanism based on the anomalously fast plasma transport, which causes the plasma pressure profile to relax and the pressure to reduce in the current disruption region as observed by AMPTE/CCE [*Lui et al.*, 1992]. Because the plasma β_{eq} is much larger than unity in the current disruption region, a small reduction in the plasma pressure can cause a large increase in the magnetic field intensity, as will be shown below.

To determine how the plasma sheet ambient magnetic field changes during the expansion phase, we make use of the observations that the plasma and fields are in a turbulent state with the dominant fluctuation time scales ranging from a few seconds to about 100 seconds, and the fluctuation wavelengths are less than the ambient magnetic field and pressure scale lengths. Moreover, we make use of the observational fact that the plasma flow energy, $\rho|\mathbf{V}|^2$ is less than the magnetic and plasma thermal energy. Then, by averaging the momentum equation over the short temporal and spatial scales associated with these fluctuations, we obtain the quasi-static equilibrium equation for the ambient quantities

$$\langle \mathbf{J} \rangle \times \langle \mathbf{B} \rangle - \boldsymbol{\nabla} \langle P \rangle \simeq 0, \tag{59}$$

where $\langle P\rangle$ indicates the average of P, and the quadratic terms in the perturbed quantities are assumed to be smaller. Then, using $\langle \mathbf{J}\rangle = \boldsymbol{\nabla} \times \langle \mathbf{B}\rangle$, we have

$$\boldsymbol{\nabla}\langle P + \frac{B^2}{2}\rangle \simeq \langle \boldsymbol{\kappa}\rangle\langle B^2\rangle, \tag{60}$$

Near equator, as the ambient magnetic field becomes dipolarize, $\langle B\rangle$ increases but the field curvature $\langle \boldsymbol{\kappa}\rangle$ decreases such that $\langle \boldsymbol{\kappa}\rangle\langle B^2\rangle$ remains relatively unchanged. Then, to a good approximation we have $\partial\langle P + \frac{B^2}{2}\rangle/\partial t \simeq 0$ and $\langle P + \frac{B^2}{2}\rangle$ remains approximately constant during the expansion phase. Thus, a reduction in $\langle P\rangle$ can cause $\langle B\rangle$ to increase by a factor of $\sqrt{1+\beta\delta}$, where δ is the fraction of reduction in $\langle P\rangle$. In the $\beta \gg 1$ equatorial region, say $\beta = 50$, a fractional reduction of $\delta = 0.1$ in $\langle P\rangle$ will cause $\langle B\rangle$ to increase by a factor of $\sqrt{6}$. This estimate is consistent with the AMPTE/CCE observations shown in Fig. 12(d). Therefore, if the strong turbulence causes plasma transport and reduces the mean plasma pressure and modifies its profile, then the ambient magnetic field recovers from a tail-like geometry to a dipole-like geometry. Associated with the dipolarization, an enhanced duskward electric field is produced, which causes dispersionless energetic particle injections observed by geosynchronous satellites [e.g., *Zaharia et al.*, 2000].

It is emphasize that the magnetic field dipolarization process proposed above works only for $\beta_{eq} \gg 1$ region. For $\beta_{eq} \leq 1$ region, it would require the transport of magnetic flux via processes such as magnetic reconnection to cause a significant magnetic field dipolarization in the near-Earth plasma sheet region. However, there are tremendous difficulties from the theoretical standpoints for magnetic reconnection to play a direct role in causing the substorm onset and subsequent dipolarization as will be discussed in the next Section.

6. Magnetic Reconnection and Substorm

An alternative idea in the space plasma physics community regarding the mechanism responsible for the substorm onset and subsequent magnetic field dipolarization in the

plasma sheet is based on the concept of magnetic reconnection [*Sweet*, 1958; *Parker*, 1963; *Petschek*, 1964]. There are two elements in the magnetic reconnection process [*Kulsrud*, 1998]: one is the change of magnetic field topology, and the other is the rate of energy conversion from magnetic field energy to plasma thermal and flow energies. The study of the physical process of magnetic reconnection is still an intensively ongoing activity in the plasma physics community. Some critical issues of magnetic reconnection are still being pursued: how current sheets form and what the current sheet topology is; how magnetic field reconnects in a 3D sheared magnetic field; what causes reconnection (external force or internal waves or instabilities); what the reconnection rate is; whether reconnection processes are steady or spontaneous; and how electrons and ions gain energy; etc.

Despite insufficient understanding of these time-dependent magnetic reconnection physics in 3D geometries, there have been attempts to propose the magnetic reconnection as the substorm onset and expansion phase mechanism. In particular, the near-earth neutral line model [e.g., *McPherron et al.*, 1973; *Nagai and Kamide*, 1995; *Baker et al.*, 1996; *Shiokawa et al.*, 1998], which has gained popularity, postulates that the substorm expansion phase is caused by magnetic reconnection in the near-earth plasma sheet at $X > -(15-20)\,\mathrm{R_E}$. The near-Earth neutral line model is based on the scenario that the plasma and magnetic field are pinched by oppositely directed flows from north and south to form a current sheet in the equatorial near-Earth plasma sheet region. As magnetic reconnection occurs via plasma dissipation, both earthward and tailward flows are generated to transport plasma and magnetic flux. In particular, the earthward flow is expected to carry sufficient magnetic flux to dipolarize the magnetic field in the near-Earth plasma sheet region. In order for magnetic reconnection to be a viable mechanism for the substorm onset, expansion and magnetic field dipolarization, several serious difficulties of the near-Earth neutral line model associated with both observational and theoretical constraints must be addressed. In the following we discuss a few of these difficulties.

First, the effort by MHD simulations to find out whether magnetic reconnection can occur in the near-Earth plasma sheet region has been carried out. It is a common conclusion that under normal solar wind and IMF conditions observed during substorms magnetic reconnection does not occur in the near-earth plasma sheet region of $X > -15\,\mathrm{R_E}$. Even when magnetic reconnection occurs in the near-Earth plasma sheet under unrealistic solar wind and IMF conditions employed in the MHD simulations, the reconnection region is quite broad ($>$ 3 hours in local time and $> 3\,\mathrm{R_E}$ in radial direction) in the equatorial region [*Ogino and Walker*, 1998; *Tanaka*, 2000]. This is inconsistent with the observation that the substorm onset is initiated in a small localized region of less than $1\,\mathrm{R_E}$ wide in the equatorial plane at $x \sim -10\,\mathrm{R_E}$ around midnight, which corresponds to a localized initial aurora brightening region of less than a few degrees wide in longitude and less than one degree wide in latitude in the ionosphere. On the other hand, it is natural for us to expect that the kinetic ballooning instability will be initiated in a localized region in the near-Earth plasma sheet where the plasma β_{eq} is large, plasma pressure gradient and magnetic field curvature are strong so that the instability driving free energy is maximized. Although recent observations from CLUSTER satellites have identified the X-line feature of magnetic field at $X \simeq -18\,\mathrm{R_E}$, the timing of the formation of the X-line is usually different from the substorm onset time [e.g., *Baker et al.*, 2002]. If such an X-line magnetic field configuration is formed during the growth phase, the associated magnetic reconnection can perhaps cause an enhanced earthward plasma convection usually observed during the late growth phase. The enhanced earthward plasma convection can be responsible for the plasma pressure buildup and strong cross-tail current sheet formation before substorm onset. If the X-line field configuration is formed during the substorm expansion phase, it can be attributed to be a consequence of the plasma transport process associated with the plasma turbulence during the current disruption.

Secondly, the AMPTE/CCE observation of magnetic field data during substorms

has clearly identified a low frequency instability which is excited before substorm onset and continues to evolve and together with higher frequency fluctuations develop into a strong plasma turbulence during the expansion phase. There is no physical explanation of the low frequency instability and the turbulence based on the near-Earth neutral line reconnection model. On the other hand, the low frequency instability can be naturally explained in terms of the kinetic ballooning instability which requires kinetic effects of finite ion Larmor radii and trapped electron dynamics to properly understand the high threshold of β_{eq} (≥ 50), the observed wave frequency and growth rate, and the associated parallel electric field that is required to accelerate particle into and out of the auroral ionosphere.

Thirdly, it is required that the magnetic reconnection process in the near-earth plasma sheet region must produce observable high speed earthward plasma flows perpendicular to the field lines before and during the substorm expansion phase. It relies on the earthward flow to carry plasma and magnetic flux to cause magnetic field dipolarization in the near-Earth plasma sheet region. The near-Earth neutral line model advocates have been arguing that the existence of high speed flows is manifested by the bursty bulk flows (BBF) [e.g., *Angelopoulos et al.*, 1992]. However, more recent analysis of the GEOTAIL data has indicated that there is no statistically favorable evidence of large perpendicular earthward flows within $25\,\mathrm{R_E}$ from the Earth in the night side [*Lui et al.*, 1998; *Miyashita et al.*, 2000] prior to substorm onset. Moreover, recent detailed data analysis indicates that earthward flows are mostly related to field-aligned ion beams. More recently, based on the Geotail observations the low frequency flow oscillations in the Pi 2 range are found to be related to MHD perturbations [*Shiokawa et al.*, 2003].

Based on the above discussions, it is unlikely that reconnection will be the direct driver of the substorm onset. However, magnetic reconnection can be an effective means in the storage of energy in the plasma sheet during the growth phase if the reconnection occurs beyond $X \simeq -15\,\mathrm{R_E}$ in the magnetotail. It can also provide a channel to release

plasma energy in the far tail in the substorm expansion phase as evidenced by the poleward expansion of the polar cap (open-closed field line) boundary in the ionosphere in the late expansion phase [*Voronkov et al.*, 2003]. **Figure 17.**

7. Summary and Discussion

In this paper we have proposed a substorm scenario and the corresponding physical processes of substorm growth phase, onset, and dipolarization in the expansion phase based on observations and theories. Fig. 17 summarizes the substorm scenario. The physical processes are demonstrated by the numerical solutions of 3D magnetospheric equilibria for the substorm growth phase and MHD ballooning instabilities as well as the analytical theories of kinetic ballooning modes and magnetic field dipolarization. Moreover, these numerical solutions and analytical theories are shown to be consistent with ground-based and satellite observations of substorms in the ionosphere and the plasma sheet.

During the substorm growth phase the plasma pressure in the equatorial region of the plasma sheet increases on a time scale of tens of minutes due to enhanced convection and β_{eq} increases from $O(1)$ to 10 - 20 in the near-Earth plasma sheet region. plasma pressure and its gradient are continued to increase over the quiet-time values in the plasma sheet. Toward the end of the growth phase at approximately 2-3 minutes before the current disruption onset, a strong cross-tail current sheet is formed in the near-Earth plasma sheet region ($\sim 7 - 12\,\mathrm{R_E}$), where a local magnetic well is formed, β_{eq} reaches a local maximum with value larger than 50 and the cross-tail current density is enhanced to over $10\,\mathrm{nA/m^2}$. This current sheet region maps to the transition region between the regions of the region-1 and the region-2 currents in the ionosphere. Based on the ionospheric observations this transition region coincides with the intense proton precipitation region, which is located near the equatorward edge of the soft electron precipitation (or electron aurora) observed during the late growth phase.

Based on the AMPTE/CCE observations, a low frequency instability with period of about $50 - 75$ seconds is excited at about 2-3 minutes before the current disruption onset in the strong current sheet region, grows exponentially to a large amplitude with $\delta B/B > 0.3$, and initiates the substorm onset. The low frequency instability is explained in terms of the kinetic ballooning instability, which can be driven unstable in the enhanced cross-tail current sheet region due to high β_{eq}, pressure gradient and enhanced tail-like magnetic field curvature. Based on the ideal MHD model, the β_{eq} threshold for the ballooning instability is about unity. Numerical solutions of the ballooning instability based on the growth phase magnetospheric equilibria show that the most unstable ballooning instabilities are located in the tailward side of the strong cross-tail current sheet region, whose field lines map to the transition region between the region-1 and region-2 currents in the ionosphere, which is consistent with the observed initial brightening location of the breakup arc in the intense proton precipitation region.

However, the β_{eq} threshold obtained from the ideal MHD ballooning mode stability calculationsis much smaller than the typical β_{eq} values observed in the near-Earth plasma sheet region. Observations show that during most of the growth phase $\beta_{eq} < 50$ and the magnetic fields are quiet without noticeable fluctuations [*Lui et al.*, 1992], and the low frequency instability was observed in the enhanced cross-tail current sheet region only near the end of the growth phase when $\beta_{eq} > 50$ [*Cheng and Lui*, 1998a]. Moreover, the ideal MHD model would predict purely growing ballooning instabilities, and thus can not explain the observed frequency of the instability. Another fundamental difficulty of the ideal MHD model is that there is no parallel electric field, and thus the unstable MHD ballooning mode does not accelerate particles to produce the substorm onset auroral brightening observed in the ionosphere. However, even with these inconsistencies with observations, the ideal MHD model provides the valuable information that the most unstable ballooning instability and the maximum free energy associated with the plasma pressure gradient and magnetic field curvature are located in the strong cross-tail current

sheet region. To mitigate these difficulties arising from the ideal MHD model, we need to consider the particle kinetic effects. As was shown previously [*Cheng and Lui*, 1998a], the kinetic effects of ion gyroradii and trapped electron dynamics give rise to a large parallel electric field and hence a parallel current that greatly enhances the stabilizing effect of field line tension. Thus, the β_{eq} threshold for ballooning instability is enhanced to a value of ≥ 50 consistent with observations. As a consequence, the region for unstable ballooning modes is reduced to the strong cross-tail current sheet region, where the free energy for the ballooning instability is maximum.

As KBI grows to a large amplitude, the wave-ion resonance with $\omega - \omega_{di} = 0$ produces a perturbed ion distribution centered at a duskward velocity roughly equal to the average ion magnetic drift velocity. This perturbed ion distribution explains the enhanced duskward ion flux during the explosive growth phase, and provides the velocity space free energy to excite higher frequency instabilities (such as the cross-field current instability). As these low and high frequency instabilities grow, a strong plasma turbulence is developed fully to yield large plasma transport (possibly via diffusion, convection as well as magnetic reconnection) and heating. In a few minutes the average plasma pressure profile (averaged over the fast fluctuation time and space scales) is relaxed by the plasma transport and the averaged pressure in the cross-tail current sheet is reduced by about 10% so that the magnetic field intensity increases by more than a factor of 2, and the ambient magnetic field recovers from a tail-like geometry to a more dipole-like geometry.

In Summary, the substorm is the major energy regulating process in the magnetosphere (particularly in the plasma sheet) and the ionosphere, and significant progress has been made in both observations and theories. Although the theoretical progress in understanding of the substorm dynamics has been achieved, quantitative comparisons of theories and simulations with observations have not yielded satisfactory results. This is mainly because detailed theoretical calculations and realistic numerical

simulations including kinetic physics for understanding the substorm processes in 3D geometries have not yet been performed. Moreover, observations with multiple point measurements also need to be carried out in order to provide unambiguous physical pictures of substorms.

Acknowledgments. This work is supported by the NASA grant No. W-10062 and the DoE Contract No. DE-AC02-76-CHO3073. The author would like to thank Drs. Sorin Zaharia and A. T. Y. Lui for valuable discussions and help in preparing the paper.

References

Akasofu, S.-I., *Physics of Magnetospheric Substorms*. 1977.

Angelopoulos, V., W. Baumjohann, C. F. Kennel, F. V. Coroniti, M. G. Kivelson, R. Pellat, R. J. Walker, H. Luhr, and G. Paschmann, Bursty bulk flows in the inner central plasma sheet, *J. Geophys. Res.*, *97*, 4027, 1992.

Angelopoulos, V., et al., Statistical characteristics of bursty bulk flow events, *J. Geophys. Res.*, *99*, 21,257, 1994.

Antonsen, Jr., T. M., and B. Lane, Kinetic equations for low frequency instabilities in inhomogeneous plasmas, *Phys. Fluids*, *23*, 1205–1214, 1980.

Baker, D. N., T. I. Pulkkinen, V. Angelopoulos, W. Baumjohann, and R. L. McPherron, Neutral line model of substorms: Past results and present view, *J. Geophys. Res.*, *101*, 12975, 1996.

Baker, D. N., et al., Timing of magnetic reconnection initiation during a global magnetospheric substorm onset, *Geophys. Res. Lett.*, *29*, 2190, 10.1029/2002GL015539, 2002.

Baumjohann, W., M. Hesse, S. Kokubun, T. Mukai, T. Nagai, and A. A. Petrukovich, Substorm dipolarization and recovery, *J. Geophys. Res.*, *104*, 24,995, 1999.

Becker, U., T. Neukirch, and K. Schindler, On the quasistatic development of thin current sheets in magnetotail-like magnetic fields, *J. Geophys. Res.*, *106*(A3), 3811, 2001.

Bhattacharjee, A., Z. W. Ma, and X. Wang, Ballooning instability of a thin current sheet in the high Lundquist-number magnetotail, *Geophys. Res. Lett.*, *25*, 861, 1998.

Birmingham, T. J., Birkeland currents in an anisotropic, magnetostatic plasma, *J. Geophys. Res.*, *97*, 3907, 1992.

Birn, J., and K. Schindler, Thin current sheets in the magnetotail and the loss of equilibrium, *J. Geophys. Res.*, *107*(A7), 1117, doi: 10.1029/2001JA000291, 2002.

Blanchard, G. T., L. R. Lyons, and J. C. Samson, Accuracy of using 6300 A auroral emission to identify the magnetic separatrix on the nightside of earth, *J. Geophys. Res.*, *102*, 9697, 1997.

Borovsky, J. E., M. F. Thomsen, R. C. Elphic, T. E. Cayton, and D. J. McComas, The transport of plasma sheet material from the distant tail to geosynchronous orbit, *J. Geophys. Res.*, *103*, 20297, 1998.

Catto, P. J., W. M. Tang, and D. E. Baldwin, Generalized gyrokinetics, *Plasma Phys.*, *23*, 639–650, 1981.

Chen, L.-J., A. Bhattacharjee, K. Sigsbee, G. Parks, M. Fillingim, and R. Lin, Wind observations pertaining to current disruption and ballooning instability during substorms, *Geophys. Res. Lett.*, *30(6)*, 1335, doi:10.1029/2002GL016317, 2003.

Cheng, C. Z., High-n collisionless ballooning modes in axisymmetric toroidal plasmas, *Nucl. Fusion*, *22*, 773–781, 1982a.

Cheng, C. Z., Kinetic theory of collisionless ballooning modes, *Phys. Fluids*, *25*, 1020–1026, 1982b.

Cheng, C. Z., A kinetic-magnetohydrodynamic model for low-frequency phenomena, *J. Geophys. Res.*, *96*, 21,159–21,171, 1991.

Cheng, C. Z., Magnetospheric equilibrium with anisotropic pressure, *J. Geophys. Res.*, *97*, 1497, 1992.

Cheng, C. Z., Three-dimensional magnetospheric equilibrium with isotropic pressure, *Geophys. Res. Lett.*, *22*, 2401, 1995.

Cheng, C. Z., MHD field line resonances and global modes in three-dimensional magnetic fields, *J. Geophys. Res.*, *108(A1)*, 1002, doi:10.1029/2002JA009470, 2003.

Cheng, C. Z., and J. R. Johnson, A kinetic-fluid model, *J. Geophys. Res.*, *104*, 413–427, 1999.

Cheng, C. Z., and A. T. Y. Lui, Kinetic ballooning instability for substorm onset and current disruption observed by AMPTE/CCE, *Geophys. Res. Lett.*, *25*, 4091–4094, 1998a.

Cheng, C. Z., and A. T. Y. Lui, Physical processes of substorm onset and current disruption observed by AMPTE/CCE, in *Substorms-4*, edited by S. Kokubun, and Y. Kimide, pp. 455–459. Terra Scientific Pub. Co. and Kluwer Acad. Pub., 1998b.

Cheng, C. Z., and Q. Qian, Theory of ballooning-mirror instabilities for anisotropic pressure plasmas in the magnetosphere, *J. Geophys. Res.*, *99*, 11,193–11,209, 1994.

Cheng, C. Z., and S. Zaharia, Field line resonances in quiet and disturbed time three dimensional magnetospheres, *J. Geophys. Res.*, *108(A1)*, 1001, doi:10.1029/2002JA009471, 2003a.

Cheng, C. Z., and S. Zaharia, MHD ballooning instability in the plasma sheet, *J. Geophys. Res.*, submitted in October, 2003b.

Cheng, C. Z., N. N. Gorelenkov, and C. T. Hsu, Fast particle destabilization of TAE modes, *Nucl. Fusion*, *35*, 1639–1650, 1995.

De Michelis, P., I. A. Daglis, and G. Consolini, An average image of proton plasma pressure and of current systems in the equatorial plane derived from AMPTE/CCE-CHEM measurements, *J. Geophys. Res.*, *104*, 28615, 1999.

Dewar, R. L., and A. H. Glasser, Ballooning mode spectrum in general toroidal systems, *Phys. Fluids*, *26*, 3038, 1983.

Dewar, R. L., P. Cuthbert, and R. Ball, Strong quantum chaos in the global ballooning mode spectrum of three-dimensional plasmas, *Phys. Rev. Lett.*, *86*, 2321, 2001.

Erickson, G. M., A quasi-static magnetospheric convection model in two-dimensions, *J. Geophys. Res.*, *97*, 6505, 1992.

Erickson, G. M., N. C. Maynard, W. J. Burke, G. R. Wilson, and M. A. Heinemann, Electromagnetics of substorm onsets in the near-geosynchronous plasma sheet, *J. Geophys. Res.*, *105*, 25265–25290, 2000.

Frank, L. A., and J. B. Sigwarth, Findings concerning the positions of substorm onsets with auroral images from the Polar spacecraft, *J. Geophys. Res.*, *105*, 12,747, 2000.

Frank, L. A., J. B. Sigwarth, and W. R. Paterson, High resolution global images of Earth's auroras during substorms, in *in SUBSTORM-4, International Conf. on Substorms-4, European Space Agency Spec. Publ. SP-335*, p. 3. 1998.

Friedrich, E., J. C. Samson, I. Voronkov, and G. Rostoker, Dynamics of the substorm expansive phase, *J. Geophys. Res.*, *106*, 13,145, 2001.

Grad, H., Some new variational properties of hydromagnetic equilibria, *Phys. Fluids*, *7*, 1283, 1964.

Hau, L., Effects of steady state adiabatic convection on the configuration of the near-Earth plasma sheet, *J. Geophys. Res.*, *96*(A4), 5591, 1991.

Heinemann, M., and D. H. Pontius, Jr., Representations of currents and magnetic fields in isotropic magnetohydrostatic plasma, *J. Geophys. Res.*, *95*, 251, 1990.

Horton, W., H. V. Wong, and J. W. Van Dam, Substorm trigger conditions, *J. Geophys. Res.*, *104*, 22745, 1999.

Hurricane, O. A., MHD ballooning stability of a sheared plasma sheet, *J. Geophys. Res.*, *102*, 19903, 1997.

Hurricane, O. A., R. Pellat, and F. V. Coroniti, The kinetic response of a stochastic plasma to low frequency perturbations, *Geophys. Res. Lett.*, *21*, 253, 1994.

Hurricane, O. A., R. Pellat, and F. V. Coroniti, The stability of a stochastic plasma with respect to low frequency perturbations, *Phys. Plasmas*, *2*, 289, 1995.

Ieda, A., et al., Plasmoid ejection and auroral brightenings, *J. Geophys. Res.*, *106*, 3845, 2001.

Iijima, T., and T. A. Potemra, The amplitude distribution of field-aligned currents at northern high latitudes observed by Triad, *J. Geophys. Res.*, *81*, 2165, 1976a.

Iijima, T., and T. A. Potemra, Field-aligned currents in the dayside cusp observed by Triad, *J. Geophys. Res.*, *81*, 5971, 1976b.

Kamide, Y., How and where auroral breakup begins: An example of multi-scale phenomena in space, *Physics of Space Plasmas*, *15*, 197, 1998.

Kan, J., On the structure of the magnetotail current sheet, *J. Geophys. Res.*, *78*, 3773, 1973.

Kaufman, R. L., B. M. Ball, W. R. Paterson, and L. A. Frank, Plasma sheet thickness and electric currents, *J. Geophys. Res.*, *106*, 6179–6194, 2001.

Kaufman, R. L., C. Lu, W. R. Paterson, and L. A. Frank, Three-dimensional analyses of electric

currents and pressure anisotropies in the plasma sheet, *J. Geophys. Res.*, *107*, 1103, DOI 10.1029/2001JA000288, 2002.

Kistler, L. M., E. Mobius, W. Baumjohann, G. Paschmann, and D. C. Hamilton, Pressure changes in the plasma sheet during substorm injections, *J. Geophys. Res.*, *97*, 2973, 1992.

Kubyshkina, M. V., V. A. Sergeev, S. V. Dubyagin, S. Wing, P. T. Newell, W. Baumjohann, and A. T. Y. Lui, Constructing the magnetospheric model including pressure measurements, *J. Geophys. Res.*, *107*, doi:10.1029/2001JA900167, 2002.

Kulsrud, R. M., Magnetic reconnection in a magnetohydromagnetic plasma, *Phys. Plasmas*, *5*, 1599, 1998.

Lee, D. Y., Ballooning instability in the tail plasma sheet, *Geophys. Res. Lett.*, *25*, 4095, 1998.

Lee, D. Y., Effect of plasma compression on plasma sheet stability, *Geophys. Res. Lett.*, *26*, 2705, 1999a.

Lee, D. Y., Stability analysis of the plasma sheet using Hall magnetohydromagnetics, *J. Geophys. Res.*, *104*, 19,993, 1999b.

Lee, D. Y., and R. A. Wolf, Is the Earth's magnetotail balloon unstable?, *J. Geophys. Res.*, *97*, 19251, 1992.

Lee, L. C., L. Zhang, G. S. Choe, and H. J. Cai, Formation of a very thin current sheet in the near-earth magnetotail and the explosive growth phase of substorms, *Geophys. Res. Lett.*, *22*, 1137, 1995.

Lee, L. C., L. Zhang, A. Otto, G. S. Choe, and H. J. Cai, Entropy antidiffusion instability and formation of a thin current sheet during geomagnetic substorms, *J. Geophys. Res.*, *103*, 29419, 1998.

Liou, K., C. I. Meng, A. T. Y. Lui, P. T. Newell, M. Brittnacher, G. Parks, G. D. Reeves, R. R. Anderson, and K. Yumoto, On relative timing in substorm onset signatures, *J. Geophys. Res.*, *104*, 22,807, 1999.

Liou, K., C. I. Meng, P. T. Newell, K. Takahashi, S. Ohtani, A. T. Y. Lui, M. Brittnacher, and G. Parks, Evaluation of low-latitude Pi 2 pulsations as indicators of substorm onset using Polar ultraviolet imagery, *J. Geophys. Res.*, *105*, 2495, 2000.

Liu, W. W., Physics of the explosive growth phase: Ballooning instabilities revisited, *J. Geophys. Res.*, *102*, 4927, 1997.

Lui, A. T. Y., Inferring global characteristics of current sheet from local measurements, *J. Geophys. Res.*, *98*(A8), 13423, 1993.

Lui, A. T. Y., Current disruption in the Earth's magnetosphere: Observations and models, *J. Geophys. Res.*, *101*(A6), 13067, 1996.

Lui, A. T. Y., and C. Z. Cheng, Resonant frequency of stretched magnetic field lines based on a self-consistent equilibrium magnetosphere model, *J. Geophys. Res.*, *106*, 25793 – 25802, 2001.

Lui, A. T. Y., and D. C. Hamilton, Radial profiles of quiet time magnetospheric parameters, *J. Geophys. Res.*, *97*, 19325, 1992.

Lui, A. T. Y., and A.-H. Najmi, Time-frequency decomposition of signals in a current disruption event, *Geophys. Res. Lett.*, *24*, 3157, 1997.

Lui, A. T. Y., R. W. McEntire, and S. M. Krimigis, Evolution of the ring current during two geomagnetic storms, *J. Geophys. Res.*, *92*, 7459, 1987.

Lui, A. T. Y., C. L. Chang, A. Mankofsky, H. K. Wong, and D. Winske, A cross-field current instability for substorm expansions, *J. Geophys. Res.*, *96*, 11389, 1991.

Lui, A. T. Y., et al., Current disruptions in the near-Earth neutral sheet region, *J. Geophys. Res.*, *97*, 1461, 1992.

Lui, A. T. Y., H. E. Spence, and D. P. Stern, Empirical modeling of the quiet time nightside magnetosphere, *J. Geophys. Res.*, *99*, 151, 1994.

Lui, A. T. Y., et al., Special features of a substorm during high solar wind dynamic pressure, *J. Geophys. Res.*, *100*, 19095, 1995.

Lui, A. T. Y., K. Liou, P. T. Newell, C.-I. Meng, S.-I. Ohtani, S. Kokubun, T. Ogino, M. Brittnacher, and G. Parks, Plasma and magnetic flux transport associated with auroral breakups, *Geophys. Res. Lett.*, *25*, 4059, 1998.

Lyons, L. R., I. O. Voronkov, E. F. Donovan, and E. Zesta, Relation of substorm breakup arc to other growth-phase auroral arcs, *J. Geophys. Res.*, *107*, 1390, DOI 10.1029/2002JA009317, 2002.

Maynard, N. C., et al., Dynamics of the inner magnetosphere near times of substorm onsets, *J. Geophys. Res.*, *101*, 7705, 1996.

McPherron, R. L., Growth phase of magnetospheric substorms, *J. Geophys. Res.*, *75*, 5592, 1970.

McPherron, R. L., C. T. Russell, and M. P. Aubry, Satellite studies of magnetospheric model for substorms, *J. Geophys. Res.*, *78*, 3131, 1973.

Mishin, V. M., C. T. Russell, T. I. Saifudinova, and A. D. Bazarzhapov, Study of weak substorms observed during October 8. 1990, Geospace Environmental Campaign: Timing of different types of substorm onset, *J. Geophys. Res.*, *105*, 15,913, 2000.

Miyashita, Y., S. Machida, T. Mukai, Y. Saito, K. Tsuruda, H. Hayakawa, and P. R. Sutcliffe, A statistical study of variations in the near and mid-distant magnetotail associated with substorm onset: Geotail observations, *J. Geophys. Res.*, *105*, 15,913, 2000.

Murphree, J. S., and M. L. Johnson, Clues to plasma processes based on Freja UV observations, *Adv. Space Res.*, *18*, 95, 1996.

Nagai, T., and Y. Kamide, Magnetic field changes at the neutral sheet associated with substorm expansion onset: A model prediction and observation, *J. Geophys. Res.*, *100*, 3521, 1995.

Nagai, T., et al., Structure and dynamics of magnetic reconnection for substorm onsets with Geotail observations, *J. Geophys. Res.*, *103*, 4419, 1998.

Nevins, W. M., and L. D. Pearlstein, Moderate-m ballooning modes in quadrapole stabilized tandem mirrors, *Phys. Fluids*, *31*, 1988, 1988.

Ogino, T., and R. J. Walker, Response of the magnetosphere to a southward turning of IMF: Energy flow and near Earth tail dynamics, in *in SUBSTORM-4, International Conf. on Substorms-4, European Space Agency Spec. Publ. SP-335*, p. 635. 1998.

Ohtani, S., and T. Tamao, Does the ballooning instability trigger substorms in the near-Earth magnetotail?, *J. Geophys. Res.*, *98*, 19369, 1993.

Ohtani, S., K. Takahashi, L. J. Zanetti, T. A. Potemra, R. W. McEntire, and T. Iijima, Tail current disruption in the geosynchronous region, edited by J. R. Kan, T. A. Potemra, S. Kokubun, and T. Iijima, in *AGU monograph on Magnetospheric Substorms*, pp. 131–137. AGU, Washington, D. C., 1991.

Ohtani, S., K. Takahashi, L. Zanetti, T. A. Potemra, R. W. McEntire, and T. Iijima, Initial signatures of magnetic field and energetic particle fluxes at tail reconfiguration: Explosive growth phase, *J. Geophys. Res.*, *97*, 19311, 1992.

Ohtani, S., T. Higuchi, A. T. Y. Lui, and K. Takahashi, Magnetic fluctuations associated with tail current disruption: Fractal analysis, *J. Geophys. Res.*, *100*, 19135, 1995.

Parker, E. N., The solar flare phenomenon and the theory of reconnection and annihilation ofmagnetic fields, *Astrophys. J. Suppl. Series*, *8*, 177, 1963.

Petschek, H. E., Magnetic field annihilation, in *AAS-NASA Symposium on the Physics of Solar Flares*, Washington, DC. NASA Spec. Publ., SP-50, 1964.

Pulkkinen, T. I., et al., Thin current sheets in the magnetotail during substorms: CDAW 6 revisited, *J. Geophys. Res.*, *99*, 5793, 1994.

Pulkkinen, T. I., et al., Spatial extent and dynamics of a thin current sheet during the substorm growth phase on December 10, 1996, *J. Geophys. Res.*, *104*(A12), 28475, 1999.

Reeves, G. D., G. Kettmann, T. A. Fritz, and R. D. Belian, Further investigation of the CDW 7 substorm using geosynchronous particle data: Multiple injections and their implications, *J. Geophys. Res.*, *97*, 6417, 1992.

Rostoker, G., The evolving concept of of a magnetospheric substorm, *J. Atmos. Terr. Phys.*, *61*, 85, 1999.

Rostoker, G., S.-I. Akasofu, J. Foster, G. R. A, Y. Kamide, K. Kawasaki, A. T. Y. Lui, R. L. McPherron, and C. T. Russell, Magnetospheric substorms – Definition and signature, *J. Geophys. Res.*, *85*, 1663, 1980.

Roux, A., S. Perraut, A. Morane, P. Robert, A. Korth, G. .Kremser, A. Pederson, R. Pellinen, and Z. Y. Pu, Plasma sheet instability related to the westward traveling surge, *J. Geophys. Res.*, *96*, 17697, 1991.

Samson, J. C., L. R. Lyons, P. T. Newell, F. Creutzberg, and B. Xu, Proton aurora and substorm intensifications, *Geophys. Res. Lett.*, *19*, 2167, 1992a.

Samson, J. C., D. D. Wallis, T. J. Hughes, F. Creutzberg, J. M. Ruohoniemi, and R. A. Greenwald, Substorm intensifications and field line resonances in the nightside magnetosphere, *J. Geophys. Res.*, *97*, 8495, 1992b.

Sanny, J., R. L. McPherron, C. T. Russell, D. N. Baker, T. I. Pulkkinen, and A. Nishida, Growth-phase thinning of the near-Earth current sheet during the CDAW 6 substorm, *J. Geophys. Res.*, *99*(A4), 5805, 1994.

Sergeev, V. A., P. Tanskanen, K. Mursula, A. Korth, and R. C. Elphic, Current sheet thickness in the near-earth plasma sheet during substorm growth phase, *J. Geophys. Res.*, *95*, 3819, 1990.

Sergeev, V. A., D. G. Mitchell, C. T. Russell, and D. J. Williams, Structure of the tail plasma/current sheet at $\approx 11R_E$ and its changes in the course of a substorm, *J. Geophys. Res.*, *98*, 17345, 1993a.

Sergeev, V. A., M. Malkov, and K. Mursula, Testing the isotropic boundary algorithm method to evaluate the magnetic field configuration in the tail, *J. Geophys. Res.*, *98*, 7609, 1993b.

Sergeev, V. A., V. Angelopoulos, C. Carlson, and P. Sutcliffe, Current sheet measurements within a flapping plasma sheet, *J. Geophys. Res.*, *103*, 9177, 1998.

Shiokawa, K., G. Haerendel, and W. Baumjohann, Azimuthal pressure gradient as driving force of substorm currents, *Geophys. Res. Lett.*, *25*(7), 959, 1998.

Shiokawa, K., I. Shinohara, T. Mukai, H. Hayakawa, and C. Z. Cheng, Substorm-associated

magnetic field fluctuations around X = -10 Re in the near-Earth tail, *J. Geophys. Res.*, to be submitted, 2003.

Spence, H. E., and M. G. Kivelson, Contributions of the low-latitude boundary layer to the finite width magnetotail convection model, *J. Geophys. Res.*, *98*, 15487, 1993.

Spence, H. E., M. G. Kivelson, R. J. Walker, and D. J. McComas, Magnetospheric plasma pressures in the midnight meridian: Observations from 2.5 to 35 R_E, *J. Geophys. Res.*, *94*, 5264, 1989.

Sweet, P. A., The neutral point theories of solar flares, in *Electromagnetic Phenomena in Cosmic Physics, edited by E. Lehnert*, p. 135. 1958.

Takahashi, K., L. J. Zanetti, R. E. Lopez, R. W. McEntire, T. A. Potemra, and K. Yumoto, Disruption of the magnetotail current sheet observed by AMPTE/CCE, *Geophys. Res. Lett.*, *14*, 1019, 1987a.

Takahashi, K., J. F. Fennell, E. Amata, and P. R. Higbie, Field-aligned structure of the storm time Pc 5 waves of November 14–15, 1979, *J. Geophys. Res.*, *92*, 5857–5864, 1987b.

Tanaka, T., The state transition model of the substorm onset, *J. Geophys. Res.*, *105*, 21,081, 2000.

Tsyganenko, N. A., and T. Mukai, Tail plasma sheet models derived from Geotail particle data, *J. Geophys. Res.*, *108*(A3), doi:10.1029/2002JA009707, 2003.

Tsyganenko, N. A., and D. P. Stern, Modeling the global magnetic field of the large-scale Birkeland current systems, *J. Geophys. Res.*, *101*, 27187, 1996.

Vasyliunas, V. M., Mathematical models of magnetospheric convection and its coupling to the ionosphere, in *Particles and Fields in the Magnetosphere, ed. B. M. McCormac, D. Reidel, Hingham, MA*, pp. 60–71. 1970.

Voigt, G.-H., Field line twist and field-aligned currents in an axisymmetric equilibrium magnetosphere, *J. Geophys. Res.*, *91*, 10995, 1986.

Voronkov, I., E. Friedrich, and J. C. Samson, Dynamics of the substorm growth phase as

observed using CANOPUS and SuperDARN instruments, *J. Geophys. Res.*, *104*, 28,491, 1999.

Voronkov, I. O., E. F. Donovan, and J. C. Samson, Observations of the phases of substorms, *J. Geophys. Res.*, *108*, A2, 1073, doi:10.1029/2002JA009314, 2003.

Wang, C. P., L. R. Lyons, M. W. Chen, R. A. Wolf, and F. R. Toffoletto, Modeling the inner plasma sheet protons and magnetic field under enhanced convection, *J. Geophys. Res.*, *108*(A2), 1074, doi: 10.1029/2002JA009620, 2003.

Wiegelmann, T., and K. Schindler, Formation of thin current sheets in a quasistatic magnetotail model, *Geophys. Res. Lett.*, *22*, 2057, 1995.

Wing, S., and P. T. Newell, Central plasma sheet ion properties as inferred from ionospheric observations, *J. Geophys. Res.*, *103*, 6785, 1998.

Wolf, R. A., The quasi-static (slow-flow) region of the magnetosphere, in *Solar-Terrestrial Physics*, pp. 303–368. Kluwer Academic, 1983.

Zaharia, S., and C. Z. Cheng, Near-Earth thin current sheets and Birkeland currents during substorm growth phase, *Geophys. Res. Lett.*, *30(17)*, 1883, doi:10.1029/2003GL017456, 2003.

Zaharia, S., C. Z. Cheng, and K. Maezawa, 3D force balanced magnetospheric configurations, *Ann. Geophys.*, *21*, paper number – AG03014, in press, 2003.

Zaharia, S. G., C. Z. Cheng, and J. R. Johnson, Particle transport and energization associated with substorms, *J. Geophys. Res.*, *105*, 18741, 2000.

This manuscript was prepared with the AGU LaTeX macros v3.0.

With the extension package 'AGU^{++}', version 1.2 from 1995/01/12

Figure Captions

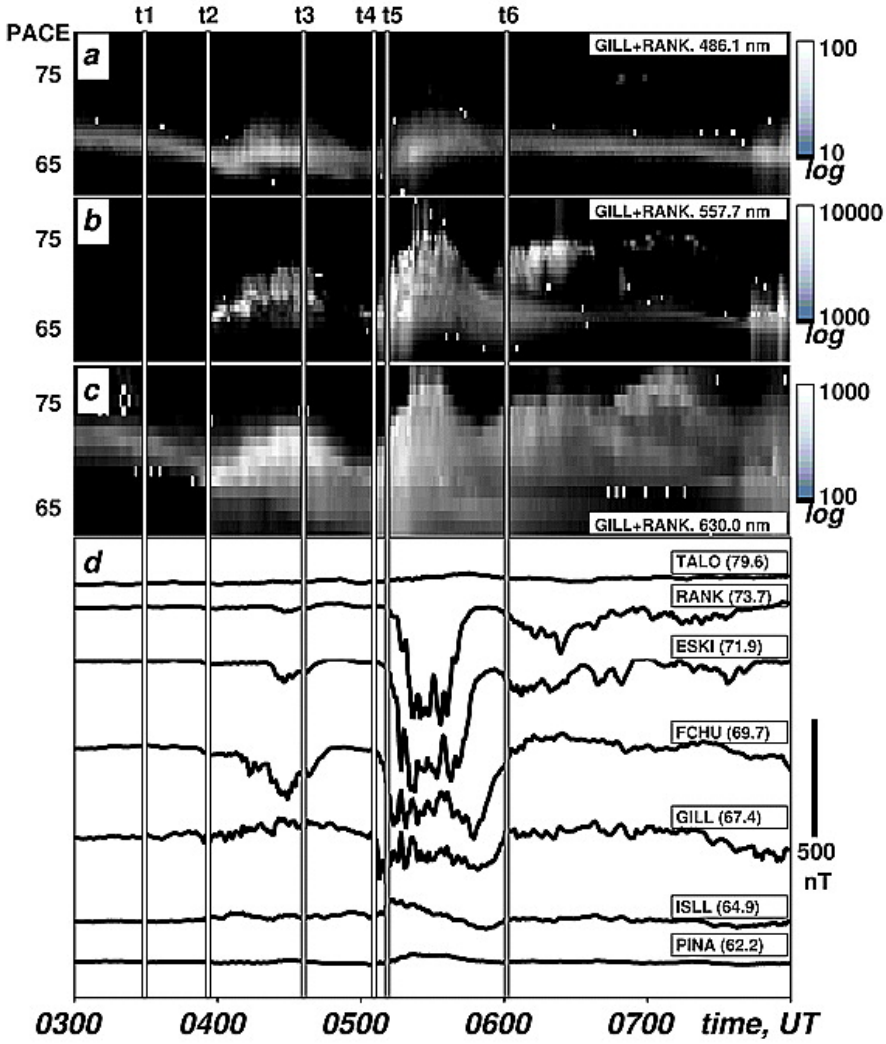

Figure 1. Ground based data for the February 19, 1996 substorm event: Merged GILL and RANK MSP data for emissions of the spectral lines (a) 486.1 nm, (b) 557.7 nm, (c) 630.0 nm, and (d) the X-component of the magnetic field at Churchill line. The PACE latitudes of the Churchill line magnetometers are shown in brackets. The time labels for the vertical lines indicate that t1 is the beginning of the growth phase, t2 is the start of pseudo-breakup, t3 is the recovery of the local substorm and the beginning of the second growth phase, t4 is the breakup onset, t5 is the full substorm onset, and t6 is the poleward boundary intensification at the substorm recovery phase. The figure was published in *Voronkov et al.* [2003] as Figure 3.

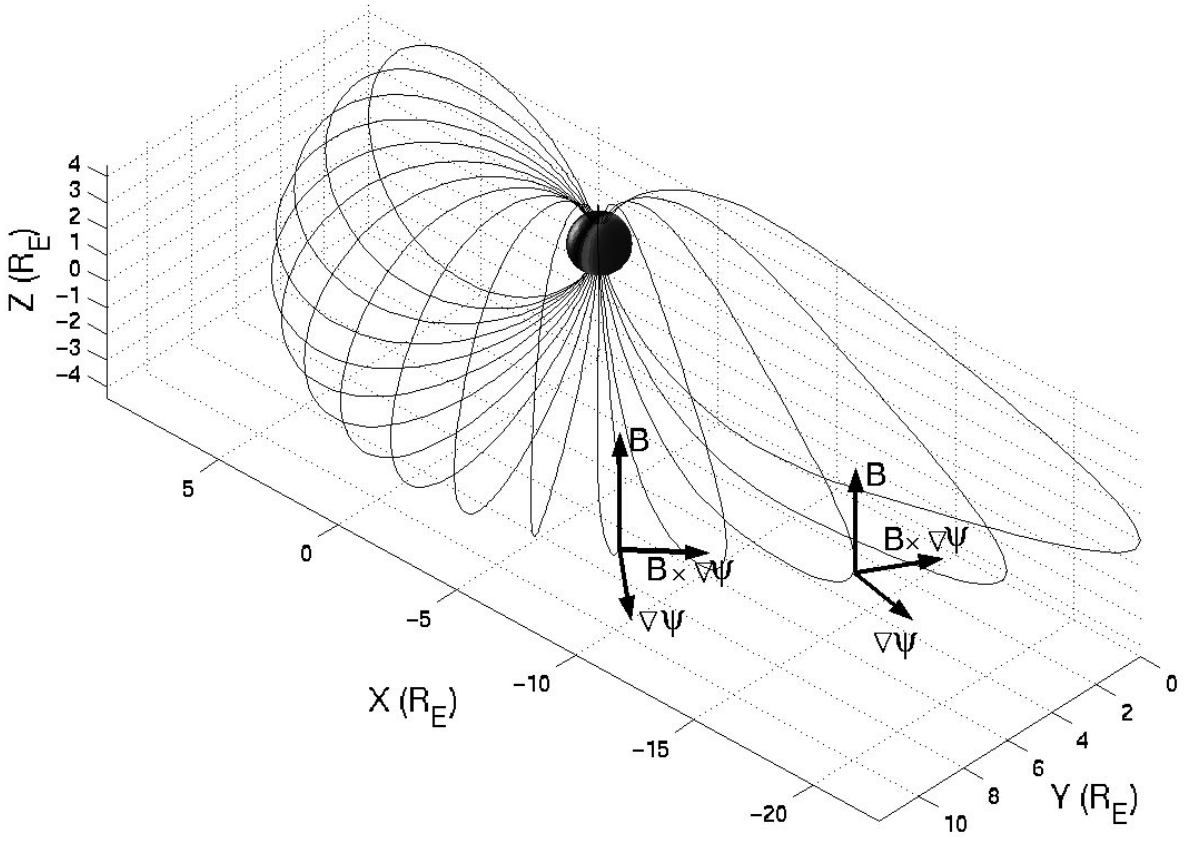

Figure 2. Field lines in a constant ψ surface of a three-dimensional magnetospheric equilibrium. The three orthogonal vectors used for the decomposition of the displacement vector and perturbed magnetic field are shown. The figure was published in *Cheng* [2003] as Figure 1.

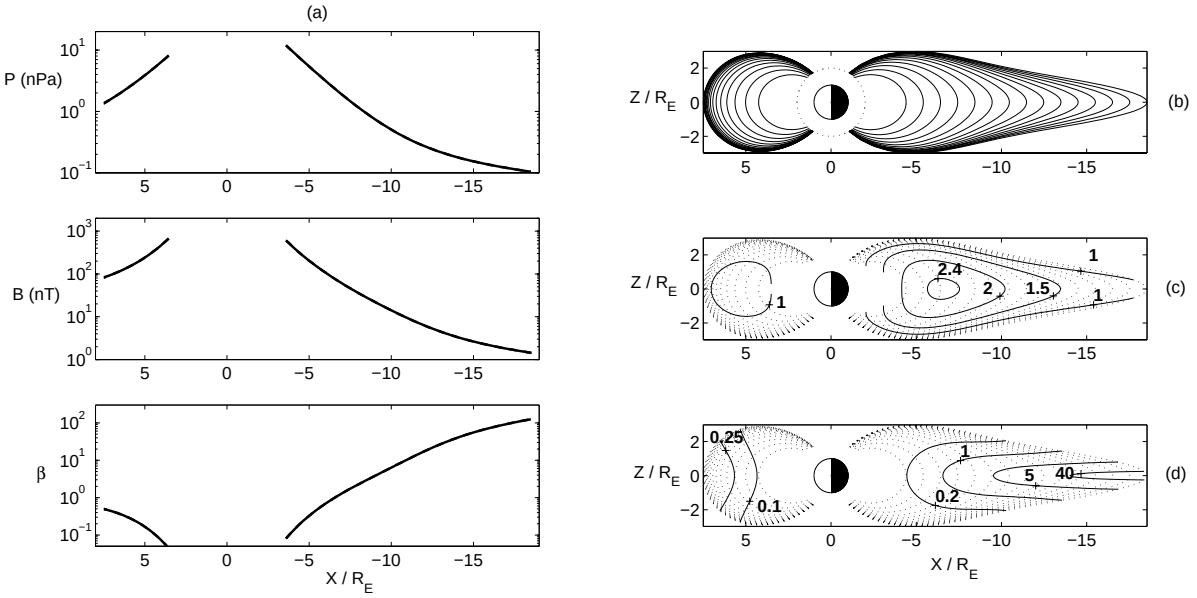

Figure 3. (a) Profiles of P, B and β along the Sun-Earth axis for the quiet-time case; and (b) Magnetic field lines; (c) Constant J_ϕ (solid) in the unit of nA/m^2 and ψ (dotted) contours; and (d) Constant β (solid) and ψ (dotted) contours in the noon-midnight meridian plane.

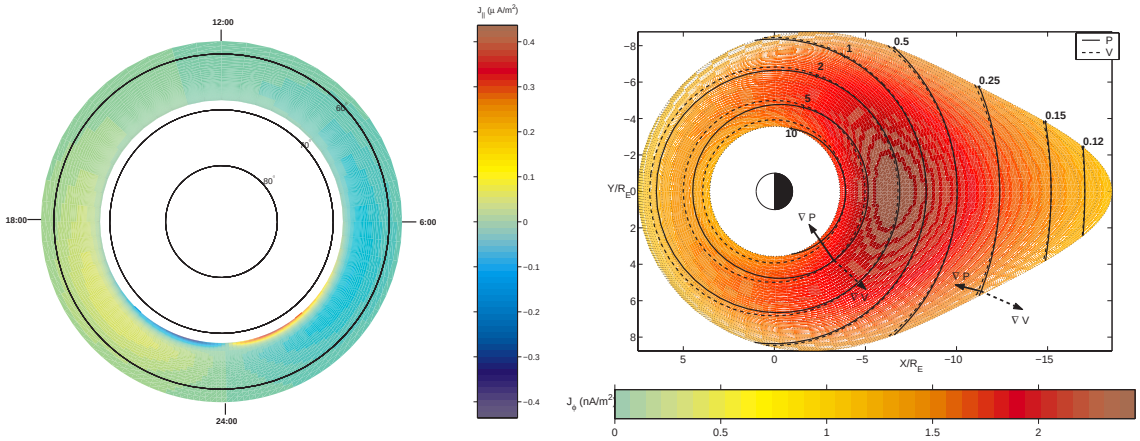

Figure 4. For the quiet-time state: (a) Ionospheric $J_\parallel$ (in μA/m^2); (b) Equatorial plane contours of P(nPa) (thick solid lines), V (dashed) and ψ (dotted), over a color plot of J_ϕ (in nA/m^2); also shown are $\boldsymbol{\nabla} P$ and $\boldsymbol{\nabla} V$ at two points mapping into regions of opposite $J_\parallel$ in the ionosphere.

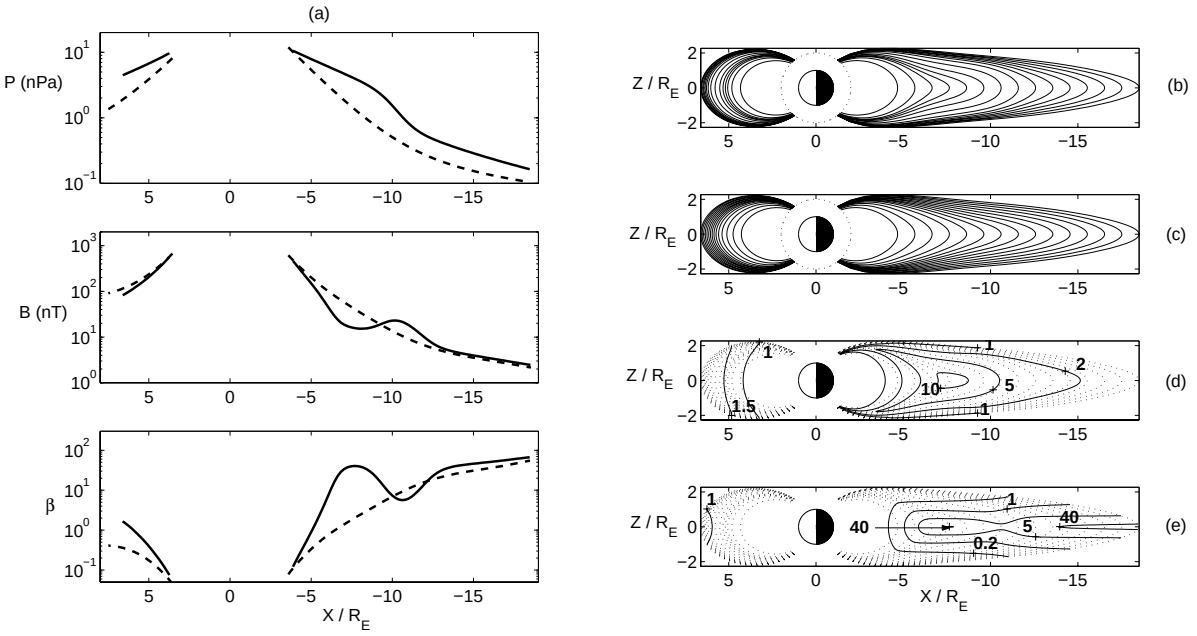

Figure 5. (a) Profiles of P, B and β along the Sun-Earth axis for the growth phase (solid) and quiet-time (dashed); For the growth phase, plots in the noon-midnight meridian plane of : (b) Equilibrium magnetic field lines; (c) Magnetic field lines of T-96 model (for comparison purpose); (d) Constant J_ϕ (solid) and ψ (dotted) contours; (e) Constant β (solid) and ψ (dotted) contours. A part of the figures was published in *Zaharia and Cheng* [2003] as Fig. 2.

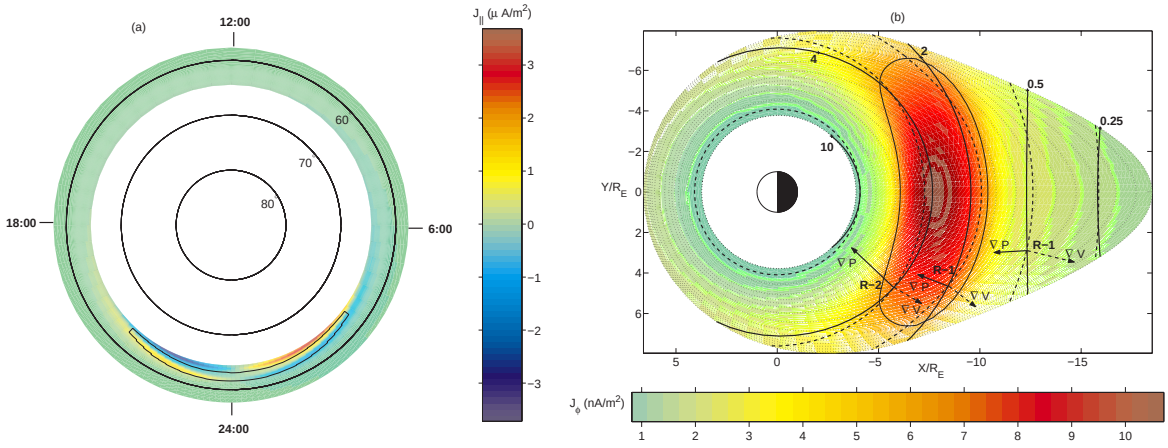

Figure 6. For the growth phase: (a) Ionospheric $J_\parallel$; (b) Equatorial plane P(nPa) contours (thick solid lines), V (dashed) and ψ (dotted), over a color plot of J_ϕ; the thin solid contour shows the region inside which $J_\phi > 0.5\, J_{\phi\max}$; also shown are $\boldsymbol{\nabla} P$ and $\boldsymbol{\nabla} V$ at three locations. The figure was published in *Zaharia and Cheng* [2003] as Fig. 3.

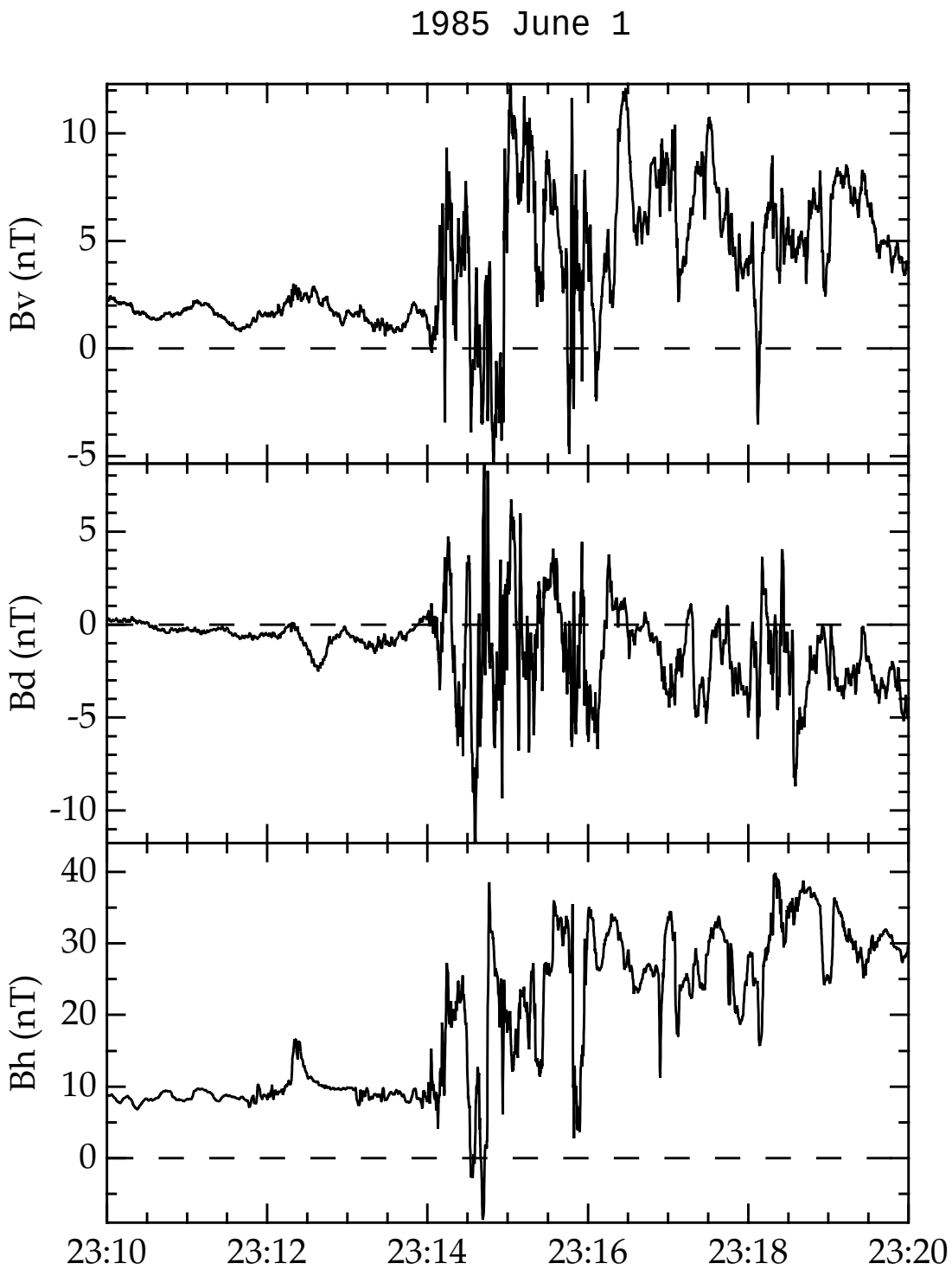

Figure 7. Three components of magnetic field measured by AMPTE/CCE at high time resolution for the June 1, 1985 substorm event. The figure was published in *Lui et al.* [1992] as Figure 4.

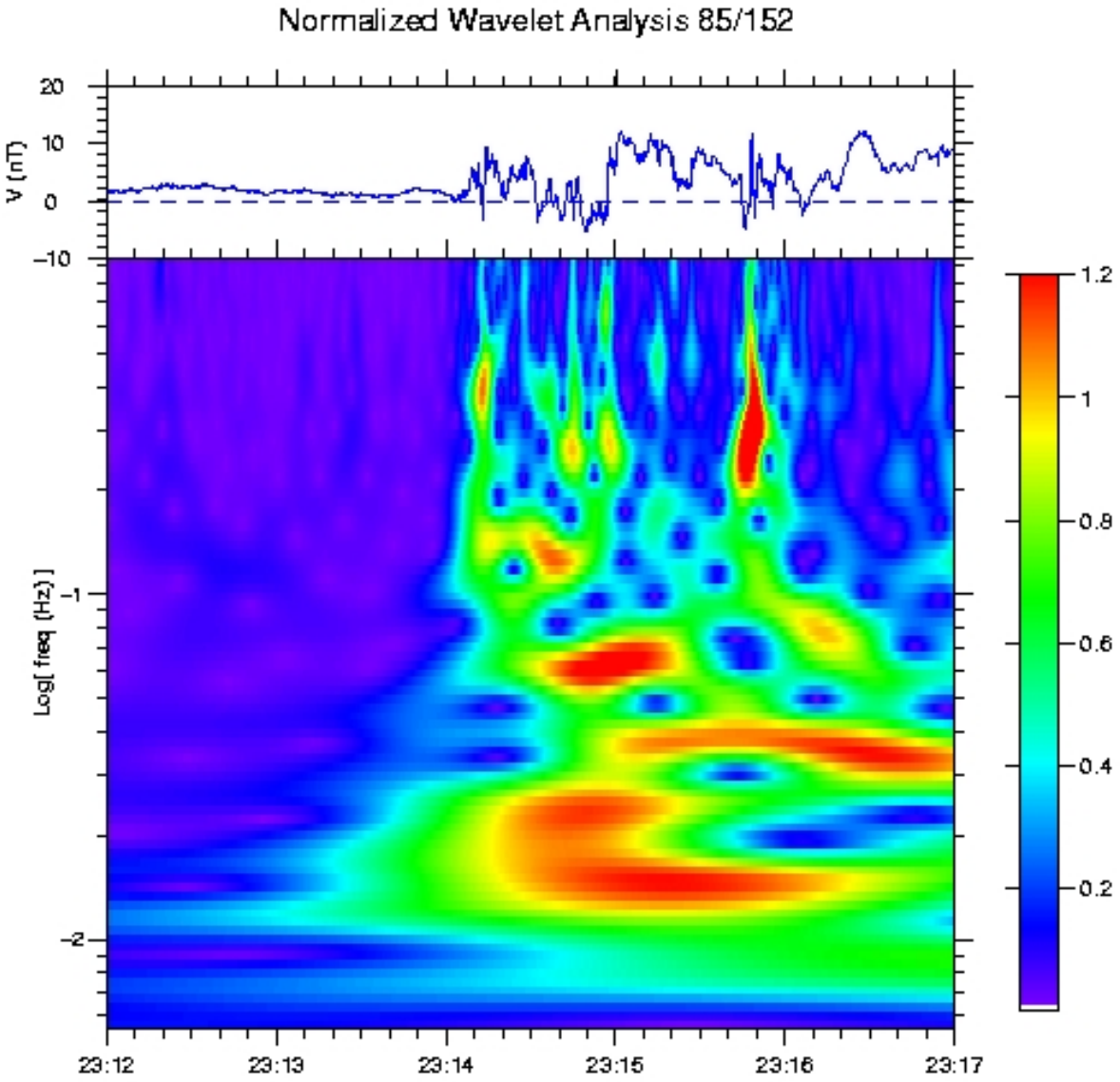

Figure 8. The power spectrogram of the V component of the perturbed magnetic field using wavelet analysis for the June 1, 1985 substorm event. The figure was published in *Lui and Najmi* [1997] as Plate 2.

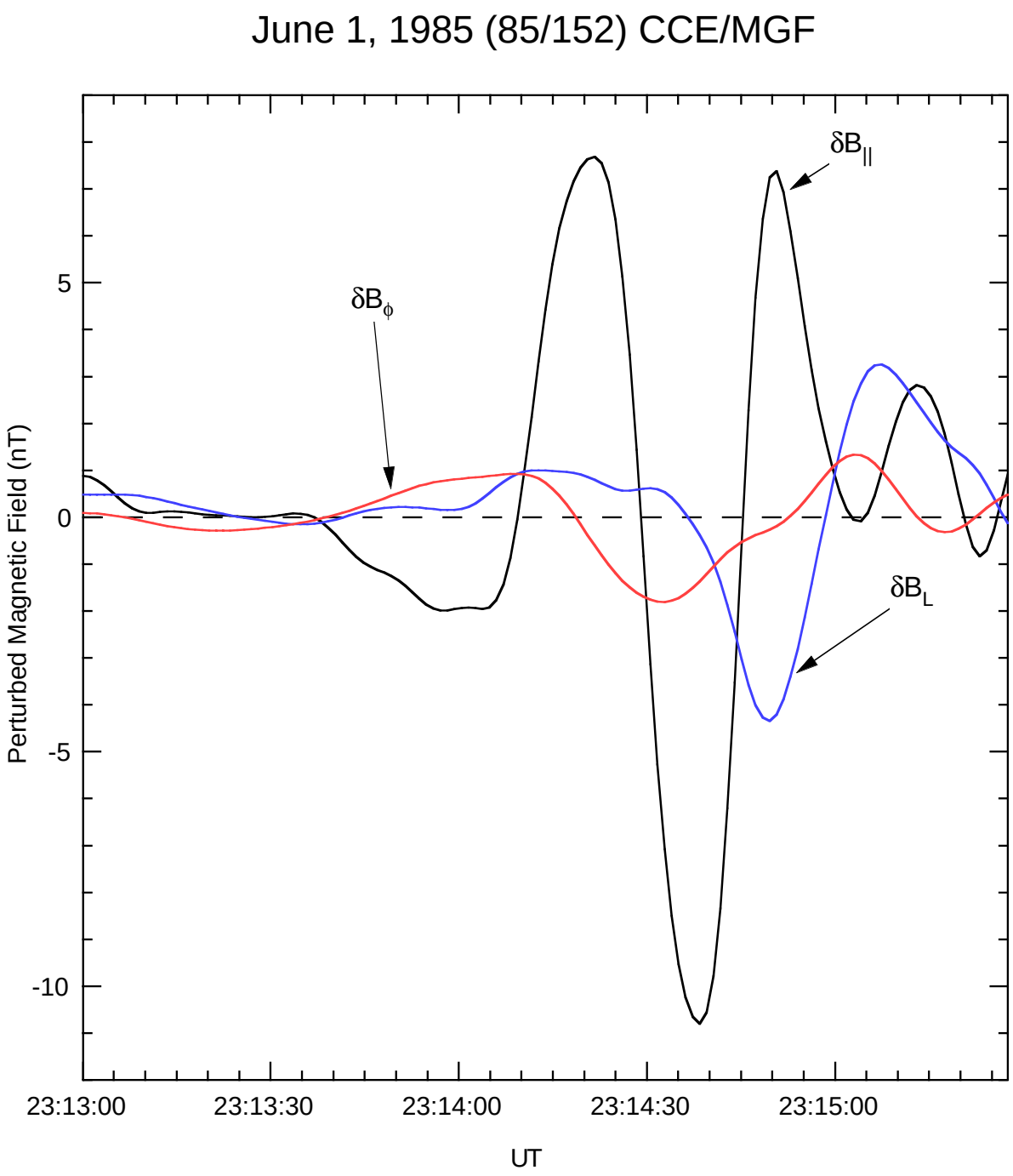

Figure 9. Three components of the low frequency component of the perturbed magnetic field for the June 1, 1985 substorm event.

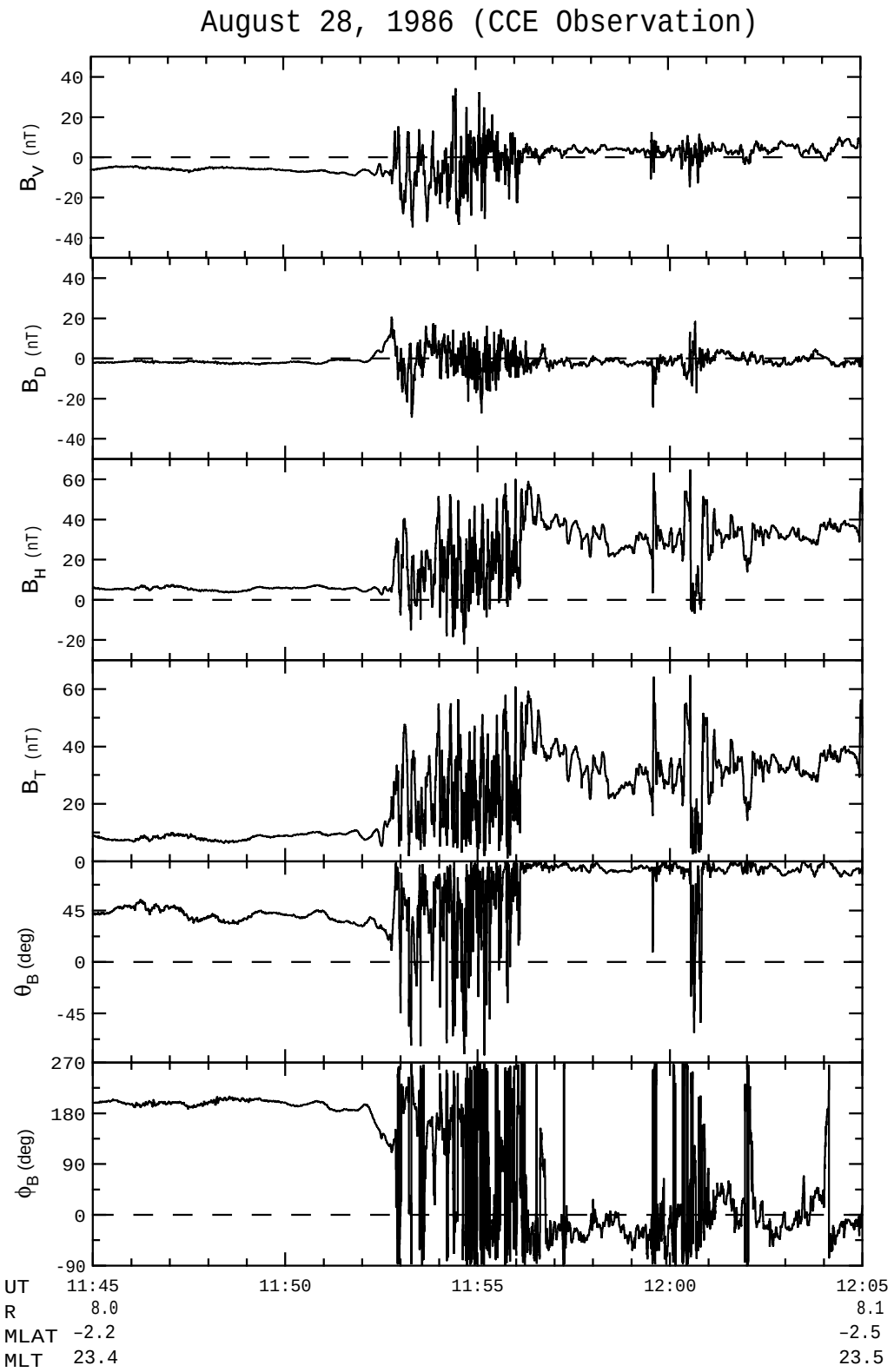

Figure 10. Three components of magnetic field measured by AMPTE/CCE at high time resolution for the August 28, 1986 substorm event.

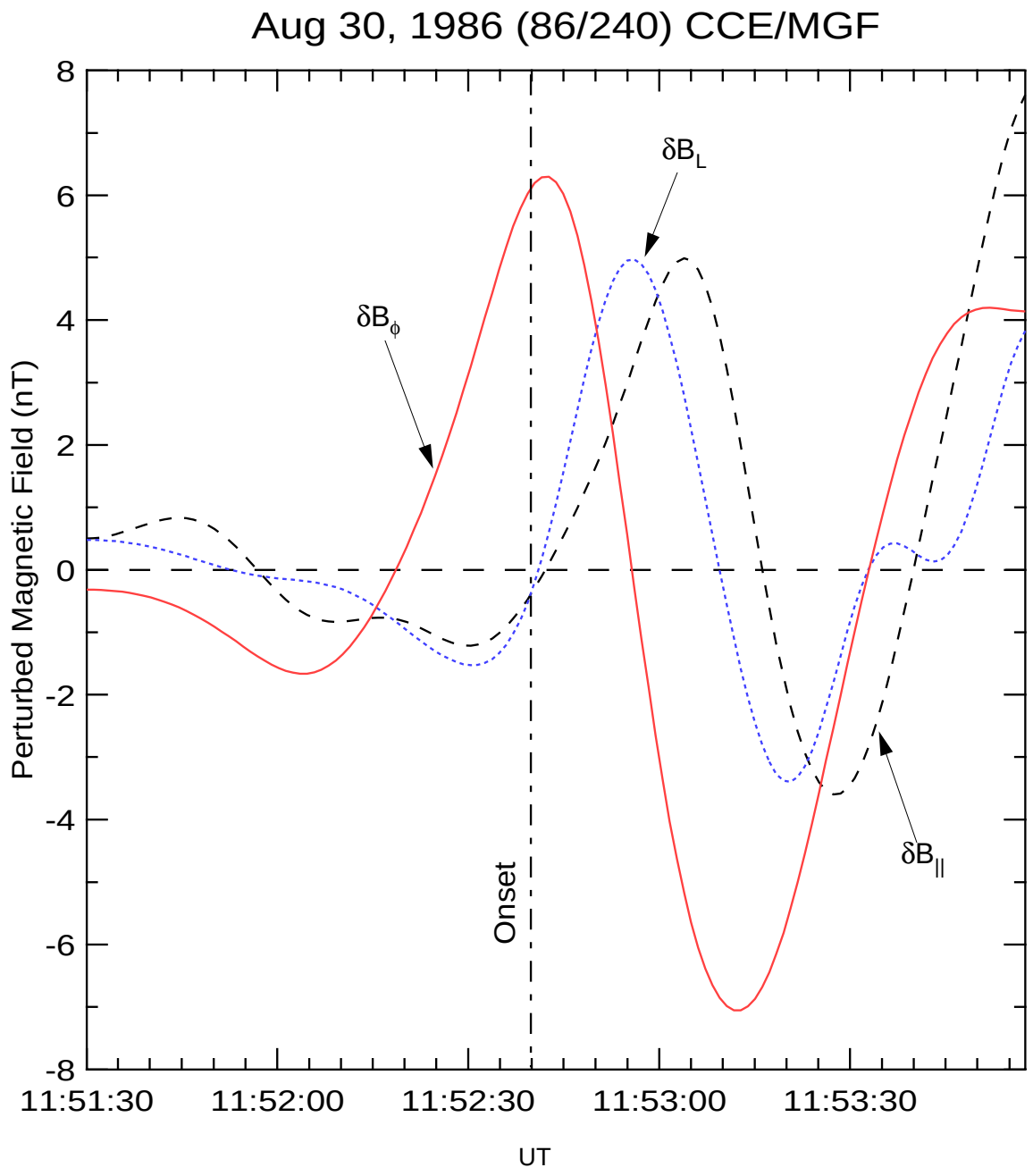

Figure 11. Three components of the low frequency perturbed magnetic field for the August 28, 1986 substorm event. The figure was published in *Cheng and Lui* [1998a] as Figure 1.

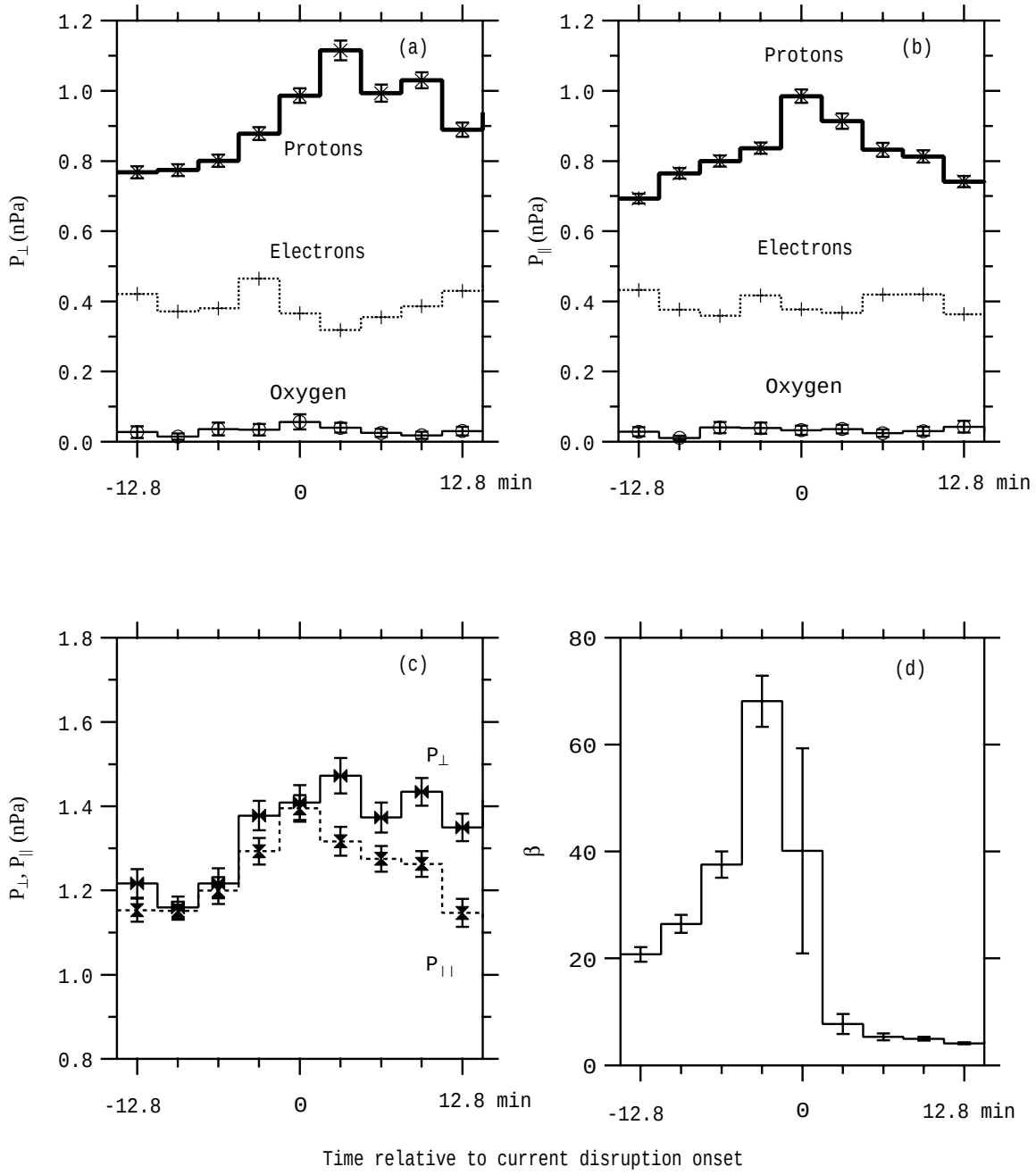

Figure 12. The three-minute averages of the perpendicular and parallel components of the electron and proton and total plasma pressures, and $\beta = (P_\perp + P_\parallel)/B^2$ measured by the AMPTE/CCE satellite for the June 1, 1985 substorm event. The figure was published in *Lui et al.* [1992] as Figure 4.

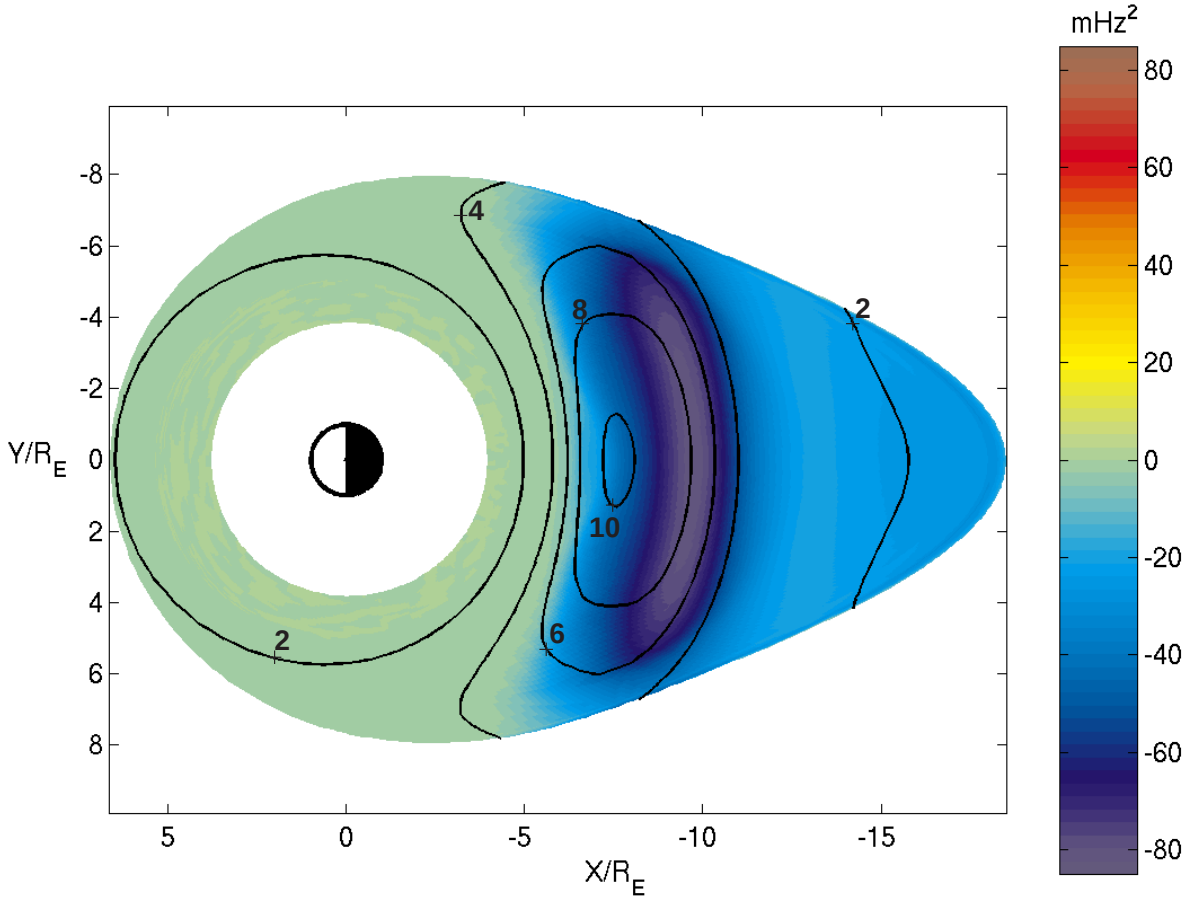

Figure 13. The square of frequency (in $(mHz)^2$) of ballooning modes is shown in color in the equatorial plane for the growth phase equilibrium with the full MHD model. The contours of the azimuthal current density (in nA/m^2) are also plotted to show the location of the most unstable region relative to the strong cross-tail current region. The figure is from Figure 1 of *Cheng and Zaharia* [2003b].

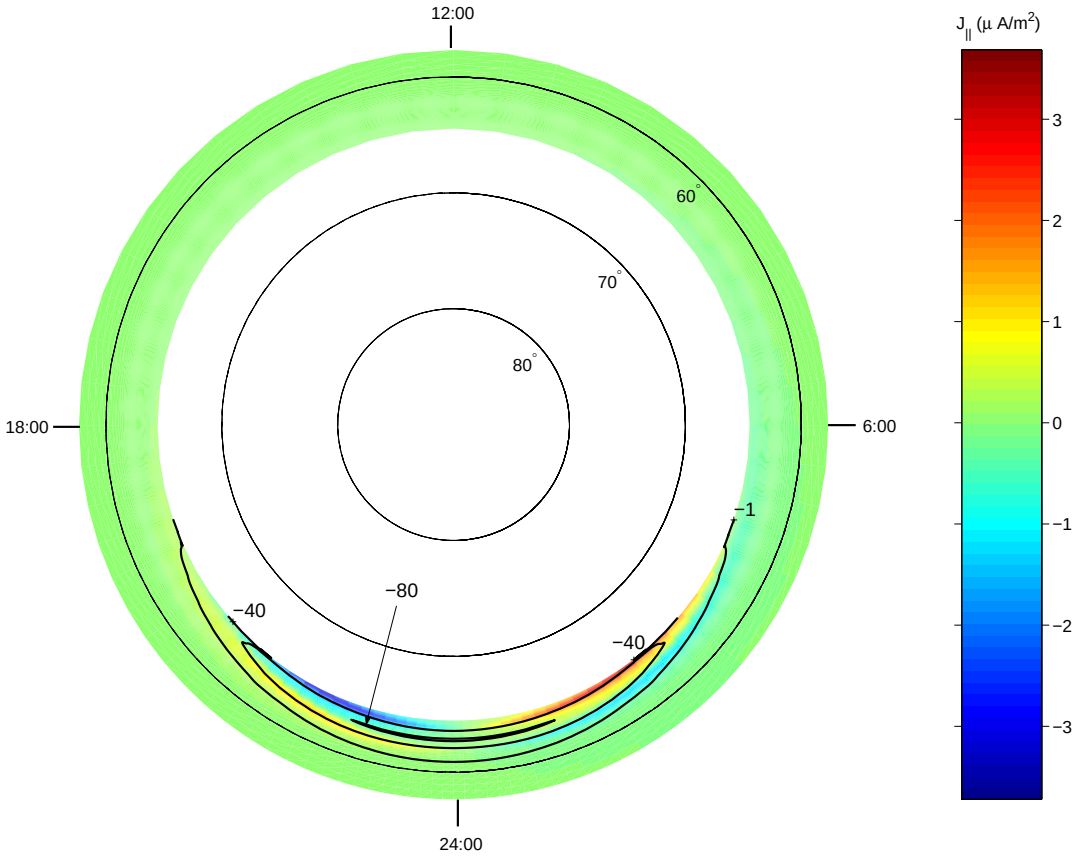

Figure 14. The contours of the square of frequency (in $(mHz)^2$) of ballooning modes are plotted over the northern polar ionosphere for the growth phase equilibrium with the full MHD model. The field-aligned current density is also shown in color to show that the most unstable ballooning instability region is located at the transition region between the region-1 and region-2 currents. The figure is from Figure 2 of *Cheng and Zaharia* [2003b].

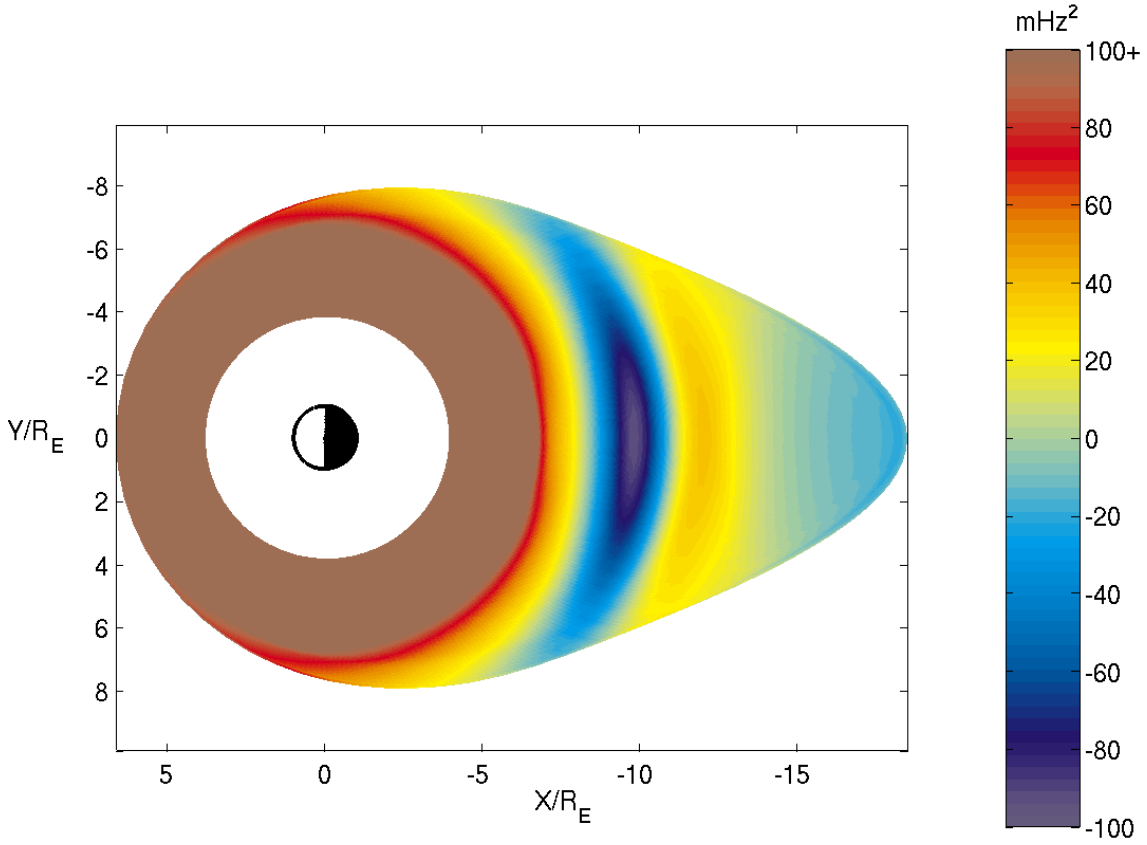

Figure 15. The square of frequency (in $(mHz)^2$) of ballooning modes is plotted in the equatorial plane for the growth phase equilibrium with the Lee-Wolf model of compressibility. The figure is from Figure 3 of *Cheng and Zaharia* [2003b].

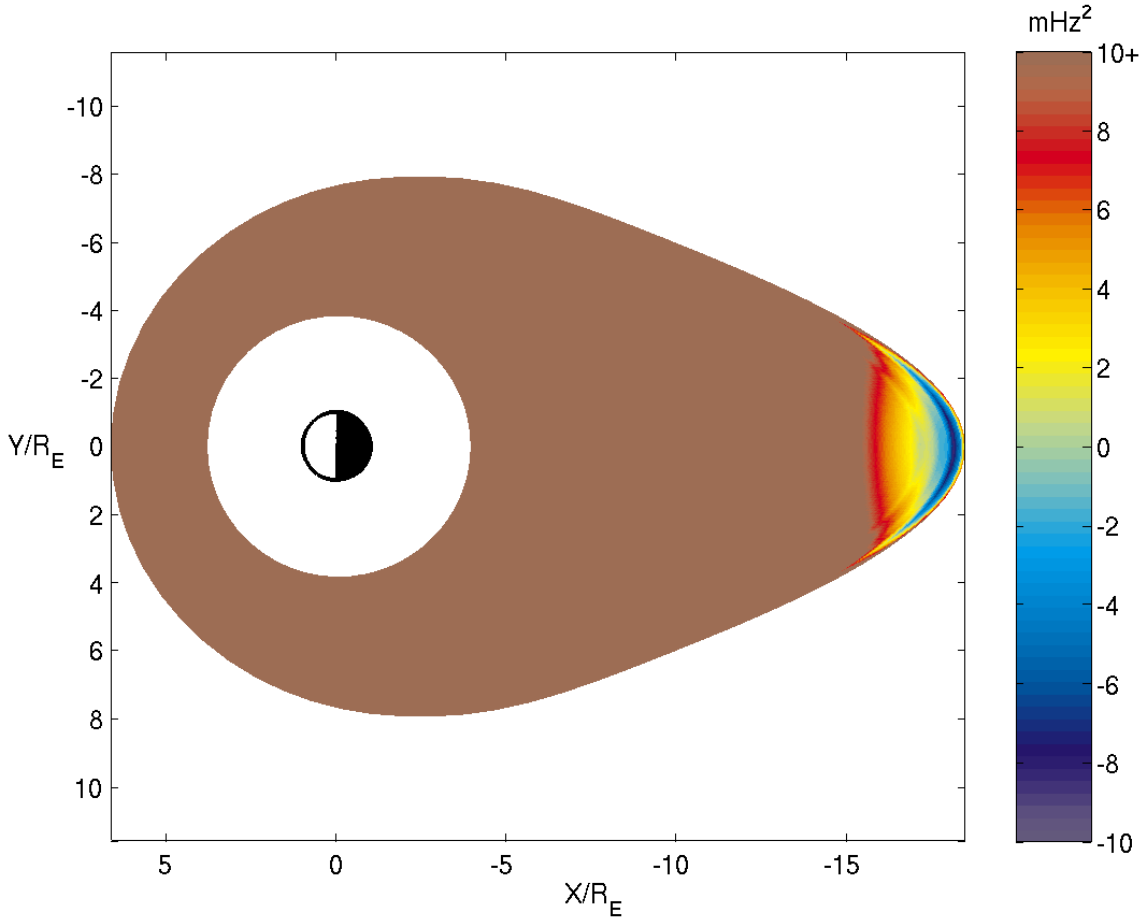

Figure 16. The square of frequency (in $(mHz)^2$) of ballooning modes is plotted over the equatorial plane for the growth phase equilibrium with the fast-MHD model of compressibility. The figure is from Figure 4 of *Cheng and Zaharia* [2003b].

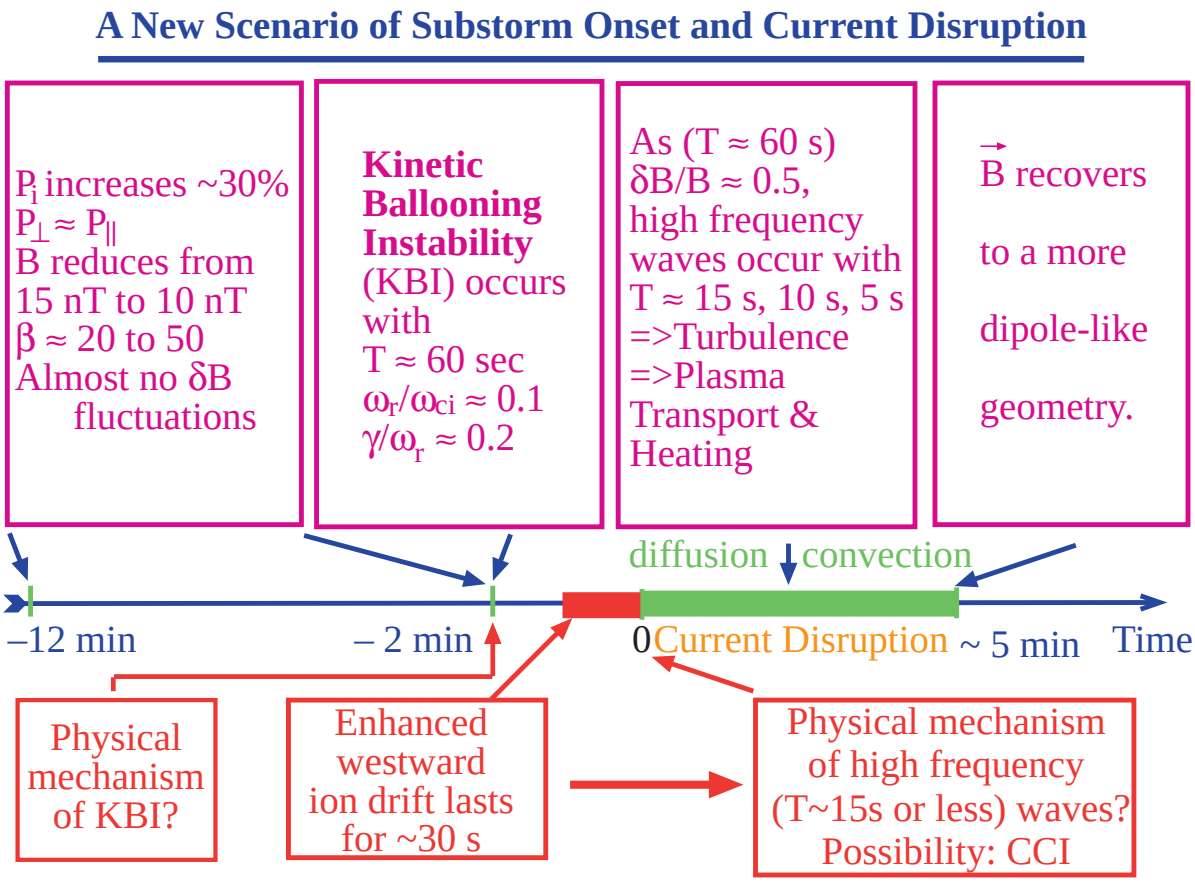

Figure 17. A substorm scenario.

External Distribution

Plasma Research Laboratory, Australian National University, Australia

Professor I.R. Jones, Flinders University, Australia

Professor João Canalle, Instituto de Fisica DEQ/IF - UERJ, Brazil

Mr. Gerson O. Ludwig, Instituto Nacional de Pesquisas, Brazil

Dr. P.H. Sakanaka, Instituto Fisica, Brazil

The Librarian, Culham Laboratory, England

Mrs. S.A. Hutchinson, JET Library, England

Professor M.N. Bussac, Ecole Polytechnique, France

Librarian, Max-Planck-Institut für Plasmaphysik, Germany

Jolan Moldvai, Reports Library, Hungarian Academy of Sciences, Central Research Institute for Physics, Hungary

Dr. P. Kaw, Institute for Plasma Research, India

Ms. P.J. Pathak, Librarian, Institute for Plasma Research, India

Ms. Clelia De Palo, Associazione EURATOM-ENEA, Italy

Dr. G. Grosso, Instituto di Fisica del Plasma, Italy

Librarian, Naka Fusion Research Establishment, JAERI, Japan

Library, Laboratory for Complex Energy Processes, Institute for Advanced Study, Kyoto University, Japan

Research Information Center, National Institute for Fusion Science, Japan

Dr. O. Mitarai, Kyushu Tokai University, Japan

Dr. Jiangang Li, Institute of Plasma Physics, Chinese Academy of Sciences, People's Republic of China

Professor Yuping Huo, School of Physical Science and Technology, People's Republic of China

Library, Academia Sinica, Institute of Plasma Physics, People's Republic of China

Librarian, Institute of Physics, Chinese Academy of Sciences, People's Republic of China

Dr. S. Mirnov, TRINITI, Troitsk, Russian Federation, Russia

Dr. V.S. Strelkov, Kurchatov Institute, Russian Federation, Russia

Professor Peter Lukac, Katedra Fyziky Plazmy MFF UK, Mlynska dolina F-2, Komenskeho Univerzita, SK-842 15 Bratislava, Slovakia

Dr. G.S. Lee, Korea Basic Science Institute, South Korea

Institute for Plasma Research, University of Maryland, USA

Librarian, Fusion Energy Division, Oak Ridge National Laboratory, USA

Librarian, Institute of Fusion Studies, University of Texas, USA

Librarian, Magnetic Fusion Program, Lawrence Livermore National Laboratory, USA

Library, General Atomics, USA

Plasma Physics Group, Fusion Energy Research Program, University of California at San Diego, USA

Plasma Physics Library, Columbia University, USA

Alkesh Punjabi, Center for Fusion Research and Training, Hampton University, USA

Dr. W.M. Stacey, Fusion Research Center, Georgia Institute of Technology, USA

Dr. John Willis, U.S. Department of Energy, Office of Fusion Energy Sciences, USA

Mr. Paul H. Wright, Indianapolis, Indiana, USA

The Princeton Plasma Physics Laboratory is operated
by Princeton University under contract
with the U.S. Department of Energy.

Information Services
Princeton Plasma Physics Laboratory
P.O. Box 451
Princeton, NJ 08543

Phone: 609-243-2750
Fax: 609-243-2751
e-mail: pppl_info@pppl.gov
Internet Address: http://www.pppl.gov